VILNIUS UNIVERSITY
CENTER FOR PHYSICAL SCIENCES AND TECHNOLOGY

Žydrūnas
PODLIPSKAS

Carrier Dynamics in III-Nitrides: From AlGaN to InN

DOCTORAL DISSERTATION

Natural sciences,
Physics N 002

VILNIUS 2019

This dissertation was written between 2014 and 2019 at the Institute of Photonics and Nanotechnology, Vilnius University. The research was supported by the Research Council of Lithuania (scholarship for academic accomplishments DOK-17436).

Academic supervisor:

Assoc. Prof. Dr. Ramūnas Aleksiejūnas (Institute of Photonics and Nanotechnology, Vilnius University, Natural sciences, Physics N 002)

Dissertation Defense Panel:

Chairman – **Prof. Habil. Dr. Gintaras Valušis** (Center for Physical Sciences and Technology, Natural sciences, Physics N 002)

Members:

Dr. Ramūnas Adomavičius (Center for Physical Sciences and Technology, Natural sciences, Physics N 002)

Dr. Audrius Alkauskas (Center for Physical Sciences and Technology, Natural sciences, Physics N 002)

Dr. Tomas Čeponis (Institute of Photonics and Nanotechnology, Vilnius University, Technological sciences, Materials engineering T 008)

Prof. Habil. Dr. Saulius A. Juršėnas (Institute of Photonics and Nanotechnology, Vilnius University, Natural sciences, Physics N 002)

The dissertation shall be defended at a public meeting of the Dissertation Defense Panel at 2:00 PM on November 29, 2019 in Room A101 of the National Center for Physical Sciences and Technology. Address: Saulėtekio ave. 3, Vilnius, Lithuania

Tel. +37052648884; e-mail office@ftmc.lt

The text of this dissertation can be accessed at the libraries of Center for Physical Sciences and Technology and Vilnius University, as well as on the website of Vilnius University:

www.vu.lt/lt/naujienos/ivykiu-kalendorius

VILNIAUS UNIVERSITETAS
FIZINIŲ IR TECHNOLOGIJOS MOKSLŲ CENTRAS

Žydrūnas
PODLIPSKAS

Krūvininkų dinamika III grupės nitridiniuose junginiuose: nuo AlGaN iki InN

DAKTARO DISERTACIJA

Gamtos mokslai,
Fizika N 002

VILNIUS 2019

Disertacija rengta 2014 – 2019 metais Vilniaus universiteto Fotonikos ir nanotechnologijų institute. Mokslinius tyrimus rėmė Lietuvos mokslo taryba (stipendija už akademinius pasiekimus DOK-17436).

Mokslinis vadovas:

Doc. dr. Ramūnas Aleksiejūnas (Fotonikos ir nanotechnologijų institutas, Vilniaus universitetas, gamtos mokslai, fizika N 002)

Gynimo taryba:

Pirmininkas – **Prof. habil. dr. Gintaras Valušis** (Fizinių ir technologijos mokslų centras, gamtos mokslai, fizika N 002)

Nariai:

Dr. Ramūnas Adomavičius (Fizinių ir technologijos mokslų centras, gamtos mokslai, fizika N 002)

Dr. Audrius Alkauskas (Fizinių ir technologijos mokslų centras, gamtos mokslai, fizika N 002)

Dr. Tomas Čeponis (Fotonikos ir nanotechnologijų institutas, Vilniaus universitetas, technologijos mokslai, medžiagų inžinerija T 008)

Prof. habil. dr. Saulius A. Juršėnas (Fotonikos ir nanotechnologijų institutas, Vilniaus universitetas, gamtos mokslai, fizika N 002)

Disertacija ginama viešame Gynimo tarybos posėdyje 2019 m. lapkričio mėn. 29 d. 14:00 val. Nacionalinio fizinių ir technologijos mokslų centro A101 auditorijoje. Adresas: Saulėtekio al. 3, Vilnius, Lietuva

Tel. +37052648884; el. paštas office@ftmc.lt

Disertaciją galima peržiūrėti Fizinių ir technologijos mokslų centro bei Vilniaus universiteto bibliotekose ir Vilniaus universiteto interneto svetainėje adresu:

www.vu.lt/lt/naujienos/ivykiu-kalendorius

Padėka

Neklasifikuodamas adresatų pagal svarbą pirmu artėjimu dėkoju visiems chroniškiems bei jau reabilituotiems *713 palatos*[a] pacientams ir daktarams, tarp jų:

Dr. Ramūnui Aleksiejūnui (vadovui) – už beatodairišką pasitikėjimą ir neribotą laisvę — kartais šio gėrio man buvo per daug, nors to mažinimui ir būčiau priešinęsis;

Dr. Sauliui Nargelui – už pagalbą bet kokiais techniniais klausimais, susijusiais ne tik su palatos veikla;

Daktarams Tadui Malinauskui ir Arūnui Kadžiui – už palatoje paklotus programinės įrangos pamatus ir palopytas mano žinių skyles;

Pacientui (dr. nuo 19-10-24) Kazimierui Nomeikai – už disertacijos gynimo nuotykio ‚walkthrough'.

Antru artėjimu dėkoju:

Prof. Gintautui Tamulaičiui (antram vadovui) – už mano nesibaigiančių perfekcionistinių paieškų toleravimą;

Regimantui Komskiui – už pokalbius gryname ore;

Dr. Akvilei Zabiliūtei-Karaliūnei ir Žygimantui Vosyliui – už gelbėjimą paskutinio spurto metu prabudusioje akademinėje veikloje;

Dr. Jonui Jurkevičiui – už maistą, kritiką ir visapusiškai smagesnę dieną;

Justei Kudzytei ir FNI administracijai – už vietoje manęs atliktus skambučius ir išsiųstus laiškus;

Žurnalų recenzentams Nr. 2 – už vaizduotės lavinimą generuojant pravardes bei savo veiklos kvestionavimą.

Svarbiausiu artėjimu dėkoju:

Draugei Editai Mažutavičiūtei – už tai, kad leidai būti keistu, ir didžiausio tingulio akimirkomis geranoriškai priminei, jog jau pernai turėjau apsiginti (heart emoji);

Tėvams Audronei ir Olegui – už tai, kad esate, ir už tai, kad nuolat skatinote būti kūrybingu.

[a] Laboratorija, kurioje augau.

Table of Contents

Acronyms

EQE	external quantum efficiency
HEMT	high electron mobility transistor
2DEG	two-dimensional electron gas
LD	laser diode
NW	nanowire
WoS	Web of Science
EL	electroluminescence
SE	stimulated emission
MBE	molecular beam epitaxy
hBN	hexagonal boron nitride
TMDC	transition metal dichalcogenide
HOIP	hybrid organic-inorganic perovskite
HT	high-throughput
DFT	density functional theory
MOCVD	metalorganic chemical vapor deposition
TMAl	tri-methyl-aluminum
TMGa	tri-methyl-gallium
MEMOCVD	migration-enhanced MOCVD
SETi	Sensor Electronic Technology, inc.
PL	photoluminescence
TRPL	time-resolved photoluminescence spectroscopy
LITG	light-induced transient grating
SRH	Shockley-Read-Hall
HBS	holographic beam splitter
PD	photodetector/diode
IQE	internal quantum efficiency
REDR	recombination-enhanced defect reactions
SR	surface recombination

SQW	single quantum well
u-InN	unintentionally doped indium nitride
PV	photovoltaic
SPE	Solar particle/proton event
NIEL	nonionizing energy loss
NRL	Naval Research Laboratory
QW	quantum well

Introduction

Currently, there are more than 3'000 unique nitride compounds catalogued in the Inorganic Crystal Structure Database,[1,2] and three of them – InN, GaN, AlN, and their ternary or quaternary counterparts – are extensively investigated. The main reason why these particular nitrides became such a compelling material system is their tunable bandgaps, featuring photon energies in IR range (down to 0.65 eV in InN), the entire visible spectrum (in InGaN), and UV range (up to 6 eV in AlN). This quality allows to exploit them in plethora of unique applications, for instance: AlGaN system has been an irreplaceable building block for UV LEDs and photodiodes; GaN slowly but surely is becoming an integral part in power electronics, surpassing Si in efficiency, voltage limits, operating frequency, and all sorts of hardnesses (temperature, radiation, etc.); while InGaN has been dominating semiconductor lighting markets with virtually nondeteriorating LEDs for visible spectrum.

Despite these outstanding properties and wide-reaching applications cultivated for decades and used by millions, nitride name has been barely known outside academia and industry, contrary to the silicon. This year, however, gallium nitride was finally noticed by tech media giants, such as *The Verge*, and [as usual for every recognized semiconductor] was touted as the silicon of the future.[3] Meanwhile, companies like *Anker* started using *GaN* as a marketing buzzword for extremely small and relatively powerful powerbanks and chargers tailored for everyday portable devices[4] – a technology trickled down from electric cars. This change not only indicates the emerging awareness of nitrides, but also signifies the material maturity and an ongoing/oncoming shift in nitride studies.

Recently, the maturity of traditional III-nitrides was assessed by Tsao et al.[5] following these parameters: (i) doping development; (ii) substrate size/availability; and (iii) volume/cost, i.e., whether a given nitride system has only specialized/government markets (low-volume/high-cost) or a broad commercial market (high-volume/low-cost), recognizing the leverage brought to a given system by a larger market (such as LED lighting for InGaN). According to this classification, GaN, AlGaN of certain compositions (gravitating towards Al-poor range), and InGaN targeting blue-to-green LEDs are mature material systems, while Al-rich AlGaN, AlN, In-rich InGaN, and InN are immature.

In case of mature systems, the research on basic material properties is reasonably complete (although not all lingering problems are solved), and

optimization of growth or design of conventional devices is basically taken over by industry, more often than not surpassing the academia. Meanwhile, academic research is defocusing from routine material characterization and is shifting towards novel unconventional applications, often multidisciplinary in nature. Such ventures include development of GaN microprocessors[6] and neutron detectors[7] tailored for space-bound harsh environments; investigation of nitride surfaces and interfaces connecting synthetic materials and biological entities for bioelectronics;[8,9] development of GaN-based photochemical diodes for water splitting;[10] realization of RT single-photon emission from defects in nitrides for quantum computing;[11] or discovery of surprising properties, such as diamond-like wear resistance.[12] In addition to this shift, mature nitrides are also becoming the role models for immature/novel nitride systems trying to catch up with their senior siblings.

In case of immature nitrides, the research on basic material properties is still in its infancy. For instance, frequent studies on carrier dynamics in mature InGaN alloys are a rare sight in immature InN or Al-rich AlGaN, leading to highly scattered data or lack of any results altogether. This discrepancy is caused by numerous intertwined factors: challenging growth, low-quality samples, more complicated experiments in IR and UV-C ranges, absence of noteworthy devices or breakthrough discoveries (for InN), and in some cases – just a lack of interest. Nevertheless, immature nitrides may still hold some game-changing properties hiding in blank spots of their research, making them worth to investigate.

Aim and novelty

This thesis is a compilation of studies on carrier dynamics in various traditional III-nitrides (specifically, AlGaN, GaN, and InN), different both in composition and maturity level. To target materials in different development stages, the work focusses on a two-fold goal:

> In case of immature nitrides, the thesis aims to fill in the missing data on basic properties of carrier recombination and diffusion; in case of mature nitrides, the work targets advanced unexplored phenomena, such as recombination-enhanced defect reactions or interface recombination, and their impact on material performance.

On the whole, the work features five distinct objectives/studies significant in their own respective manner.

The first study (Chapter A; based on Paper A) addresses carrier recombination both in Al-poor and Al-rich AlGaN epilayers and describes evolution of radiative as well as nonradiative recombination channels with changing excess carrier density. Most importantly, the study evaluates AlGaN radiative performance and provides previously unreported recombination coefficients assessed in combination of two techniques: a time resolved one – light-induced transient gratings (LITG), and a time integrated one – quasi-stationary photoluminescence (PL) spectroscopy. Although such study would not be unprecedented in InGaN research space, it is rather unique for AlGaN alloys, lacking comprehensive picture on carrier dynamics in the majority of composition range.

The second study (Chapter B; based on Paper B) offers a rare take on the phenomenon of *recombination-enhanced defect reactions* (REDR) in AlGaN alloys. To put it simply, REDR effect is a form of athermal defect annealing activated by nonradiative recombination of excess carriers at extreme densities. Here, such densities are achieved by intense laser illumination – *photomodification*. Through history, REDR phenomenon has been studied in late stages of material development, observed in virtually every significant semiconductor, and blamed for degradation of numerous devices. In nitrides, however, REDR has been encountered/recognized only a handful of times and has been linked to a density-activated increase in concentration of carrier killer centers. Here, the study seeks to single out the material parameters controlling concentration of such centers and susceptibility to photomodification. Moreover, the study investigates impact of photomodification on carrier diffusivity and reveals a surprising outcome – photomodification-induced increase in carrier diffusion coefficient and diffusion length.

The third study (Chapter C, unpublished) assesses the properties of carrier dynamics in ordinary AlGaN/GaN heterointerfaces. In such heterostructures, a substrate or an underneath layer should limit the quality of a subsequent upper layers and the performance of an entire device. Meanwhile, an upper layer should passivate the bottom surface and diminish the interface recombination velocity. Nevertheless, the study reports an unconventional reverse phenomenon: AlGaN barrier-induced deterioration of the interface quality and acceleration of nonradiative recombination in the underlying GaN buffer. The study shows that the interface recombination is a major carrier loss mechanism in the affected interfaces, thus limiting the efficiency of a nitride-based device. These results reveal unexpected harmful processes in

seemingly-passive device elements, which are often neglected in device development.

The fourth study (Chapter D, based on Paper D) investigates basic properties of carrier recombination and diffusion in MOCVD- and MBE-grown InN epilayers with different intrinsically-high electron concentrations. In case of recombination properties, the work confidently reveals the dominant recombination mechanism (actively debated before). In case of diffusion properties, the study features remarkably high minority hole diffusion coefficients in previously unobserved electron density range. Based on this data, the study also assesses applicability of cheap MOCVD-grown InN in photovoltaics field. This work stands out for the large sample set and the application of femtosecond-resolution LITG technique, which is capable to access minority carrier dynamics unapproachable by other field-favorite experiments.

The fifth study (Chapter E; based on Paper E) investigates response of carrier dynamics in InN to extremely hostile spacelike proton irradiation, assesses material's radiation resistance, and compares it to that in the most radiation-resistant semiconductors as well as to corresponding radiation dose received in a decades-long space mission. Currently, the duration of space missions in the most severe space-bound radiation environments is vastly limited by conventional photovoltaic devices based on non-resilient semiconductors. Meanwhile, the demand for radiation-hard semiconductors is continually rising due to emerging private- and government-funded space exploration efforts. To address this demand, the study presents InN and its flagship feature – the extreme radiation resistance.

Key findings

Finding A: At the excess carrier densities below ~10^{19} cm^{-3}, internal quantum efficiency in the AlGaN alloys increases with the carrier density and the Al content due to the increasing radiative recombination rate; in the opposite wing of carrier densities, efficiency droop occurs and is governed by the density-activated nonradiative channel as well as the phase-space filling-induced saturation of the radiative recombination rate

Finding B: The photomodification of $Al_xGa_{1-x}N$ epilayers (with $x \approx 0.2 \div 0.7$) at extremely high carrier densities ($6\times10^{19} \div 3.7 \times10^{20}$ cm^{-3}) photogenerated with intense laser pulses can permanently accelerate nonradiative carrier recombination and enhance the diffusivity; the magnitude of such changes depends on the number of photomodification pulses, carrier density and the Al content

Finding C: In AlGaN/GaN heterointerfaces, interface-deteriorating defects in AlGaN barrier alter and govern the carrier dynamics in the underlying GaN buffer: the interface recombination velocity in the buffer is increased with decreasing barrier quality, and the interface recombination pathway is transformed from the insignificant to the dominant one

Finding D: In u-InN, properties of carrier dynamics are strongly bound to the total electron density (corresponding to the background and excess electrons): at densities above mid-10^{18} cm^{-3}, the diffusion coefficient increases super-linearly with increasing electron density, while the carrier lifetime decreases; the latter is governed by the direct Auger recombination and the phase-space filling phenomenon

Finding E: In proton-irradiated u-InN, displacement damage dose required for carrier lifetime deterioration exceeds that in the most radiation-resistant semiconductors; such rad-resistance originates from relatively small impact of radiation-induced defects limited to that of an electron source to the Auger process

Thesis layout

The thesis comprises an introduction, a review section for traditional and novel nitrides, a section for experimental info, and five chapters discussing the results.

The review section follows the discussion on the maturity of III-nitrides started in the introduction and elaborates on it. Further on, author's outlook on prospects of nitride research is given and future opportunities in the field of novel nitride materials are discussed.

In the experimental section, info on the studied samples is provided: growth-related details are discussed and select electrical parameters are listed. Moreover, experimental techniques, such as light-induced transient grating and photoluminescence spectroscopies, are described.

Finally, the results are dissected study by study in Chapters A-E (briefly described above). Each chapter features an opening section for addressed scientific problem, an analysis of original experimental data, concluding highlights, a key finding, and closing suggestions for future research. Chapters are arranged in a following manner: ultrawide-gap AlGaN alloys are investigated in Chapters A and B, AlGaN/GaN heterostructures with wide-gap GaN – in Chapter C, and narrow-gap InN – in Chapters D and E.

Author contribution

The vast majority of experiments and data analysis efforts discussed in the thesis were performed by the thesis author (ZP). The exceptions are credited in appropriate thesis sections. The paper manuscripts related to the thesis were either prepared by ZP, or with a heavy ZP involvement. These papers are published in *Clarivate Analytics Web of Science*-indexed journals and are listed in *Main publications* section below. The thesis results were also presented in a number of international and national-level scientific conferences listed in *Conferences* section below; there, presentations performed by ZP are highlighted in bold. A separate list (*Other publications*, see below) is given for ZP-coauthored papers not related to the thesis.

Main publications

Paper A: Podlipskas, Ž., Aleksiejūnas, R., Kadys, A., Mickevičius, J., Jurkevičius, J., Tamulaitis, G., Shur, M. S., Shatalov, M., Yang, J. & Gaska, R. Dependence of radiative and nonradiative recombination on carrier density and Al content in thick AlGaN epilayers. *Journal of Physics D: Applied Physics* **49**, 145110 (2016).

Paper B: Podlipskas, Ž., Aleksiejūnas, R., Nargelas, S., Jurkevičius, J., Mickevičius, J., Kadys, A., Tamulaitis, G., Shur, M. S., Shatalov, M., Yang, J. & Gaska, R. Photomodification of carrier lifetime and diffusivity in AlGaN epitaxial layers. *Current Applied Physics* **16**, 633–637 (2016).

Paper D: Aleksiejūnas, R., Podlipskas, Ž., Nargelas, S., Kadys, A., Kolenda, M., Nomeika, K., Mickevičius, J. & Tamulaitis, G. Direct Auger recombination and density-dependent hole diffusion in InN. *Scientific Reports* **8**, 4621 (2018).

Paper E: Podlipskas, Ž., Jurkevičius, J., Kadys, A., Kolenda, M., Kovalevskij, V., Dobrovolskas, D., Aleksiejūnas, R. & Tamulaitis, G. Extreme radiation resistance in InN. *Journal of Alloys and Compounds* **789**, 48–55 (2019).

Conferences

- Dobrovolskas, D., Podlipskas, Ž., Jurkevičius, J., Kadys, A., Kolenda, M., Kovalevskij, V., Aleksiejūnas, R. & Tamulaitis, G. Origin of extreme radiation resistance of InN. *International Workshop on Nitride Semiconductors,* Kanazawa, Japan (2018).
- **Podlipskas, Ž.**, Aleksiejūnas, R., Nargelas, S., Kadys, A., Kolenda, M., Nomeika, K., Mickevičius, J. & Tamulaitis, G. Density-dependent hole diffusion and recombination in InN. *34th International Conference on the Physics of Semiconductors,* Montpellier, France (2018).
- **Podlipskas, Ž.**, Jurkevičius, J., Kadys, A., Kolenda, M., Kovalevskij, V., Dobrovolskas, D., Aleksiejūnas, R. & Tamulaitis, G. InN – an extremely radiation-resistant semiconductor. *34th International Conference on the Physics of Semiconductors,* Montpellier, France (2018).
- **Podlipskas, Ž.**, Mickevičius, J., Riauka, M. & Aleksiejūnas, R. Krūvininkų difuzijos, gyvavimo trukmės ir lokalizacijos sąryšis AlGaN junginiuose. *42-oji Lietuvos nacionalinė fizikos konferencija*, Vilnius, Lithuania (2017).

- Jurkevičius, J., Dobrovolskas, D., Podlipskas, Ž., Nomeika, K., Kolenda, M., Kadys, A., Malinauskas, T., Mickevičius, J., Aleksiejūnas, R. & Tamulaitis, G. InN sluoksnių auginimas impulsiniu MOCVD metodu. *42-oji Lietuvos nacionalinė fizikos konferencija*, Vilnius, Lithuania (2017).
- **Podlipskas, Ž.**, Nomeika, K., Kadys, A., Miasojedovas, S. & Aleksiejūnas, R. Two-way connection between quality of layers in AlGaN/GaN template. *International Workshop on Nitride Semiconductors*, Orlando FL, USA (2016).
- Nomeika, K., Podlipskas, Ž., Aleksiejūnas, R., Dargis, D., Ščajev, P., Nargelas, S. & Jarašiūnas, K. Carrier diffusivity as the key parameter behind the peak quantum efficiency in (In,Ga)N quantum structures. *International Workshop on Nitride Semiconductors*, Orlando FL, USA (2016).
- **Podlipskas, Ž.** Two-way connection between quality of layers in AlGaN/GaN template. *Open Readings 2016*, Vilnius, Lithuania (2016).
- Aleksiejūnas, R., Podlipskas, Ž., Nargelas, S., Jurkevičius, J., Mickevičius, J., Tamulaitis, G., Kadys, A., Shur, M. S., Shatalov, M., Yang, J. & Gaska, R. Permanent modification of excess carrier lifetime and diffusivity by intense laser illumination in AlGaN. *11th International Conference on Nitride Semiconductors*, Beijing, China (2015).
- **Podlipskas, Ž.**, Aleksiejūnas, R., Nargelas, S., Jurkevičius, J., Mickevičius, J., Tamulaitis, G., Kadys, A., Shur, M. S., Shatalov, M., Yang, J. & Gaska, R. Nepusiausviruųjų krūvininkų gyvavimo trukmės ir difuzijos koeficiento ilgalaikė modifikacija intensyvia lazerine spinduliuote AlGaN sluoksniuose. *41-oji Lietuvos nacionalinė fizikos konferencija*, Vilnius, Lithuania (2015).
- **Podlipskas, Ž.** Impact of laser-induced optical annealing to recombination and diffusivity of excess carriers in AlGaN. *Open Readings 2015*, Vilnius, Lithuania (2015).

- Saxena, T., Shur, M., Nargelas, S., Podlipskas, Ž., Aleksiejūnas, R., Tamulaitis, G., Shatalov, M., Yang, J. & Gaska, R. Dynamics of nonequilibrium carrier decay in AlGaN epitaxial layers with high aluminum content. *Optics Express* **23**, 19646–19655 (2015).
- Mickevičius, J., Podlipskas, Ž., Aleksiejūnas, R., Kadys, A., Jurkevičius, J., Tamulaitis, G., Shur, M. S., Shatalov, M., Yang, J. & Gaska, R. Nonradiative recombination, carrier localization, and emission efficiency of AlGaN epilayers with different Al content. *Journal of Electronic Materials* **44**, 4706–4709 (2015).

The maturity of nitrides

Victories, defeats and trends

Studies on the conventional III-nitride semiconductors (InN – GaN – AlN) performed for three decades have rendered some of the family members technologically mature, and the strongest example of a mature nitride is InGaN tailored for a blue LED.

The development of a blue LED was remarkably fast: in the first three years, the external quantum efficiency (EQE) for a blue LED was enhanced from 0.18% (in 1991)[13] to 2.7% (in 1994),[14] and commercial LED was launched. At this stage, single-digit EQE values were sufficient for a commercially feasible product due to lack of reliable alternatives in the market. Fast forward to 2010, EQE of 86% for a blue LED was reached.[15] Meanwhile, progress in development of a more challenging InGaN-based green LED is similarly impressive despite very limited R&D[16] (compared to that for blue LEDs): currently, academia boasts about EQE values reaching 56% in a green LEDs (2019 data),[17,18] while industry (*Osram* specifically) – about a significant 40% jump in efficiency of direct-emitting green LEDs (compared to that of predecessor products across the entire company portfolio; 2018 data).[19]

Another example of a mature nitride system is GaN/AlGaN heterostructure with low Al fractions in AlGaN layer tailored for a high electron mobility transistor (HEMT). The first nitride HEMT was fabricated in 1993[20] without the fundamental understanding about the origin of two-dimensional electron gas (2DEG) in AlGaN/GaN heterointerface. By 1999-2001, the situation improved, and mechanisms controlling 2DEG density and mobility were described.[21–27] Later, after numerous delays, nitride HEMTs were commercialized: around 2006, HEMTs grown on SiC wafers (by *Eudyna*[28] and possibly other companies); and by 2008, HEMTs on Si (by *Nitronex*[29] and others).

AlGaN alloys with moderate Al fractions also received a fair share of scientific attention, stimulating rapid advancements in select applications. For instance, UV-C AlGaN LEDs emitting in spectral range of 275-280 nm and addressing in demand germicidal applications demonstrate leaps in performance comparable to that in green LEDs. From 2002 to 2004, EQE in AlGaN-based LEDs emitting at 280 nm increased more than tenfold: from 0.01-0.1% in the very first reported LED[30] to ~1%[31] in [already] commercial product. By 2012, EQE of 10-12% and the output power of 9-30 mW was reached in LED emitting at 278 nm;[32] and in 2017, EQE of 20% was achieved

in (18-44)-mW LED emitting at 275 nm.[33] By 2018, single-chip 100-mW LEDs emitting at 278 nm for 10'000 hours were available for sale from *LG Innotek*.[34,35]

Despite the apparent success in AlGaN development targeting LEDs in 275-280 nm spectral range, AlGaN alloys with moderate-to-high Al fractions are regarded as immature due to lagging efficiencies in the UV-B and the remainder of UV-C regions as well as due to problematic growth aimed for high Al fractions.[5] Development of AlGaN-based UV laser diodes (LDs) also proved to be challenging. Currently, the shortest wavelength achieved in a planar electrically injected AlGaN LD is 336 nm (UV-A spectrum).[36] Meanwhile, electrically pumped UV-B and UV-C lasing (at 289, 262, and 239 nm)[37–39] was attained only in MBE-grown (abbr. of Molecular beam epitaxy) AlGaN nanowire (NW) lasers, which are difficult to fabricate in high volume.

AlN is also regarded as immature semiconductor hindered by lack of a good acceptor and even a donor.[5] To date, only sulfur is postulated as a likely shallow donor for AlN,[40] with no shallow acceptors suggested. Despite this drawback, planar p-i-n AlN LED (with turn on voltage >20 V) was fabricated:[41] p- and n-type conductivity was achieved by brute-force doping with Mg acceptor (concentration up to 4×10^{19} cm^{-3}) and Si donor (up to 2×10^{18} cm^{-3}), yielding 10^{10}-10^{11} cm^{-3} free hole and mid-10^{15} cm^{-3} free electron concentrations. Significantly higher carrier concentrations can be reached with the same dopants in nanowire-based AlN, e.g., hole concentration of 10^{16} cm^{-3} was attained in MBE-grown AlN-on-Si nanowire LED with bandgap-limited turn on voltage of 6 V.[42] This example shows a rather compelling approach for fabrication of AlN devices even in the infancy of AlN doping. A similar nanowire-based doping strategy can be used for InN devices as well (see further).

The most immature and the least popular conventional III-nitride is InN. The low level of attention to InN is evident from a relatively low annual quantity of studies on this topic. The *Web of Science* (WoS)[43] data in Figure 1 show that the number of published papers mentioning InN peaked at ~400 per year (in 2008), while number of papers mentioning other III-nitrides ranged from ~900 to 4000 in the best respective years (2013-to date). Since 2008, the interest in InN has only declined, and the annual quantity of studies has decreased down to ~250 (in 2017) – a substantially lower number compared to that for the second least popular III-nitride, InGaN (~660 published papers in 2017). While a decrease in attention to InGaN may be a result of its maturity, neglect of InN may be caused by the absence of necessary

breakthroughs in InN research during the prime of III-nitride development. For instance, the first electroluminescence (EL) in InN-based device was observed as late as 2007;[44] the first solar cell and LEDs were fabricated in 2011 and 2012, respectively;[45–47] and the first stimulated emission (SE) in planar InN was demonstrated in 2018[48] (in comparison, lasing in planar AlN was reported in 2006)[49] — almost all of these important breakthroughs occurred after the interest peak (see Figure 1).

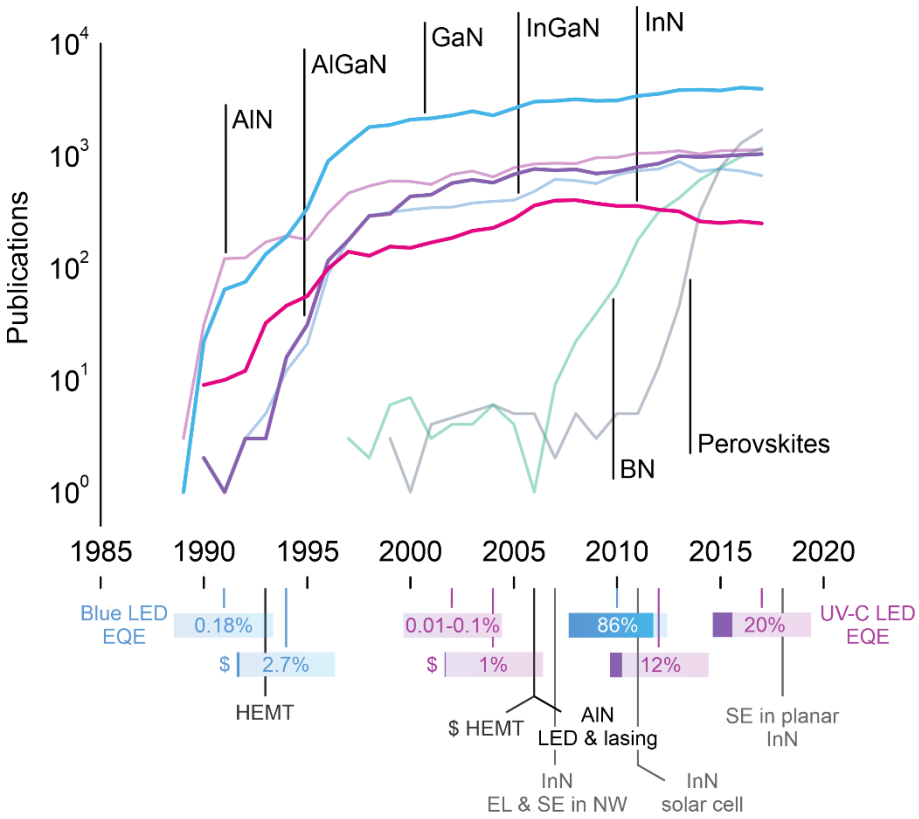

Figure 1. Top – annual number of WoS-indexed articles mentioning nitride- and perovskite-based semiconductors vs. years.[b] Bottom – progress in efficiency of blue InGaN- and UV-C (275-280 nm) AlGaN-based LEDs; notable breakthroughs in nitride research; and launch dates for commercial devices (noted with '$').

[b] Search performed using *Clarivate Analytics Web of Science* database. Search terms for each curve: AlN – AlN NOT ceramics; AlGaN – AlGaN; GaN – GaN; InGaN – InGaN; InN – InN (select journal categories); BN – 'boron nitride' AND graphene; Perovskites – perovskite AND ['solar cell' OR photovoltaic].

The slow development of InN has been caused by multitude of problems mostly related to unintentional doping leading to doping-dependent variation in band-gap (E_g);[50,51] surface electron accumulation[52] and propensity to extreme free electron concentrations; as well as ineffectiveness of p-type doping.[53,54] Some of these difficulties have been overcome. Firstly, the phenomenon of band-gap variation was understood (by the year 2002), and the fundamental E_g value has been established (~0.7 eV instead of initially estimated ~2 eV).[51] Secondly, unintentional free electron concentration has been reduced down to $3\text{-}4\times10^{17}$ cm^{-3} by employing MBE technique and growing thicker layers (up to 7.5 μm).[51] However, p-type doping of InN has still not been mastered, and p-InN in InN-based devices usually has been substituted by other materials or engineered with a help of complicated workarounds. For instance, p-type conductivity in InN-based planar LEDs has been achieved with p-GaN layer[46] and p-NiO layer;[55,56] in InN-based planar solar cell – with p-GaN layer;[57] in InN nanodots-based LED – with p-Si layer;[47] while in InN nanowire-based transistor,[44] LED,[58] and solar cell[45] – with p-InN nanowires. Unfortunately, InN will probably remain rather abandoned by scientific community until a planar p-InN of acceptable conductivity is demonstrated or other applications are found. In contrast, AlN has gained a great deal of attention (gauged by the quantity of articles; see AlN curve in Figure 1) despite the underdeveloped doping. This is a result of AlN capacity to be used as a passive component in nitride-based devices, e.g., as a buffer, substrate, barrier in LEDs, and an insulator in transistors — the advantage InN lacks.

The future of nitrides

The nitrides are dead, long live the nitrides!

While academia attention is saturating or even declining for some of the conventional III-nitrides, the interest in select novel nitrides and other similar yet modern materials is booming. One of these materials is BN (specifically hexagonal BN form (hBN)), applications of which are compatible both with the traditional III-nitrides and the trending family of ultrathin 2D nanomaterials (graphene, transition metal dichalcogenides (TMDCs)). In the case of traditional III-nitrides, hBN can be used as a buffer and a release layer for growth and mechanical transfer of GaN-based devices.[59] Regarding the 2D nanomaterials, hBN performs as an essential building block for van der Waals heterostructures, such as graphene- or TMDC-based capacitors, transistors, LEDs, plasmonic devices, photodetectors, and solar cells (curious reader can find the data on these devices and relevant references in the

reviews[60–63]). Such remarkable versatility of hBN already generates the annual quantity of papers rivaling that for the traditional III-nitrides (see Figure 1).

Hybrid organic-inorganic perovskites (HOIPs) also deserve a place in this discussion due to their recent surge in recognition (see Figure 1) and peculiar resemblance to nitrides. The ~180-year old ABX_3 perovskite architecture (where A stands for metal or organic cation; B – metal cation; and X for halide, formate, azide, or other anion) accommodates a huge material class exhibiting diverse physical properties.[64] Despite this diversity, current research tends to focus specifically on metal halide HOIPs because of their promising photovoltaic applications.[65–70] Conveniently for this analysis, a handful of HOIPs (lead halide-based and possibly others) share numerous electronic properties and phenomena with conventional III-nitrides, i.e., both material systems feature disorder-induced carrier localization; degeneracy- and localization-governed carrier diffusivity; efficiency droop driven by density-dependent nonradiative recombination; etc.[71,72] Interesting properties may also manifest in a completely new class of nitride perovskites ABN_3, where A and B are metal cations, and N is nitride anion instead of halide. However, these materials (including $TaThN_3$,[73] $LaReN_3$, $YReN_3$, and $LaWN_3$[74]) are only computationally predicted and not yet synthesized.

Although the discussed modern materials attract a healthy amount of attention, cover an expanding range of applications, and are capable to solve a multitude of problems, a future even more interesting and important material systems are being designed already. These novel materials, including nitrides, are being discovered using high-throughput (HT) computational material design approach, which combines advanced computational quantum-mechanical-thermodynamic methods (such as combinatorial calculations driven by density functional theory (DFT)[75,76]) with intelligent data-mining[77–79] and database construction.[80] Such marriage of different fields enables generation, management and analysis of enormous data repositories[c] for the

[c] The *Materials Project* at www.materialsproject.org

The *AFLOW Distributed Materials Property Repository* at www.aflowlib.org, where AFLOW stands for Automatic-FLOW for Materials Discovery

The *Open Quantum Materials Database (OQMD)* at www.oqmd.org

The *Electronic Structure Project (ESP)* at gurka.fysik.uu.se/ESP/

The *Open Materials Database* at www.openmaterialsdb.se

The *Novel Materials Discovery (NOMAD)* Repository at repository.nomad-coe.eu

The *Theoretical Crystallography Open Database (TCOD)* at www.crystallography.net/tcod

'learning' of crystallization rules and prediction of novel materials at drastically accelerated rates (see reviews[2,75,81–83] for more info). For instance, HT material design approach fused with machine learning model can accelerate screening of 1.6 million ternary materials (in unconstrained composition space) from tens of thousands of CPU-years to merely minutes (compared to ground state DFT calculations and excluding the 'training' time).[84] In case of nitride screening, HT material design strategy has fueled increase in nitride discovery from single digits per year (e.g., discovery rate of M_1-M_2-N chemical spaces was ~3.3 per year in the period from 1927 to 2015; M stands for metal)[85] to tens and hundreds of new nitride compounds per study.[85–87] In one of these studies, Sun et al.[85] have predicted 203 new stable and 303 metastable ternary nitride compounds within 92 new stable and 563 metastable M_1-M_2-N spaces.

Novel nitrides predicted, synthesized or characterized using HT material design approach include Cu_3N;[88] Sn_3N_4;[89] $ZnSnN_2$;[90] $CuTaN_2$, $CuNbN_2$, $Cu_3Ga_2N_3$, and $Cu_3In_2N_3$;[91] $CaZn_2N_2$;[92] $Mg_{G\text{-}3}TMN_{G\text{-}2}$ (*TM* = Ti, Zr, Nb, Hf);[87] Zn_2SbN_3, Zn_3WN_4, and Zn_3MoN_4;[85] and hundreds of others. A multitude of these compounds as well as not yet discovered future nitrides seem to have potential for integration into contemporary optoelectronic devices and for replacement of traditional III-nitrides with problematic compositions and properties. Firstly, numerous novel nitrides are lattice-compatible with the traditional III-nitrides (see the obligatory *band-gap engineering* depiction in Figure 2) and feature band-gaps overlapping with technologically-important band-gap regions (e.g., *green gap*, Shockley-Queisser energy range[93]). Secondly, select novel nitrides are less susceptible to problems plaguing the traditional III-nitrides; for instance, Cu_3N[94] and $CaZn_2N_2$[92] are not deprived of the infamous p-type conductivity. Nevertheless, the novel nitrides (including these few rather randomly introduced ones) have limitations of their own and have not yet realized their promise of tailor-made remedy semiconductors.

At this moment, HT discovery of an optimal nitride fitting a targeted application is more accidental than intended. A more accurate/purposeful compound search (and finally – design) needs systematic understanding of materials,[95–98] i.e., extraction of chemical rules or data-mined statistical patterns describing origin of required properties. Unfortunately, relatively low exploration level of nitride space (~3'000 unique nitride compounds catalogued in the Inorganic Crystal Structure Database[1] vs. >41'000 oxides; mid 2015 data)[2] hampers this type of studies. Research on doping, photoexcited and electrically injected carrier properties, carrier dynamics,

interfacial phenomena, etc. in novel nitrides also lacks. Fortunately, many valuable insights on such studies can be gained from researchers working on the established III-nitrides.[2]

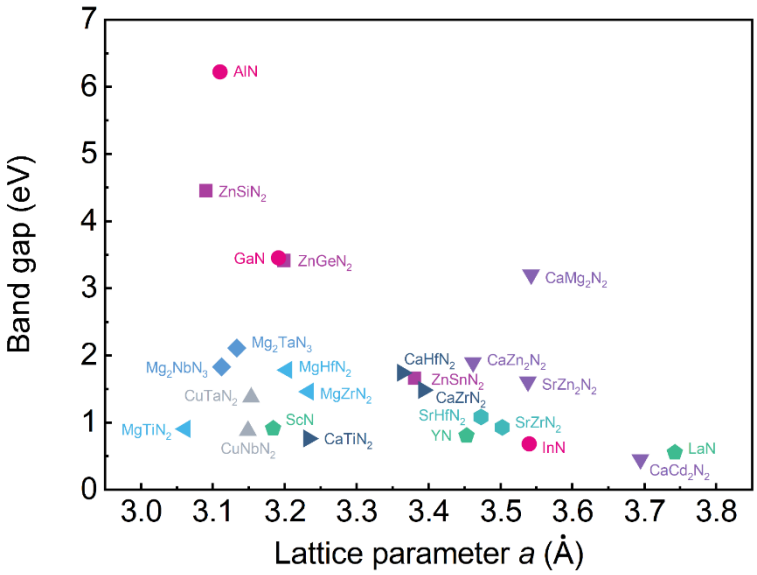

Figure 2. Band-gap vs. lattice parameter *a* for traditional III-nitrides as well as novel nitride materials studied using HT material design approach; values are taken from Refs.[87,91,92,99]

In the future, nitride research could greatly benefit from the increased interaction between the fields of traditional and novel nitrides. On the one hand, the continuously expanding list of novel nitride semiconductors could be exploited for improvement of current III-N-based optoelectronic devices. On the other hand, lessons learned from the mature III-nitrides could be adapted in the basic research of novel nitrides, thus providing materials with fully controlled optoelectronic properties and perfectly fitting the targeted devices.

Therefore, one can argue that the declining academia attention to the traditional III-nitrides will not render these studies obsolete, and that the available III-nitride research will kickstart the future studies on novel nitride materials.

Experimental

Samples

In the thesis, AlGaN and InN samples will be identified by the following basic parameters: Al content[d] (x), localization depth (σ), which stands for the standard deviation of the Gaussian distribution for the band-tail density of states – for AlGaN epilayers; background electron concentration (N_e) – for InN epilayers. These parameters and other sample properties, such as layer thickness or buffer state (present/absent), as well as select growth-related details are summarized in Table 1 and Table 2 for AlGaN- and InN-based samples, respectively.

$Al_xGa_{1-x}N$/GaN heterostructures were grown by Dr. Arūnas Kadys (Institute of Photonics and Nanotechnology, Vilnius University, Lithuania) on a c-plane sapphire using an *Aixtron* close-coupled showerhead 3×2" metalorganic chemical vapor deposition (MOCVD) reactor. $d = 130 \div 300$-nm thick $Al_xGa_{1-x}N$ barriers were grown at identical temperature and identical tri-methyl-aluminum (TMAl) flow rate (1090 °C and 1.21×10^{-5} mol/min, respectively); the Al content was controlled by changing the tri-methyl-gallium (TMGa) flow rate (listed in Table 1). Three sample sets with different barrier Al content were obtained: $\bar{x}$ = (0.13, 0.2, or 0.34), with $\lesssim$10% relative variation in x within a sample set. This variation is an unintentional side effect occurring due to changes in ammonia flow rate: lower ammonia flow rate (higher NH_3 deficiency) results in higher portion of stronger Al-N bonds compared to Ga-N. The ammonia flow rate was varied intentionally to obtain different barrier structural quality between the samples. Meanwhile, 4-µm thick GaN buffers were grown under identical conditions (T = 1080 °C, TMGa flow rate of 1.77×10^{-4} mol/min, NH_3 flow rate of 0.232 mol/min) for every sample. AlGaN barriers and GaN buffers for all $Al_xGa_{1-x}N$/GaN samples were grown under continuous gas flow. All of these samples were employed to study carrier dynamics in the AlGaN/GaN interface as described in Chapter C; select few AlGaN barriers were also exploited in studies on carrier recombination (Chapter A) and photomodification phenomenon (Chapter B) in AlGaN alloys.

[d] Al content for AlGaN epilayers was either disclosed by the sample provider or estimated from X-ray diffraction measurements performed by Dr. Tadas Malinauskas (Institute of Photonics and Nanotechnology, Vilnius University, Lithuania) and Dr. Sandra Stanionytė (Center for Physical Sciences and Technology, Lithuania)

Table 1. Electrical parameters and growth-related details for AlGaN epilayers in the studied AlGaN-based samples.

Sample	σ (meV)	d (nm)	Growth method	TMGa (mol/min)	NH_3 (mol/min)
$Al_{0.11}Ga_{0.89}N$/GaN		300	MOCVD	1.25×10^{-4}	0.223
$Al_{0.12}Ga_{0.88}N$/GaN		300	MOCVD	1.25×10^{-4}	0.179
$Al_{0.13}Ga_{0.87}N$/GaN		300	MOCVD	1.25×10^{-4}	0.134
$Al_{0.14}Ga_{0.86}N$/GaN	13	300	MOCVD	1.25×10^{-4}	0.089
$Al_{0.19}Ga_{0.81}N$/GaN		300	MOCVD	7.76×10^{-5}	0.112
$Al_{0.20}Ga_{0.80}N$/GaN	21	300	MOCVD	7.76×10^{-5}	0.089
$Al_{0.21}Ga_{0.79}N$/GaN		300	MOCVD	7.76×10^{-5}	0.067
$Al_{0.32}Ga_{0.68}N$/GaN		130	MOCVD	3.84×10^{-5}	0.112
$Al_{0.33}Ga_{0.67}N$/GaN	30	130	MOCVD	3.84×10^{-5}	0.089
$Al_{0.34}Ga_{0.66}N$/GaN		130	MOCVD	3.84×10^{-5}	0.067
$Al_{0.35}Ga_{0.65}N$/GaN		130	MOCVD	3.84×10^{-5}	0.045
$Al_{0.38}Ga_{0.62}N$/GaN		130	MOCVD	3.84×10^{-5}	0.022
$Al_{0.46}Ga_{0.54}N$		700	MOCVD	6.65×10^{-5}	0.179
$Al_{0.48}Ga_{0.52}N$	45	1000	MEMOCVD		
$Al_{0.60}Ga_{0.40}N$	48	1000	MEMOCVD		
$Al_{0.60}Ga_{0.40}N$	57	1000	MEMOCVD		
$Al_{0.60}Ga_{0.40}N$	60	1000	MEMOCVD		
$Al_{0.60}Ga_{0.40}N$	60	1000	MEMOCVD		
$Al_{0.64}Ga_{0.36}N$	34	1000	MEMOCVD		
$Al_{0.65}Ga_{0.35}N$	50	1000	MEMOCVD		
$Al_{0.68}Ga_{0.32}N$	65	1000	MEMOCVD		
$Al_{0.71}Ga_{0.29}N$	50	1000	MEMOCVD		

$Al_{0.46}Ga_{0.54}N$ epilayer of 700 nm thickness was grown by Dr. Arūnas Kadys on c-AlN/sapphire template using the same MOCVD reactor. The following growth conditions were applied: T = 1090 °C, TMAl flow rate of 3.23×10^{-5} mol/min, TMGa flow rate of 6.65×10^{-5} mol/min, and NH_3 flow rate of 0.179 mol/min. This sample was exploited for the study on AlGaN photomodification discussed in Chapter B.

The remaining ~1-µm thick **$Al_xGa_{1-x}N$ epilayers with $x \geq 0.48$** were grown using migration-enhanced MOCVD (MEMOCVD) technique on 0.6 – 8-µm thick AlN buffers deposited on c-sapphire. The samples were provided by *Sensor Electronic Technology, Inc.* (SETi) without disclosing growth-related details. These epilayers were employed in studies on carrier recombination (Chapter A) and photomodification phenomenon (Chapter B) in AlGaN alloys.

Table 2. Electrical parameters and growth-related details for as-grown InN epilayers.

Sample	N_e (cm^{-3})	d (nm)	Buffer	Growth method	Gas flow	Growth T
	5.1×10^{19}	300	✓	MOCVD	pulsed	constant
	4.7×10^{19}	300	✓	MOCVD	pulsed	constant
	4.7×10^{19}	300	✓	MOCVD	pulsed	constant
	4.5×10^{19}	300	✓	MOCVD	pulsed	constant
	4.4×10^{19}	300	✓	MOCVD	pulsed	constant
	4.2×10^{19}	300	✓	MOCVD	pulsed	constant
	3.5×10^{19}	26	✓	MOCVD	pulsed	ramped
S2	$(3.4/5.9)\times10^{19}$	300	✓	MOCVD	pulsed	constant
	3.1×10^{19}	300	✓	MOCVD	pulsed	constant
	3.0×10^{19}	79	✓	MOCVD	pulsed	ramped
	2.3×10^{19}	300	✓	MOCVD	pulsed	constant
	2.3×10^{19}	300	✓	MOCVD	pulsed	constant
	1.5×10^{19}	158	✓	MOCVD	pulsed	ramped
S3	$(1.3/1.9)\times10^{19}$	390	×	MOCVD	cont.	constant
	1.1×10^{19}	326	✓	MOCVD	cont.	ramped
	9.0×10^{18}	300	✓	MOCVD	pulsed	ramped
	8.8×10^{18}	236	✓	MOCVD	pulsed	ramped
S1	$(8.0/13)\times10^{18}$	300	✓	MOCVD	pulsed	ramped
	6.8×10^{18}	315	✓	MOCVD	pulsed	ramped
	6.8×10^{18}	315	✓	MOCVD	pulsed	ramped
	6.2×10^{18}	394	✓	MOCVD	pulsed	ramped
	1.4×10^{18}	2300	✓	MBE		

A set of **InN** epilayers comprising 21 sample (see Table 2) was grown by Dr. Arūnas Kadys and Marek Kolenda (Institute of Photonics and Nanotechnology, Vilnius University, Lithuania) on c-sapphire using the previously described MOCVD reactor. The 30 – 400-nm thick InN epilayers were deposited either on 5-μm thick GaN buffers or directly on sapphire. The growth temperature ranged from 570 to 630 °C and was either maintained constant or ramped up during the growth. The ammonia flow rate (0.268 mol/min) was identical for all InN epilayers, while the tri-methyl-indium (TMIn) flow rate was equal to 2.69×10^{-5} mol/min or to 3.36×10^{-5} mol/min. Both continuous and pulsed precursor delivery methods were exploited with different pulse (7 ÷ 21 s) and pause (5 ÷ 20 s) durations between the samples. The variation of described growth conditions yielded unintentionally doped InN epilayers with the background electron concentration ranging from 6×10^{18} cm^{-3} to 5×10^{19} cm^{-3}. The electron concentration was extracted from Hall measurements in van der Pauw geometry performed by Dr. Arūnas Kadys and Dr. Ignas Reklaitis (Institute

of Photonics and Nanotechnology, Vilnius University, Lithuania). These samples were employed to study carrier dynamics in as-grown InN epilayers as discussed in Chapter D.

Three samples (**S1, S2, and S3;** noted in Table 2) with different structural quality and background electron concentration were selected for the further study exploring proton-irradiation impact on carrier dynamics in InN (Chapter E). In this study, the selected samples were cut into several fragments of similar size for the irradiation procedure. Next, Hall electron concentration was remeasured. Due to smaller surface area of new sample fragments and effectively larger contact area,[100] new Hall N_e values for as-grown epilayers were up to 70% higher than those in the Chapter D study. This discrepancy is noted in Table 2.

Finally, **the thickest (2.3 μm) and highest quality ($N_e = 1.4\times10^{18}$ cm^{-3}) InN** epilayer (see Table 2) was grown by Theodore D. Moustakas team (Boston University, MA, USA) on c-sapphire using RF (radio frequency) plasma-assisted MBE technique. This sample was investigated in the Chapter D study.

Techniques

Quasi-stationary photoluminescence spectroscopy

Localization depth σ for AlGaN epilayers was estimated from temperature dependence of photoluminescence (PL) peak shift assessed under quasi-steady-state conditions. An example of typical PL spectra for the studied epilayers is demonstrated in Figure 3. This set of spectra was measured for $Al_{0.48}Ga_{0.52}N$ epilayer at temperatures ranging from 8 to 300 K and features a sequence of red-blue-red peak shifts with increasing temperature. The initial, low-temperature, redshift is generally attributed to the carrier freeze-out phenomenon.[101,102] In this case, carriers (excitons) have enough energy to leave shallower localized states and hop into regions of deeper potential minima, but not vice versa. The latter blue and red shifts occur due to temperature-induced carrier delocalization and band-gap narrowing, respectively. These high-temperature PL peak shifts can be quantitatively described using Eliseev's band-tail-filling model and a simple Varshni-like expression:[103]

$$E(T) = E_g(0) - \frac{\alpha T^2}{\Theta + T} - \frac{\sigma^2}{k_B T} \quad (1)$$

where E is PL peak energy, $E_g(0)$ is band-gap at 0 K, α is Varshni parameter, Θ is material-specific Debeye temperature, and localization depth σ is defined

as the standard deviation of the Gaussian distribution for the band-tail density of states. For $Al_{0.48}Ga_{0.52}N$ epilayer, a fit to the experimental data was obtained with $\sigma = 45$ meV (see the inset in Figure 3). For other studied AlGaN epilayers, σ values were estimated using the same basic approach and are listed in Table 1.

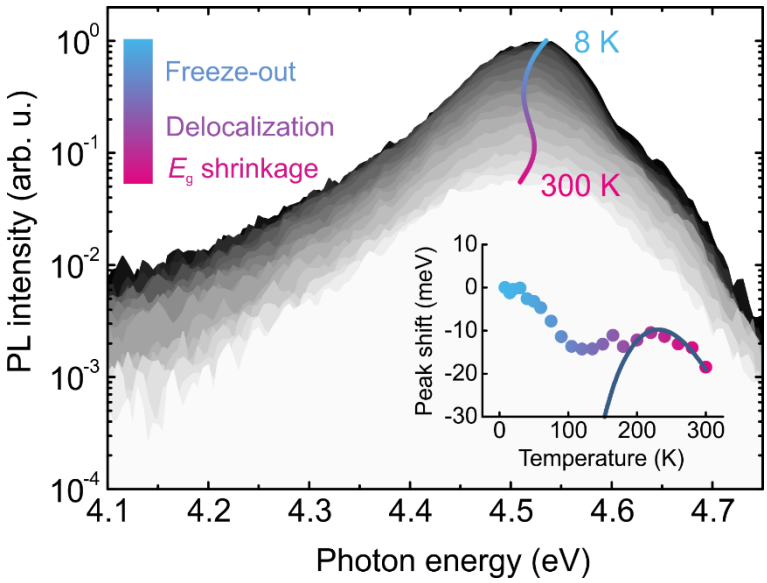

Figure 3. PL spectra measured at various temperatures for $Al_{0.48}Ga_{0.52}N$ epilayer. In the inset – temperature dependence of PL peak shift; line denotes the fit according to Eq. (1).

A more complex *localized-state ensemble* model by Li et al.[104] can describe PL peak shifts in a wider temperature range, including the low-temperature redshift region. Recently, this model was exploited by Wang et al.[105] to study InGaN/GaN multiple quantum wells, where high-temperature blueshift was attributed to a high-energy *blue* localization center, and low-temperature redshift – to a low-energy *red* localization center. Nevertheless, this approach was disregarded in the thesis due to its complexity.

Quasi-stationary PL measurements discussed in the thesis were performed by Dr. Jūras Mickevičius and Dr. Jonas Jurkevičius (Institute of Photonics and Nanotechnology, Vilnius University, Lithuania); only AlGaN-based samples were characterized. A Q-switched YAG:Nd laser (*Ekspla*) emitting 4-ns-duration pulses at 10 Hz repetition rate was used for the excitation: the 4th harmonic (266 nm) for AlGaN epilayers with $x \leq 0.33$, and the 5th harmonic (213 nm) for $x \geq 0.48$. The PL signal was detected using a UV-enhanced photomultiplier, analyzed using a double monochromator and

processed using a boxcar integrator. A closed-cycle helium cryostat ensured a variation and stabilization of temperature in the range from 8 to 300 K. PL measurements for evaluation of IQE (internal quantum efficiency; Chapter A) were performed in the range of excitation power density from 10 to 9000 kW/cm^2, while measurements for σ estimation (Chapter A and B) and for the investigation of photomodification phenomenon (Chapter B) were performed in a lower end of the given density range. Photomodification of $Al_{0.71}Ga_{0.29}N$ epilayer for PL characterization (Chapter B) was performed at 11 MW/cm^2.

Time-resolved photoluminescence spectroscopy

Time-resolved photoluminescence spectroscopy (TRPL) was employed to investigate carrier recombination in AlGAN/GaN interface (Chapter C). The TRPL experiment was performed using *Ekspla* Nd:YAG laser (emitting 25-ps-duration pulses at 10 Hz repetition rate) for sample excitation and a *Hamamatsu* streak camera with an *Acton* monochromator for PL signal detection. Different excitation configurations using 266 nm and 355 nm pulses were employed and are described in detail in Chapter C. Recombination processes were observed at various excitation energy fluences spanning from 3 μJ/cm^2 to 1 mJ/cm^2. Measurements were performed by the thesis author with a help from Dr. Saulius Miasojedovas (Institute of Photonics and Nanotechnology, Vilnius University, Lithuania).

Light-induced transient gratings

Light-induced transient grating (LITG) technique was employed to study carrier recombination and diffusion in both AlGaN- and InN-based sample sets. These results form a backbone of the thesis and are featured in all thesis chapters. All LITG measurements were performed by the thesis author.

In the LITG experiment, semiconductor is photoexcited with a light interference pattern, which induces a spatial modulation of a refractive index performing as a transient diffraction grating. This grating decays due to carrier recombination and diffusion processes, both of which can be evaluated by monitoring a diffraction of a delayed probe beam. Configuration of a recording pump and diffracting probe beams in LITG experiment is demonstrated in Figure 4a. Two coherent pump pulses (see purple beams) are focused on the same sample spot with the intersection angle Θ. These beams interfere with each other and form a following pattern of light field intensity:

$$I(x) = I_0\left(1 + m\cos\frac{2\pi}{\Lambda}x\right) \quad (2)$$

where $I_0 = I_1 + I_2$ is the sum intensity of both pump beams, $m = 2\sqrt{I_1 I_2}/(I_1 + I_2)$ is the modulation depth of the interference field, and $\Lambda = \lambda/(2\sin\Theta/2)$ is the field fringe spacing defined by the excitation wavelength λ and the angle Θ. The absorbed interference field creates a transient pattern of the spatially modulated density of the photoexcited carriers ΔN. The carrier density modulation causes a spatial modulation of the refractive index change, Δn, which is proportional to ΔN:

$$\Delta n = \Delta N n_{eh} \quad (3)$$

where n_{eh} is the refractive index change induced by one excess electron-hole pair. Thus, a transient diffraction grating is recorded. The grating decay is monitored by the diffraction of a delayed probe pulse (see pink beams in Figure 4a) in the transparency region of the sample. The diffraction signal is gauged by the diffraction efficiency, η – the ratio between the diffracted and transmitted probe beam intensities. In the case of strongly absorbed excitation pulses (thin transient gratings), diffraction efficiency is proportional to the excess carrier density squared $\eta \propto \Delta N^2$.

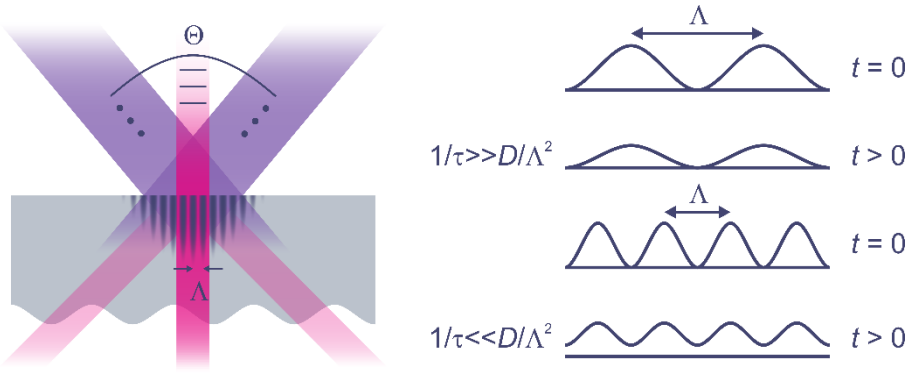

Figure 4. a) Configuration of the recording pump (purple) and diffracting probe (pink) beams in a light-induced transient grating experiment; symbols '●' and '—' denote *s* and *p* polarization, respectively. **b)** Grating profiles at different decay stages ($t = 0$ and $t > 0$) caused by carrier recombination (top) and diffusion (bottom).

The decay of diffraction grating is caused by two effects: excess carrier recombination and diffusion. Carrier recombination reduces mean carrier density without affecting grating modulation depth, while diffusion homogenizes the carrier spatial distribution (reduces modulation depth) without affecting mean carrier density; grating profiles for both of these cases

are depicted in Figure 4b. The dynamics of carrier recombination and diffusion can be described by an *ABC* model:

$$\frac{\partial N(x,z,t)}{\partial t} = \nabla[D\nabla N(x,z,t)] - \frac{N(x,z,t)}{\tau_{SRH}} - BN^2(x,z,t) - CN^3(x,z,t) + G(x,z,t) \quad (4)$$

with boundary conditions

$$\left.\frac{\partial N(x,z,t)}{\partial z}\right|_{z=0} = \frac{S_1 N(x,0,t)}{D}$$

$$\left.\frac{\partial N(x,z,t)}{\partial z}\right|_{z=d} = -\frac{S_2 N(x,d,t)}{D}$$

where D is ambipolar diffusion coefficient, τ_{SRH} is Shockley-Read-Hall (SRH) recombination time, B is bimolecular/radiative recombination coefficient, C is Auger recombination coefficient, $G(x, z, t)$ is spatially modulated carrier generation rate, $S_{1(2)}$ is recombination velocity for front (back) sample surface or interface, and d is sample thickness. In a simplified case, assuming that B, C and S recombination terms are absent, and $G(x, z, t)$ is a periodic Dirac delta function, Eq. (4) can be solved analytically:

$$N(x,t) = N_0\left[1 + exp\left(-\frac{4\pi^2 D}{\Lambda^2}t\right) cos\frac{2\pi}{\Lambda}x\right] exp\left(-\frac{t}{\tau_{SRH}}\right) \quad (5)$$

where N_0 stands for initial mean carrier density. Based on this solution, a relation between the grating decay time, τ_G, carrier lifetime, and diffusion coefficient is described as follows:

$$\frac{1}{\tau_G} = \frac{1}{\tau_{SRH}} + \frac{4\pi^2 D}{\Lambda^2} \quad (6)$$

To extract τ_{SRH} and D values, τ_G is measured at different grating periods, Λ, which are varied by adjusting the angle Θ between the interfering beams. Grating decay time τ_G is assessed by fitting LITG transient with an exponential function $\eta \propto \exp(-2t/\tau_G)$. In cases where carrier dynamics are governed by several recombination channels or single density-dependent channel, τ_{SRH} in Eq. (6) is replaced by an instantaneous effective carrier lifetime, τ, extracted at a select delay, t. The model procedure for D evaluation and typical LITG transients recorded at several grating periods (Λ = 1.9 – 7.9 μm) for one of the $Al_xGa_{1-x}N$/GaN samples are demonstrated in Figure 5. LITG-related equations introduced here as well as detailed description of LITG technique can be found in Ref.[106]

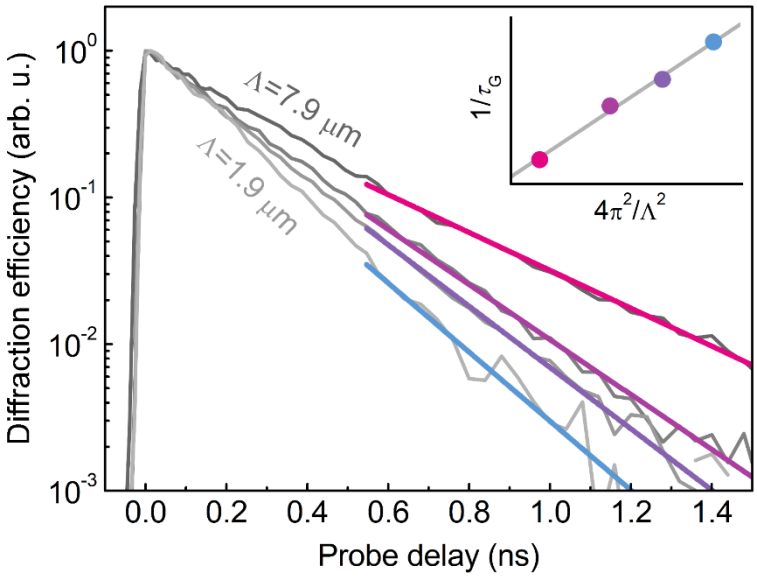

Figure 5. Normalized LITG transients recorded at different diffraction grating periods, Λ (indicated), for $Al_{0.2}Ga_{0.8}N$ epilayer. The exponential fits are depicted by straight lines. The inset shows the inverse grating decay time, $1/\tau_G$, vs. the inverse grating period, $4\pi^2/\Lambda^2$, and the corresponding linear fit according to Eq. (6).

A simplified setup for the LITG experiment in transmission geometry is depicted in Figure 6. Nd:YAG laser (*PL2143, Ekspla*) emitting 25-ps-duration pulses at 10 Hz repetition rate was employed for the excitation of AlGaN-based samples: the 3rd harmonic (355 nm) for GaN buffers in AlGaN/GaN heterostructures, the 4th harmonic (266 nm) for AlGaN epilayers with $x \leq 0.38$, and the 5th harmonic (213 nm) for $x \geq 0.46$. Meanwhile, in the study on photomodification, all samples were photoexcited with pulses of the 5th harmonic regardless the composition. Pulses of the 4th harmonic were generated from the 2nd harmonic (532 nm) using a BBO nonlinear optical crystal (noted as *BBO1* in Figure 6) located outside the laser system, while the 5th harmonic was generated from the 2nd and 3rd harmonics using a *BBO2* crystal. Pulses of the 1st harmonic (1064 nm) were used as a probe.

In studies featuring InN compounds, Yb-based *Pharos* laser (*Light Conversion*) emitting 250-fs-duration pulses at 30 kHz repetition rate was employed. The fundamental radiation at 1030 nm wavelength was used as a pump both for a sample and the *Orpheus* optical parametric amplifier (OPA; *Light Conversion*), which provided probe pulses tuned to 2400 nm.

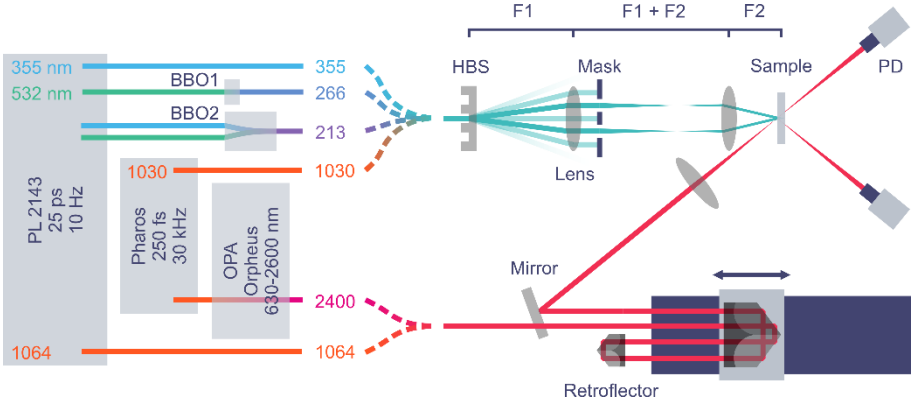

Figure 6. Simplified setup for light-induced transient grating experiments performed with different material-targeted excitation sources.

Holographic (diffractive) beam splitter (HBS) was employed to split the laser beam and to obtain two coherent pump pulses, image of which was projected on the sample surface using two lenses with *F1* and *F2* focal lengths. The angle Θ between the interfering beams was controlled by varying HBS elements with different periodic patterns. Such setup allowed to record transient gratings with the period Λ ranging from 1.4 to 15.7 μm.

Retroreflector mounted on a motorized translation stage was employed to delay a probe pulse. The second, stationary, retroreflector was exploited to double a delay time. A set of mirrors (dielectric and metallic) guided a probe beam, while a lens focused it on a recorded transient grating. Diffracted and transmitted portions of a probe beam were monitored with photodetectors (PD). The experiments were automated using a home-made software written in *labVIEW* by Dr. Tadas Malinauskas and Dr. Saulius Nargelas (Institute of Photonics and Nanotechnology, Vilnius University, Lithuania).

LITG measurements and sample photomodification for LITG characterization were performed in a wide range of excitation energy fluences spanning from 1.4 μJ/cm^2 to 1.7 mJ/cm^2. All results were obtained at room temperature. Unless stated otherwise, all values of carrier lifetime and diffusion coefficient provided in the thesis were measured using the LITG technique.

AlGaN

Chapter A: Carrier recombination in AlGaN

In this chapter, I discuss radiative and nonradiative recombination processes in $Al_xGa_{1-x}N$ epilayers with Al content x spanning from 0 to 0.7; a significant portion of these results is featured in Paper A. The study is motivated by lack of basic research on radiative recombination processes and uncertainty in recombination parameters, such as radiative coefficient B, for AlGaN alloys. To date, studies on AlGaN often borrow coefficient B from papers on GaN and regard B as composition-independent;[32,107–109] estimate B for a single sample and select composition;[110] extract sample-specific B for low temperatures only;[111] evaluate density-bound radiative lifetime instead of coefficient B – often without a density disclosure;[112–115] or predict B for the entire AlGaN composition range,[116] albeit with high discrepancy between the predicted and experimental B values for a reference GaN compound.[117–119] Meanwhile, study in this thesis addresses radiative processes as well as a split between the radiative and nonradiative B terms in a wide excess carrier density and material composition range. The study follows evolution of radiative and nonradiative pathways using density dependence of quantum efficiency as a main tool: such approach is rather common in studies on InGaN alloys, but novel for AlGaN. The most unique feature of the study is merging of LITG and quasi-stationary PL techniques, thus improving the understanding and reliability of data.

Evaluation of recombination coefficients

LITG transients for AlGaN epilayers with different Al content feature different number of exponential components and different carrier recombination channels. Here, a composition-specific algorithm for extraction of carrier recombination rates is described. This approach is tailored for the studied AlGaN samples and is used in Chapters A-C.

Figure 7a shows the LITG transients recorded in $Al_{0.65}Ga_{0.35}N$ epilayer at various peak photoexcited carrier densities (ΔN) controlled by excitation intensity. These transients are typical for all samples with moderate-to-high Al content ($x \geq 0.32$), i.e., transients are non-exponential, and consist of at least two components with different decay rates. The two components selected for the analysis are characterized by time constants τ_1 and τ_2 (indicated in Figure 7a), which represent the recombination processes at different photoexcited carrier densities. The initial component (τ_1) dominates when carrier density is the highest. At this decay stage, the density-dependent recombination of free or weakly localized electron-hole pairs should prevail. As the decay proceeds and the carrier density decreases, the second

component (τ_2) follows; it is assigned to predominantly linear localized carrier recombination via deep defect states (a.k.a. SRH channel). Next, a sample-specific set of two SRH recombination coefficients, $A_1 = 1/\tau_{SRH1}$ and $A_2 = 1/\tau_{SRH2}$, and one bimolecular (nonlinear) recombination coefficient, B, is estimated [for samples with moderate-to-high Al content].

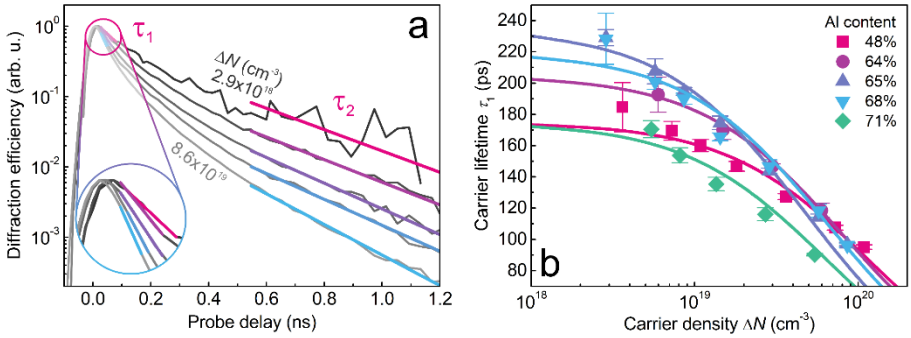

Figure 7. (a) Normalized LITG transients recorded at various peak carrier densities ΔN in $Al_{0.65}Ga_{35}N$; the exponential fits for the fast initial decay (τ_1; see the magnified area within the first 100 ps) and the slow following decay (τ_2) are depicted by straight lines. **(b)** Decay time τ_1 (symbols) in different samples with high Al content as a function of peak photoexcited carrier density; lines denote $1/\tau_1 = A_1 + BN$ fits. *Adapted from Paper A.*

The coefficients A_1 and B are extracted from τ_1 dependence on the peak photoexcited carrier density using the expression $1/\tau_1 = A_1 + BN$, as shown in Figure 7b. A good fit to the experimental data suggests a negligible role of the Auger process at carrier densities below ~10^{20} cm^{-3}. Meanwhile, the decay rate $1/\tau_2$ is simply assigned to a recombination coefficient $A_2 = 1/\tau_{SRH2}$.

AlGaN samples with low Al content ($x < 0.32$) as well as a reference GaN epilayer feature mono-exponential LITG transients in low-ΔN range (see Figure 5 in *Light-induced transient gratings* section for transients recorded in $Al_{0.2}Ga_{0.8}N$ epilayer) and nonlinear transients in high-ΔN range. In low-density case, transients are described by a single sample-specific $\tau_2 = \tau_{SRH2}$ decay time governed by SRH channel. In high-ΔN case, carrier recombination is described using coefficients $A_2 = 1/\tau_{SRH2}$ and B, evaluated from rate Eq. (4) fits. Transient fits were calculated using a home-made software written by several former and current members of Semiconductor Optoelectronics Group in the Institute of Photonics and Nanotechnology, Vilnius University.

Recombination trends

Figure 8 depicts the extracted recombination parameters B and moderate-ΔN τ_{SRH2} as functions of the Al content in the AlGaN epilayers. The

corresponding parameters obtained in thin c-plane GaN/sapphire epilayer are also shown. An overall trend for both radiative and nonradiative recombination rates is to increase with Al content x. The nonradiative lifetime τ_{SRH2} decreases from 0.8 to 0.4 ns as x increases from 0 to 0.7. These τ_{SRH2} values are rather high compared to previously reported carrier lifetimes in AlGaN layers,[115,120,121] indicating high quality of the samples. Two regions can be identified in τ_{SRH2} dependence on x (see Figure 8): a rapid decrease with increasing x in low Al content range ($x < 0.3$) and a saturation in high x range. These trends are attributed to recombination of free and localized carriers, respectively, identified based on the ratio of room kT and corresponding carrier localization depth σ. In Al-poor AlGaN alloys, σ values are smaller than the RT thermal energy of ~26 meV (see Box A), pointing to absent/shallow carrier localization and unhindered carrier mobility. In this case, carriers can reach killer centers with ease, thus enabling decrease in carrier lifetime with increasing Al content and concentration of recombination centers. In Al-rich AlGaN alloys, σ values exceed room kT, indicating deep carrier localization and limited mobility. As a result, carriers struggle to reach remote defects, and carrier lifetime does not respond to changing defect concentration.

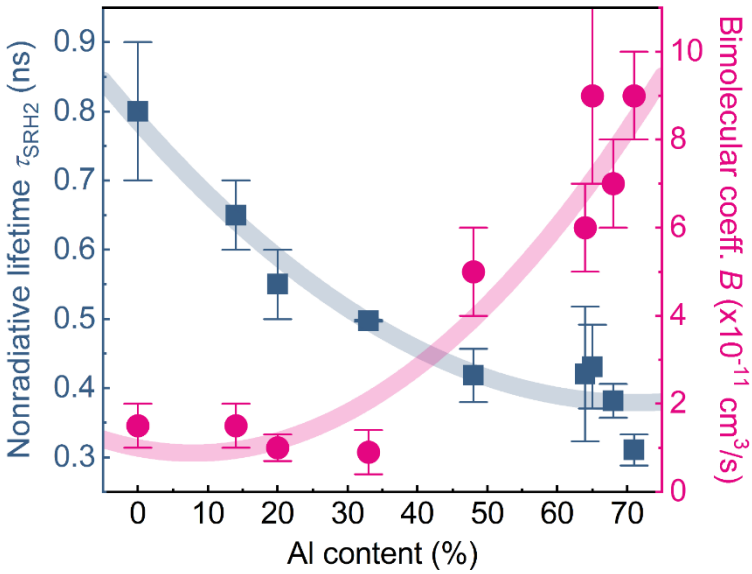

Figure 8. Nonradiative recombination time τ_{SRH2} at $\Delta N \approx 1\times10^{19}$ cm^{-3} (blue squares) and bimolecular recombination coefficient B (pink circles) as a function of Al content in AlGaN epilayers. Corresponding values in GaN epilayer are also included for comparison. Lines denote a guide for the eye. *Adapted from Paper A.*

Box A. Carrier localization in AlGaN alloys

In AlGaN alloys, composition fluctuations of purely random nature or caused by clustering and phase separation (i.e., large-scale inhomogeneities) result in potential fluctuations capable of spatial carrier localization. The strength of such localization (gauged by the parameter σ, plotted in Figure A for the studied samples) depends on the net alloy composition and is described by the expression:[101]

$$\sigma = \gamma \frac{dE_g(x)}{dx} \sqrt{x(1-x)\frac{V_c(x)}{a_{ex}^3(x)4\pi/3}} \quad \text{(A)}$$

where γ is a factor smaller than one, accounting for the quantum-mechanical averaging of the excitonic wave function, with suggested value of 0.41;[122] V_c is the smallest volume in which a composition change occurs; and a_{ex} is the exciton Bohr radius.

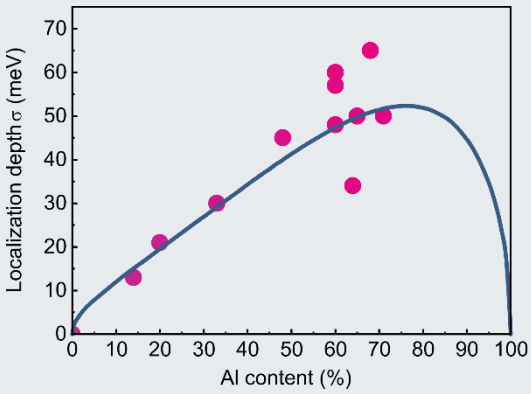

Figure A. Carrier localization depth σ vs. the Al content in the studied AlGaN epilayers. Line denotes a fit according to Eq. (A).

When V_c is the volume of the primitive unit cell, V_0, Eq. (A) provides the ultimate lower limit for σ in a perfectly random alloy. For samples in this study, model (A) fits data the best with V_c value equal to $6V_0$ (see line in Figure A). This result suggests that the composition segregation in the studied AlGaN layers occurs on a larger spatial scale, and that the potential fluctuations are not solely random in nature. An additional source of such fluctuations can be attributed to alloy clustering, phase separation, or presence of crystallographic defects.

While the carrier lifetime drops by a factor of ~2, nonlinear recombination coefficient B increases 9-fold (from 1×10^{-11} to 9×10^{-11} cm^3/s) with the increasing Al content (see Figure 8). Coefficient B typically describes radiative bimolecular recombination of the electron-hole pairs. However, it has been argued that nonradiative recombination processes can also depend on carrier density and affect B value.[111] Therefore, the coefficient B is considered as a mixture of radiative and nonradiative inputs: $B = B_{rad} + B_{nr}$. As it will be discussed further, nonradiative component becomes important at carrier densities exceeding ~10^{19} cm^{-3}. At lower ΔN, radiative B term dominates and can be used to evaluate quantum efficiency. Since $B(x)$ increase is larger compared to $\tau_{SRH2}(x)$ decrease, the equation

$$IQE = \frac{BN}{A+BN+CN^2} \quad (7)$$

predicts an increase in IQE with the Al content. High radiative performance in Al-rich AlGaN and AlN compounds has been predicted before. This projection was based on the observation of short radiative lifetimes.[107] However, increase in IQE with *x* has not been previously detected, since short radiative lifetime in reported low-quality samples has been overshadowed by even shorter nonradiative decay time.

In this work, increase in IQE with the Al content is observed using both the PL and the LITG techniques and is demonstrated in Figure 9. The PL IQE values were calculated as the ratio of the PL intensities at 300 K and 8 K assuming that IQE is equal to 100% at low temperatures (*T*). The LITG IQE values were calculated from Eq. (7) using the LITG-extracted A_{SRH2} and *B* coefficients and omitting the negligible Auger term CN^2. Both IQE dependences are shown for the same excess carrier density, $\Delta N \approx 3\times10^{18}$ cm^{-3}. At this carrier density, the radiative term of the *B* coefficient is regarded as dominant ($B \approx B_{rad}$). The small discrepancy between the PL and the LITG IQE values may be a result of the inaccurate low-*T* PL IQE assumption.[123] Despite that, the agreement between the LITG and PL IQE trends is rather good in the entire sample range.

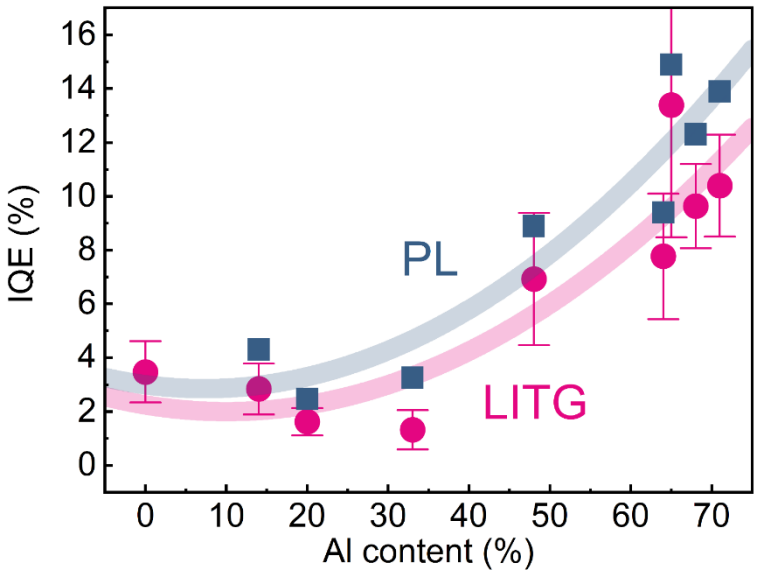

Figure 9. Internal quantum efficiency at $\Delta N \approx 3\times10^{18}$ cm^{-3} as a function of the Al content in AlGaN layers. IQE values were obtained from PL (blue squares) and LITG (pink circles) experiments. Lines denote a guide for the eye. *Adapted from Paper A.*

At higher carrier densities, LITG IQE values emerge over PL IQE; as ΔN increases, the discrepancy widens further (see PL- and LITG-measured IQE(N) dependences (points) for the $Al_{0.48}Ga_{0.52}N$ epilayer in Figure 10). The PL dependence (squares) features a saturation and eventual decrease in IQE as carrier density exceeds 10^{19} cm^{-3}. Meanwhile, the continuously increasing LITG IQE values (circles) forecast 100% peak at sufficiently high ΔN, despite the slight A_{SRH2} increase with ΔN (visible in Figure 7a). A droop-less nature of the LITG IQE(N) trend is emphasized further by a close match between the LITG-measured IQE values (circles in Figure 10) and a conventional droop-less IQE(N) curve (line in Figure 10) calculated using Eq. (7) with density-independent A and B coefficients and omitted C. Here, the coefficient A stands for the average $1/\tau_{SRH2}(N)$ rate, while B value is the same as that in Figure 8.

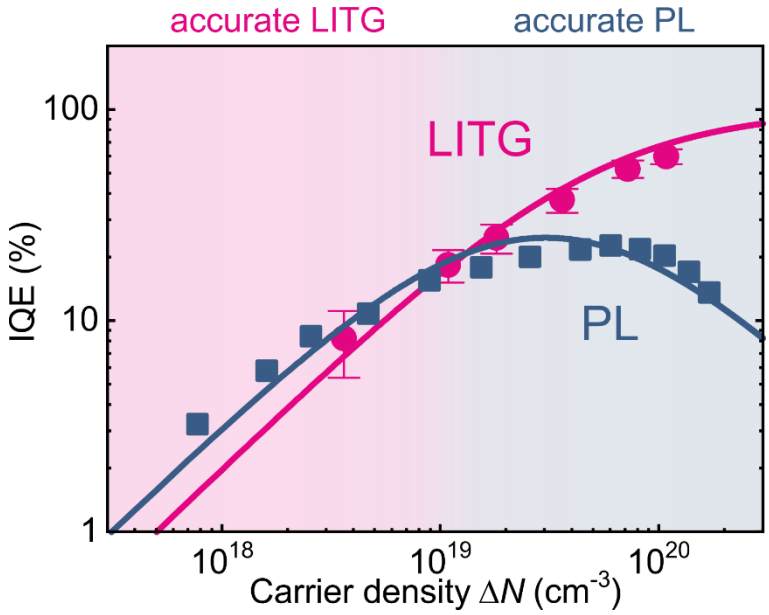

Figure 10. IQE values assessed from the PL (blue squares) and LITG (pink circles) measurements as a function of the photoexcited carrier density in $Al_{0.48}Ga_{0.52}N$. Pink and blue lines were calculated using (7) and (8) models, respectively, under the assumption that B coefficient is density-independent and solely radiative ($B = B_{rad} = const$; pink) or consists of density-dependent radiative and nonradiative terms ($B = B_{rad}(N) + B_{nr}(N) = const$; blue). *Adapted from Paper A.*

The discrepancy between the LITG and PL IQE values in high-ΔN range calls into question reliability of IQE estimation using these approaches. PL technique, although difficult to calibrate quantitatively (see the previously described *100% IQE at low T* problem), offers a direct observation of a

luminescence droop. Thus, the PL IQE curve at high ΔN should resemble the ground-truth, at least qualitatively. Meanwhile, LITG technique, although accurate in conventional cases, provides only indirect IQE estimation and does not discriminate between the radiative and nonradiative recombination pathways described with the same power function. It can be speculated that LITG-obtained B coefficient does not describe a sole radiative channel and consists of the radiative, B_{rad}, and the nonradiative, B_{nr}, terms, one of which (B_{rad}) is overestimated, while the other (B_{nr}) – underestimated at high ΔN. In such case, combination of these coefficients could be expressed as $B_{rad}(N) + B_{nr}(N) = B = const$, where B_{rad} and B_{nr} depend on ΔN, while B remains density-independent (based on the invariability of LITG-estimated B values in the entire ΔN range; see section *Evaluation of recombination coefficients*).

If these assumptions are correct, PL IQE droop could be successfully characterized using LITG-extracted set of recombination coefficients, expanded with B_{rad} and B_{nr} terms. Such characterization can be performed with the modified IQE expression:

$$IQE = \frac{B_{\mathrm{rad}}(N)N}{A+[B_{\mathrm{rad}}(N)+B_{\mathrm{nr}}(N)]N} \quad (8)$$

Here, the dependence $B_{rad}(N)$ is described as $B_{rad}(N) = B_{rad0}/(1 + N/N^*)$,[124,125] where B_{rad0} is the low-density radiative recombination coefficient (values from Figure 8), and N^* is the fitting parameter indicating the material-specific density threshold for $B_{rad} = 0.5B_{rad0}$ condition (and in this particular case – for $B_{nr} > B_{rad}$). The $B_{rad}(N)$ expression is suggested in Refs.[124,125] reporting a decrease in B_{rad} with increasing ΔN in InGaAs and InGaN alloys due to a phase-space filling phenomenon, i.e., a switch from bimolecular to monomolecular radiative recombination induced by carrier degeneracy at threshold N^*.[e] The IQE droop curve based on equation (8) with the variable parameter $N^* = 3\times10^{19}$ cm^{-3} fits well the PL IQE data for the $Al_{0.48}Ga_{0.52}N$ epilayer (see blue line and squares in Figure 10). The fits for other samples are similarly accurate and yield characteristic carrier densities N^* exceeding 10^{19} cm^{-3}. There is one caveat though – these fits require inflation of the original LITG-estimated lifetimes τ_{SRH2} (roughly by 50%) to account for the possibly exaggerated low-temperature PL IQE; such exaggeration mainly distorts low-ΔN PL IQE data. Based on the PL inaccuracy in a low carrier

[e] N^* parameter describes recombination of electron-hole pairs, thus N^* may differ from actual degeneracy threshold describing population of isolated carrier type.

density wing and the extracted N^* values indicating the range for conventional B interpretation ($B \approx B_{rad}$ at $\Delta N < 10^{19}$ cm^{-3}), one can conclude that the LITG-based IQE estimation is favorable in a low-ΔN range, while PL-based approach – in a high-ΔN range. The recommended technique for different density domains is loosely denoted in Figure 10.

The material-specific values of the extracted characteristic carrier density N^* and nonradiative term B_{nr} are demonstrated in Figure 11a and b, respectively. Here, N^* and B_{nr} correlations with the Al content x are evident: N^* decreases with the increasing x, while B_{nr} increases. These trends may be attributed to a phenomenon of *Reduced effective volume.*[126] In this case, carrier recombination properties are defined exclusively by localized carriers contained in pockets smaller than the active region (thus – *reduced volume*). In such pockets, micro-scale carrier density is higher than in the surroundings and depends on the localization depth (the stronger is the carrier localization, the higher is the carrier density in the localized sites[126]), which increases with the Al content (up to a certain point; see Box A). Meanwhile, the average, macro-scale, carrier density remains virtually the same with changing localization conditions. Therefore, the increase in the Al content/localization depth pushes the onset of the density-activated B_{rad} decrease towards the smaller N^* values (on the macro-scale) and leaves a bigger portion of excess carriers unconsumed by the radiative channel to feed the density-dependent B_{nr}-branded channel, thus effectively increasing B_{nr} values.

Although equation (8) with B_{rad} and B_{nr} terms describes the efficiency droop rather well, on some extent the term $B_{nr}N$ is just a mathematical formalism, not resembling any conventional recombination mechanism. This term can also be replaced with different power function, such as Auger-like term, C^*N^2. In this case, the extracted C^* values increase in the range $10^{-33} \div 10^{-31}$ cm^6/s with the Al content x (as well as the band-gap) and mirror the $B_{nr}(x)$ trend. Clearly, these C^* values have little in common with the actual Auger mechanism and genuine Auger coefficient, which should decrease with an increasing semiconductor band-gap.[127] Therefore, a definitive description of density-dependent nonradiative channel in AlGaN alloys cannot be given. One can agree though that such loosely defined carrier loss mechanism is dominant at high carrier densities, especially in Al-rich AlGaN. Nevertheless, empirical $B_{nr}(N, x)$ (or $C^*(x)$) trend is still useful for ballpark estimation of carrier recombination properties and is exploited in Chapter B to study the athermal defect annealing.

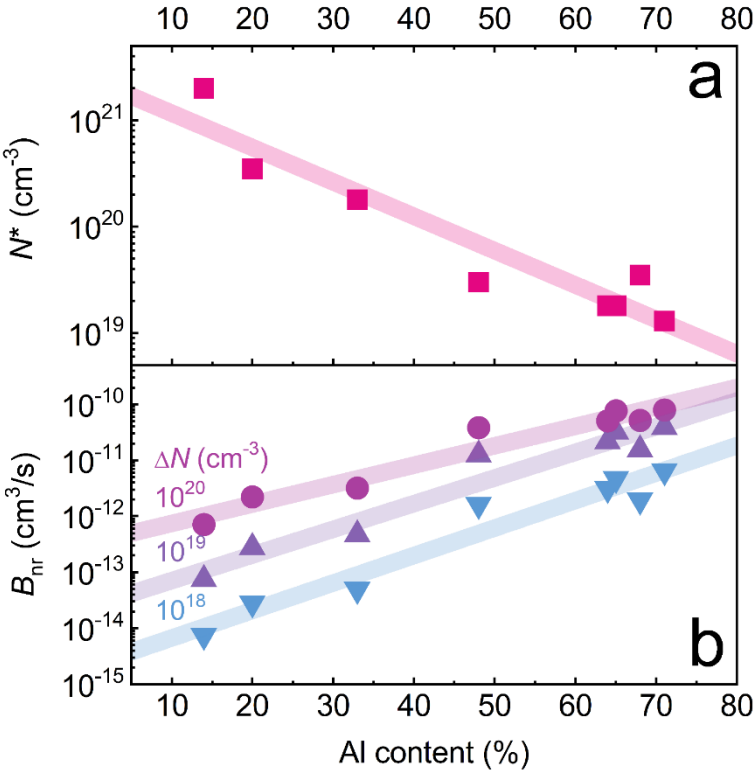

Figure 11. Characteristic carrier density N^* **(a)** and nonradiative term B_{nr} **(b)** as a function of Al content x in AlGaN epilayers; $B_{nr}(x)$ dependences were calculated for different excess carrier densities ΔN. Lines denote a guide for the eye. *Unpublished*.

Highlights

- Density-dependent radiative and nonradiative recombination pathways have been analyzed in the $Al_xGa_{1-x}N$ epilayers with x reaching 0.7
- At low carrier densities, recombination is governed by the Shockley-Read-Hall and the conventional radiative bimolecular channels
- At low carrier densities, internal quantum efficiency increases with the Al content due to the increasing radiative recombination coefficient
- At high carrier densities, efficiency is diminished due to the *phase-space filling* effect and the density-dependent nonradiative channel of unknown origin

- The density-onset of the efficiency droop decreases with the increasing Al content and the localization depth; tentatively, the trend is linked to the elevated carrier density in the localized sites

Key finding A

- At the excess carrier densities below ~10^{19} cm^{-3}, internal quantum efficiency in the AlGaN alloys increases with the carrier density and the Al content due to the increasing radiative recombination rate; in the opposite wing of carrier densities, efficiency droop occurs and is governed by the density-activated nonradiative channel as well as the phase-space filling-induced saturation of the radiative recombination rate

Research opportunities

- Dissection of recombination mechanisms in AlGaN alloys with Al content exceeding 70%
- Simulation of the density-activated nonradiative pathway and the efficiency droop

Chapter B: Photomodification of AlGaN

Recombination-enhanced defect reactions

The study in this chapter is inspired by a paper in Ref.[128] There, Saxena et al. observed curious 'optical damage' in AlGaN alloys. This 'damage' was induced by short laser pulses at energies above a certain threshold but below the melting point. Such pulses caused a permanent quench in PL intensity and a permanent decrease in carrier lifetime. The authors explained this effect using an old concept of *recombination-enhanced defect reactions* (REDR; see reviews[129–131] for an extended take on this phenomenon) and called such procedure *photomodification*. Broadly defined, the REDR mechanism is an atom migration and a defect transformation (such as diffusion, dissociation, generation, or annihilation) triggered by vibrational energy released via nonradiative recombination of excess carriers (generated optically, electrically, or using an e-beam). In the case of Saxena et al. study, carrier density-activated REDR process increased concentration of killer centers, thus accelerating carrier recombination and deteriorating PL properties.

The REDR effect is a continuously forgotten and retraced concept reported for seven decades in a wide array of materials, such as Si, GaAs, GaP,[130] ZnSe,[132] SiC,[133] ZnO,[134] diamond,[135] and even photosynthetic bacteria.[136] In the 50's, first reported cases of REDR were described using a term *thermal spike*.[137] This term is still exploited to characterize a specific REDR case, which assumes that an energy liberated by nonradiative recombination is equipartitioned over all phonon modes contained in the local environment of a killer center.[131] Basically, thermal spike is a confined annealing driven by excess carrier recombination. In the 60's, another REDR concept emerged – *phonon kick*.[138] This case assumes that the REDR is driven by a selective flow of the recombination-liberated energy along a specific reaction coordinate of phonons.[131] Since this energy (on the order of band-gap) is directly channeled to a select atom instead of all over the whole lattice, phonon kick can enable reactions unachievable with conventional annealing. In the 70's, the invention of the deep-level transient spectroscopy significantly boosted REDR research and fostered a fairly comprehensive theory by Weeks et al.,[139] which was expanded upon by Sumi et al. in the 80's.[140] Later, REDR theory has been occasionally reexamined,[141–144] often abandoned, and rediscovered with the emergence of new materials and corresponding device reliability studies.

In nitrides, studies on recombination-enhanced effects mainly focus either on *recombination-enhanced dislocation glide* phenomenon[145–148] or on REDR

aftereffects in laser lift-off,[149,150] dopant activation,[151] as well as device break-in and aging procedures.[132,152,153] Nevertheless, few studies have attempted to dissect REDR on a more granular level and to tackle core REDR features.[128,154] For instance, Saxena et al.[128] eliminated lattice heating (basically – thermal spike case) as a cause of laser-induced deterioration of PL properties in AlGaN (see above); while Tsujio et al.[154] predicted that Ga vacancy can behave as a killer center and can trigger defect reactions (specifically – hop of N atom) via phonon kick in III-nitrides.

In this thesis, I study the photomodification of AlGaN epilayers and discuss photomodification impact on carrier dynamics looking through a lens of REDR phenomenon. Since REDR mechanism is rather unexplored in nitrides, this study holds a handful of negative results and is more qualitative than quantitative compared to studies in other chapters. Nevertheless, few significant goals are still achieved: previously unknown factor determining AlGaN susceptibility to the photomodification is found and photomodification-induced changes to carrier diffusivity are evaluated. Majority of these results are featured in Paper B.

The procedure and the aftermath

AlGaN epilayers were photomodified at room temperature using high intensity pulses of 10 Hz repetition rate and 213 nm wavelength short-enough for interband carrier absorption. For LITG characterization, samples were photomodified with laser pulses of 25 ps width, for PL – with pulses of 4 ns width; pulse width options were imposed by capabilities of available experimental base. Photomodification duration was gauged by the number of photomodification pulses; pulse-generated excess carrier density (from here on – photomodification carrier density, N_{mod}) was controlled by excitation intensity. Photomodification impact on carrier dynamics was evaluated from LITG and PL measurements performed at 'safe' carrier densities below the photomodification threshold ($N_{LITG} = 3\times10^{19}$ cm^{-3} – for LITG characterization, $N_{PL} = 4\times10^{18}$ cm^{-3} – for PL); excitation pulse wavelength was set to 213 nm. Optical micrographs taken before and after the photomodification verified the absence of photomodification-induced optical mirror damage. Meanwhile, comparison of photomodification-altered PL intensity and LITG IQE indicated no change in light extraction.

Photomodification carrier density dependences of normalized diffraction efficiency, η, and carrier lifetime, τ_{SRH1}, are demonstrated in Figure 12: both η and τ_{SRH1} parameters permanently decreased with increasing N_{mod}. Here, photomodification was performed in the most susceptible epilayer –

$Al_{0.71}Ga_{0.29}N$ (see below for susceptibility causes); each data point corresponds to a photomodification with 1600 pulses in a different, previously unmodified sample spot; η was measured at a peak of LITG transient. Carrier density N_{mod} pointing to a 5% decrease in η is regarded as the photomodification threshold. For $Al_{0.71}Ga_{0.29}N$ sample, this threshold is $N_{mod} \approx 6\times10^{19}$ cm^{-3}; for other epilayers – it is higher.[f] Photomodification mechanism is strongly bound to carrier density and could not be activated by a prolonged exposure to densities lower than the threshold, e.g., exposition of $Al_{0.71}Ga_{0.29}N$ to density $N_{mod} \approx 4\times10^{19}$ cm^{-3} (slightly below the threshold) had no observable impact on η even after tens of thousands of laser shots. Diffraction efficiency η responded to change in photomodification duration only at densities above the threshold. Photomodification impact was stronger at higher densities and shorter exposure than vice versa. For instance, photomodification at densities as high as $N_{mod} \approx 2\times10^{20}$ cm^{-3} for ~1600 pulses diminished η by ~40%, while photomodification at $N_{mod} \approx 6\times10^{19}$ cm^{-3} for ~5400 pulses – by ~7%, although the product of density and duration is the same in both cases.

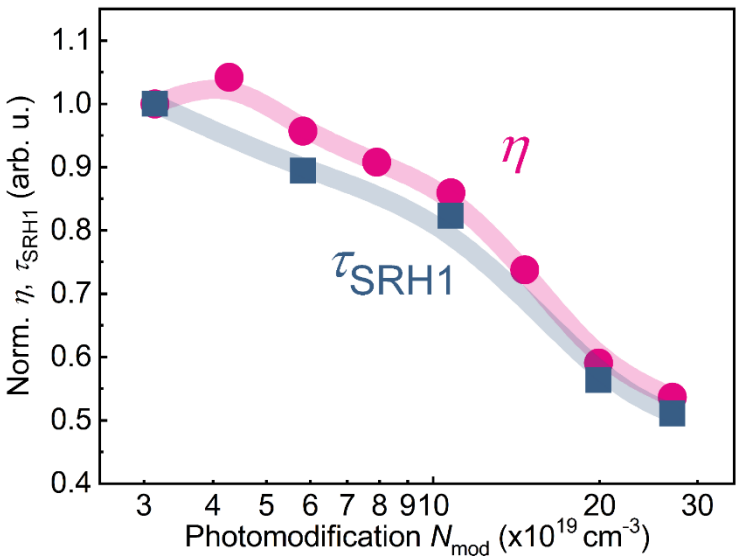

Figure 12. Normalized diffraction efficiency η and nonradiative carrier lifetime τ_{SRH1} as a function of photomodification carrier density N_{mod} in $Al_{0.71}Ga_{0.29}N$ epilayer photomodified with 1600 laser pulses. *Adapted from Paper B.*

[f] Although photomodification thresholds were approached carefully in Chapter A study, in some cases they were slightly exceeded; this overshoot affects only few extreme data points and has no impact on final conclusions.

Meanwhile, N_{mod} dependence of nonradiative carrier lifetime τ_{SRH1} mirrored the diffraction efficiency curve (see Figure 12), and densities as high as $N_{mod} \approx 3\times10^{20}$ cm^{-3} diminished τ_{SRH1} by ~50%, similarly to η case. The correlation between $\tau_{SRH1}(N_{mod})$ and $\eta(N_{mod})$ trends indicates that changes in photomodified recombination properties are well reflected in easy-to-measure instantaneous η; this feature will be exploited in further analysis.

Lifetime τ_{SRH1} characterizes free or weakly localized carriers, while lifetime τ_{SRH2} covers the localized ones (only in epilayers with σ exceeding room kT; see Chapter A). Although the photomodification cut τ_{SRH1} by a half, the procedure hardly affected τ_{SRH2}: merely ~10% decrease in τ_{SRH2} was observed in the photomodified $Al_{0.71}Ga_{0.29}N$ sample. This trend is in line with the REDR mechanism, i.e. photomodification-activated REDR process generates additional nonradiative defects, which are easier to reach by free instead of localized carriers.

Nonlinear recombination coefficient B was evaluated after the photomodification as well: no changes were detected. Since nonlinear recombination pathways in AlGaN are governed by localization phenomenon (see Chapter A), B indifference to the photomodification suggests no photomodification-induced changes in carrier localization. This prediction was tested, and indeed no changes in localization depth σ were detected by PL measurements.

Different samples endured photomodification-induced acceleration of SRH term differently. Therefore, sample settings contributing and non-contributing to photomodification-induced material response were investigated. Further conclusions were drawn from dependences of diffraction efficiency on photomodification duration in AlGaN epilayers of various composition (see Figure 13). In the following discussion, samples were photomodified at identical photomodification carrier density equal to $N_{mod} = 2\times10^{20}$ cm^{-3}. Photomodification duration [instead of density N_{mod}] was chosen as an argument of η dependences to streamline the experiment, i.e., change in the exposure duration did not require change of the sample spot.

Photomodification is not driven by a lattice heating and carrier thermalization. Photomodification of samples $Al_{0.19}Ga_{0.81}N$ and $Al_{0.71}Ga_{0.29}N$ using 5.8 eV photons generated excess carriers with thermalization energy on the order of 2.1 eV and of 0.7 eV, respectively. However, higher excess energy did not coincide with a stronger photomodification impact: the sample corresponding to a higher excess energy displayed no change in η, while the sample matching lower excess energy demonstrated a steep decrease in η (see pink squares and green triangles in Figure 13, respectively).

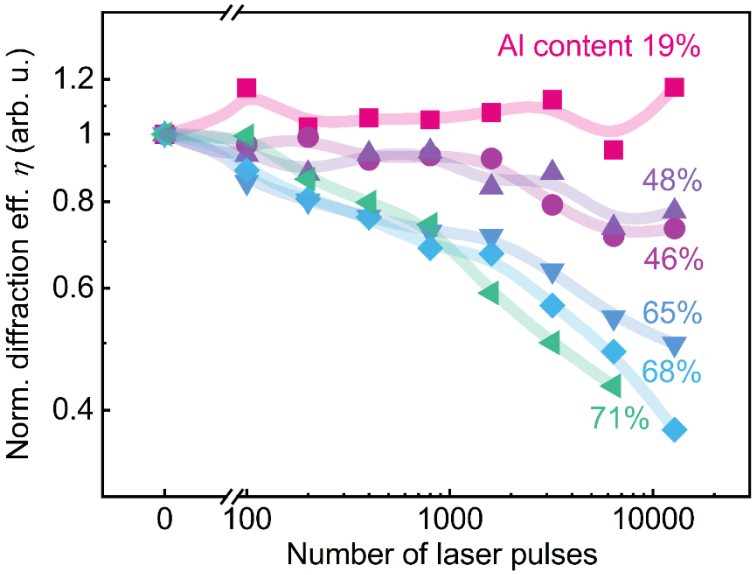

Figure 13. Normalized diffraction efficiency η as a function of photomodification duration in various composition AlGaN epilayers photomodified at $N_{mod} \approx 2\times10^{20}$ cm^{-3}; $\eta > 1$ values are due to experimental uncertainty. *Adapted from Paper B.*

Photomodification impact does not depend on virgin SRH recombination rate. As seen in Figure 13 (purple circles and violet triangles), η decreased at a similar rate in samples with similar Al content ($Al_{0.46}Ga_{0.54}N$ and $Al_{0.48}Ga_{0.52}N$) despite of different [unmodified] τ_{SRH} lifetimes ($\tau_{SRH1}^{Al_{0.48}Ga_{0.52}N}/\tau_{SRH1}^{Al_{0.46}Ga_{0.54}N} \approx 1.6$; $\tau_{SRH2}^{Al_{0.48}Ga_{0.52}N}/\tau_{SRH2}^{Al_{0.46}Ga_{0.54}N} \approx 2$). Nevertheless, this outcome should not occur in an REDR-driven system, since shorter τ_{SRH} lifetimes should result in a higher number of nonradiatively recombining carriers and defect reactions, thus enhancing photomodification impact in samples of lower quality. This contradiction can be resolved if other, faster, nonradiative pathway dominates carrier recombination in place of SRH channel (see next point).

Photomodification impact is governed by [B_{nr}-branded] nonlinear nonradiative pathway / Al content / localization depth. At carrier densities above 10^{20} cm^{-3} (such as $N_{mod} = 2\times10^{20}$ cm^{-3}), fast B_{nr}-branded pathway indeed dominates all recombination channels in [Al-rich] AlGaN epilayers (see Figure 11 in Chapter A). Furthermore, B_{nr} term is bound to AlGaN composition (and localization depth) and is similar in epilayers with similar Al content. Therefore, samples $Al_{0.46}Ga_{0.54}N$ and $Al_{0.48}Ga_{0.52}N$ respond to photomodification similarly despite different τ_{SRH} lifetimes (see Figure 13).

Since B_{nr} increases with the Al content, higher susceptibility to photomodification for Al-rich AlGaN is expected; this expectation is confirmed in Figure 13.

Al-bound photomodification impact may be explained by other phenomena as well, although they are rather unlikely and tentative. One of these explanations may be based on high Al propensity towards oxidation[155–157] occurring during the alloy growth.[158–161] In this case, concentration of REDR-generated defects is bound to concentration of oxygen (O) trapped in AlGaN lattice. Thus, higher O contamination typical for Al-rich AlGaN results in higher concentration of REDR-activated O-based defects and higher photomodification impact.

Another plausible mechanism may be driven by higher defect 'potency' in Al-rich AlGaN instead of higher defect concentration. In this case, REDR generates defects, such as nitrogen vacancies (V_N), energy level of which shifts deeper into the bandgap with increasing Al content.[155,162] Following this shift, SRH recombination via these defects accelerates (creating the illusion of higher photomodification impact), although concentration of REDR-generated defects remains the same between the samples.

To reiterate, photomodification affects SRH rate the stronger, the longer is the photomodification duration or the higher is the carrier density N_{mod} and the Al content. Meanwhile, Al content x governs the magnitude of the B_{nr} term and plausibly the energy level of REDR-generated defects or the alloy oxidation degree. Causative link between the photomodification impact and the B_{nr} term is more probable though, since $B_{nr}(N_{mod}, x)$ trend also complements stronger photomodification impact at higher densities N_{mod} vs. longer expositions (see above for discussion on this discrepancy). As N_{mod} increases, increase in B_{nr} follows (see Figure 11b in Chapter A), thus resulting in a larger share of nonradiatively recombining carriers and a larger increment of defect reactions. In contrast, proportional increase in the photomodification duration does not change B_{nr}, thus retaining the same balance between nonradiative and radiative processes and resulting in a smaller increment of defect reactions.

Along with the carrier recombination, the photomodification has affected the carrier diffusivity. This effect is demonstrated in Figure 14, where diffusion coefficient D and effective carrier lifetime τ are plotted as a function of the photomodification duration in the $Al_{0.48}Ga_{0.52}N$ and $Al_{0.19}Ga_{0.81}N$ epilayers. Here, $Al_{0.48}Ga_{0.52}N$ sample was photomodified at $N_{mod} = 2\times10^{20}$ cm^{-3}, while photomodification carrier density for $Al_{0.19}Ga_{0.81}N$ was increased up to $N_{mod} = 3.7\times10^{20}$ cm^{-3} to activate material response.

Exposure dependences of carrier lifetime were similar in both samples: τ continuously decreased with increasing exposure time. Exposure dependences of diffusion coefficient were different: in $Al_{0.48}Ga_{0.52}N$ epilayer, a non-monotonous trend of initial increase and eventual decrease was observed, while in $Al_{0.19}Ga_{0.81}N$, only an increase was detected. Meanwhile, diffusion length, $L = \sqrt{\tau D}$, was not affected by the photomodification in the $Al_{0.19}Ga_{0.81}N$ sample and increased with the exposure time in $Al_{0.48}Ga_{0.52}N$, peaking at 45% from the initial value (after 200 pulses).

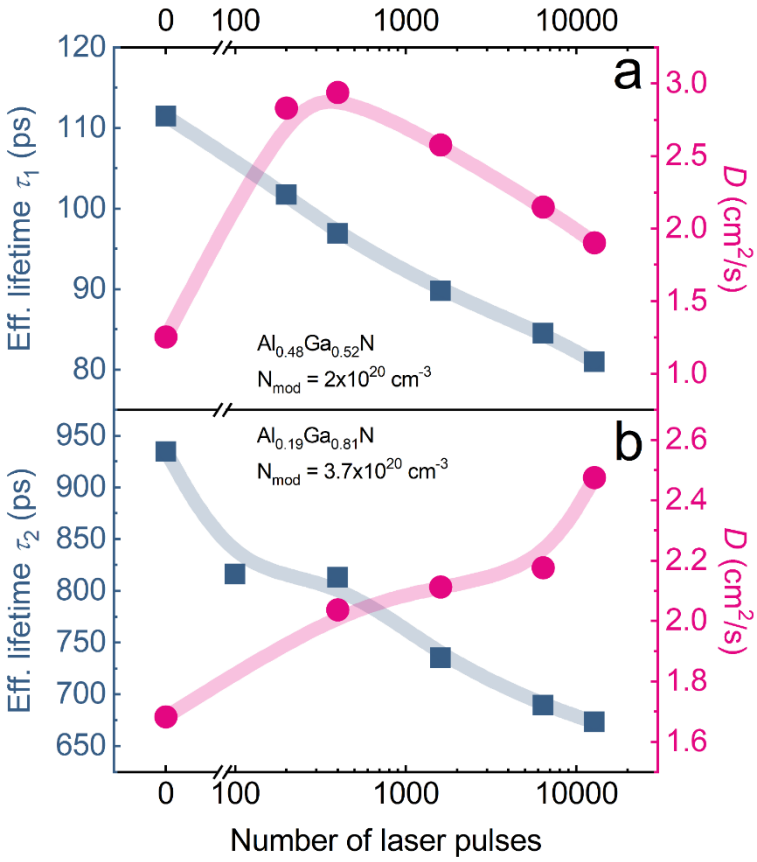

Figure 14. Effective carrier lifetime τ (blue squares) and diffusion coefficient (pink circles) as a function of photomodification duration in **(a)** $Al_{0.48}Ga_{0.52}N$ *(adapted from Paper B)* and **(b)** $Al_{0.19}Ga_{0.81}N$ *(unpublished)* epilayers photomodified at N_{mod} = 2×10²⁰ cm⁻³ and N_{mod} = 3.7×10²⁰ cm⁻³, respectively.

Such increase in carrier diffusivity was unexpected, yet the phenomenon is likely beneficial, especially for devices requiring highest possible diffusion lengths (e.g., photodiodes). The study did not aim at this phenomenon, thus sets of exposition time and N_{mod} parameters were chosen rather randomly for

both samples, and are probably suboptimal, i.e., even higher increase in D and L is plausible. At this stage, a mechanism for such increase is unclear. The naturally expected link between the photomodification-induced change in carrier diffusivity and change in carrier localization depth was confirmed false based on σ measurements, thus leaving the study to tentative explanations only. Fortunately, inspiration for this can be taken from studies on semiconductor thermal annealing[163] and device ageing,[164,165] especially at elevated carrier densities.

Increase in carrier diffusivity with increasing exposure time may be enabled by REDR-activated reordering of alloy crystalline structure, i.e., atom rearrangement and migration.[155,166–168] Such reordering may open low-scattering pathways and remove carrier scattering defects, enhancing carrier mobility. Meanwhile, decrease in carrier diffusivity manifesting in $Al_{0.48}Ga_{0.52}N$ epilayer exposed to a high number of photomodification pulses (>400; see Figure 14a) may be enabled by a competing REDR-activated process – generation of carrier scattering defects. Since slopes for high-exposure D and τ dependences are similar, carrier scattering defects may be contributing to SRH recombination as well. These defects may be attributed to nitrogen vacancies,[155,162,163,169,170] sites of out-diffused Al,[155,166,167] Al and Ga oxides,[155,171–174] and corresponding complexes.

Highlights

- $Al_xGa_{1-x}N$ epilayers with x reaching 0.7 were photomodified at extremely high excess carrier densities photogenerated with intense laser pulses
- The photomodification permanently accelerates SRH recombination via REDR-generated defects
- The deterioration of carrier lifetime is most pronounced in the Al-rich AlGaN epilayers probably due to dominating density-dependent nonradiative channel resulting in a larger number of defect reactions
- The photomodification at certain carrier densities and durations enhances carrier diffusivity

Key finding B

- The photomodification of $Al_xGa_{1-x}N$ epilayers (with $x \approx 0.2 \div 0.7$) at extremely high carrier densities ($6\times10^{19} \div 3.7\times10^{20}$ cm^{-3}) photogenerated with intense laser pulses can permanently accelerate nonradiative carrier recombination and enhance the diffusivity; the magnitude of such changes depends on the number of photomodification pulses, carrier density and the Al content

Research opportunities

- Study on duration of REDR-driven atomic-scale processes. Suggested 'tool' for such a study is a pulse of varying duration. In the current work, photomodification performed with picosecond- and nanosecond-pulses yielded similar results, thus pointing to super-nanosecond-scale atomic processes. Unfortunately, such comparison was carried out in a single sample, and evaluation of photomodification impact was not cohesive technique-wise, i.e., nanosecond-pulse photomodification was studied using the PL technique, while picosecond-pulse – using the LITG. Therefore, results are not conclusive
- Detailed description of photomodification-activated mechanism altering carrier diffusivity
- Study on REDR-generated defects in AlGaN alloys: evaluation of activation energies for defect reactions; identification of defects
- Optimization of photomodification procedure for desired effect: multidimensional mapping of photomodification conditions (such as carrier density and exposition time for a given alloy composition) and corresponding changes in carrier dynamics

AlGaN/GaN

Chapter C: Carrier dynamics in AlGaN/GaN interface

In this chapter, I use time-resolved photoluminescence spectroscopy and light-induced transient grating approaches to study carrier dynamics in AlGaN/GaN heterointerfaces, focusing on detrimental effects of interface recombination (a.k.a. surface recombination (SR) in bare-surface materials). Such studies have been rarely performed in nitride devices, mainly due to the secondary role of nonradiative SR in the high-efficiency InGaN LEDs: the SR velocity is generally lower in nitrides[175–179] compared to other III-V materials, and the diffusion length in the active InGaN region is relatively short[180] due to both carrier-localizing composition fluctuations and short carrier lifetime at high operating carrier density.[181] Additionally, the detrimental effects of SR usually decrease with the addition of a surface-passivating layer or, in case of a heterostructure, an interface layer. For instance, in bare-surface GaAs the surface recombination velocity (S) can reach 10^7 cm/s,[182] but a suitably engineered interface can reduce the S value down to single digits – 1.5 cm/s, as reported for GaInP/GaAs heterostructures.[183] Contrary to such expectations, in run-of-the-mil AlGaN/GaN heterointerfaces I observe an unconventional reverse phenomenon: AlGaN barrier-induced deterioration of the interface quality and acceleration of nonradiative recombination in the underlying GaN buffer. The results reported here are unpublished.

The study was performed in 12 AlGaN/GaN heterostructures (listed in Table 1 in *Samples* section) split into three sample sets with different barrier Al content: $\bar{x}$ = (0.13, 0.2, or 0.34), with $\lesssim$10% relative variation in x within a sample set. To simplify sample labeling, the composition of AlGaN barriers within a sample set was regarded the same.

The diffusion coefficient in GaN buffer was measured using the LITG technique, whereas the carrier lifetime in GaN buffer and the AlGaN barrier was obtained from both the TRPL and LITG transients. Different excitation configurations for the LITG and TRPL experiments are demonstrated in Figure 15; the excitation beams of different wavelength (λ = 266 nm and 355 nm) are depicted with different colors (purple and blue, respectively).

In the LITG experiment, carrier dynamics were selectively observed in the AlGaN barrier and in the GaN buffer by employing excitation pulses of 266 nm and of 355 nm wavelength, respectively (see Figure 15a and b). In the TRPL experiment, above-bandgap 266 nm excitation of both AlGaN as well as GaN layers and the availability of spectral resolution allowed the extraction of carrier lifetime in both barrier and buffer simultaneously (see Figure 15c), while 355 nm excitation provided greater absorption depth in GaN (Figure

15d). As a result, carrier recombination was investigated in different depths of the GaN buffer: in the initial ~50 nm and in the initial ~100 nm (from here on, 'shallow' and 'deep' interface, respectively).

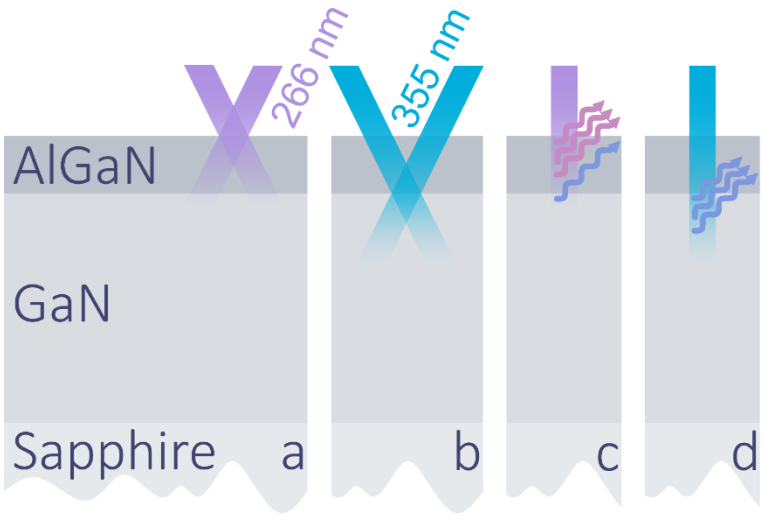

Figure 15. Simplified scheme of the excitation configurations: a) LITG in AlGaN barrier, 266 nm excitation; b) LITG in GaN buffer, 355 nm excitation; c) 266 nm excitation for TRPL in the barrier and the shallow interface (initial ~50 nm in GaN); d) 355 nm excitation for TRPL in the deep interface (initial ~100 nm in GaN).

Carrier dynamics in AlGaN barriers

Carrier lifetimes in AlGaN barriers (τ_{SRH2}^{AlGaN}; see *Evaluation of recombination coefficients* section in Chapter A for description) with various Al content are demonstrated in Figure 16 as a dependence on the V/III molar ratio, which was calculated from the gas flow rates: NH_3/(TMGa + TMAl). A non-monotonous trend of the initial increase and eventual decrease is observed for all sample sets. Different sections of this trend are shaped by different growth-related defects.

The initial growth of τ_{SRH2}^{AlGaN} with V/III ratio (NH_3 flow rate) may be attributed to the diminishing nonradiative recombination via defects bound to impurities (e.g., carbon) or native defects related to nitrogen vacancies (V_N), such as V_N-decorated dislocations. It has been shown that increase in the NH_3 flow rate can cause a decrease in the V_N concentration in GaN[184,185], AlGaN,[158,186] and AlN[187]; a similar decrease is expected for the carbon concentration in GaN[159].

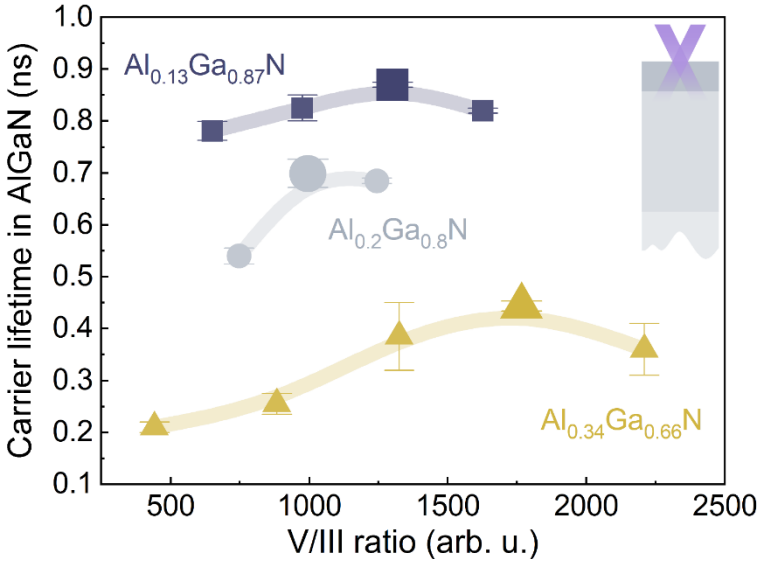

Figure 16. Carrier lifetime τ_{SRH2}^{AlGaN} in $Al_xGa_{1-x}N$ barriers with different Al content *x* as a function of V/III ratio; τ_{SRH2}^{AlGaN} was assessed from LITG transients recorded with pulses of λ = 266 nm. *Unpublished.*

At the highest V/III ratios the carrier lifetime may decrease due to the excess-nitrogen induced point defects and degraded structural quality. Overflow of N can saturate the lattice sites and hinder the surface mobility of Ga[188] and Al adatoms,[158,189] thus generating Ga[190] and Al vacancies (V_{Ga}, V_{Al}) or deteriorating surface morphology.[189,191,192] V_{Ga} and V_{Al}-related mid-gap defects may be attributed to V_{Ga}-O complexes,[193,194] dislocations decorated with V_{Ga}-O,[195–197] or V_{Al}-O complexes.[198,199]

Further discussion of the carrier lifetime τ_{SRH2}^{AlGaN} concerns the barriers with different Al content grown at respectively optimized V/III ratios (see larger symbols in Figure 16). In these barriers, peak carrier lifetime decreases from 0.9 to 0.4 ns with increasing Al content (from 0.13 to 0.34; see Figure 16). Evidently, the optimization of growth conditions did not compensate for the decrease in structural quality with growing Al content. Such quality deterioration is typically attributed to low Al adatom mobility,[200] resulting in a large and fine scale lateral phase separation,[160,201] spontaneous phase modulation,[160] as well as extended and point defects. These point defects may be native or impurity-bound. For instance, Chichibu et al. observed[115] the increasing concentration of V_{III} (or V_{III} complexes) with increasing Al content in AlGaN and argued[202] that V_{Ga} are the main carrier killers in GaN. Meanwhile, studies on impurities in AlGaN demonstrate increasing oxygen[158–161] and carbon[159] concentrations with increasing Al content as well.

While a definitive interpretation of mechanisms governing τ_{SRH2}^{AlGaN} at different growth conditions and barrier compositions is unavailable, it can be stated that the nonradiative carrier recombination in the studied barriers is driven by defects of numerous origins.

Carrier dynamics in GaN buffers

The data on carrier recombination at different AlGaN/GaN interfaces is presented in Figure 17a as effective carrier lifetime in GaN buffer (τ^{GaN}) dependences on initial photogenerated carrier density ΔN; the lifetime curves for shallow and deep interface excitations are depicted as dashed and continuous lines, respectively. Lifetime τ^{GaN} was extracted from a trailing transient component (see Figure 17b for select deep interface TRPL transients and corresponding fits) and comprises radiative as well as nonradiative terms. The rise-and-fall behavior of $\tau^{GaN}(N)$ trends can be attributed to the competition between the nonradiative and radiative terms: the initial saturation of the nonradiative channel and the eventual emergence of the radiative term with increasing ΔN. The nonradiative recombination may include contributions from Shockley-Read-Hall and interface recombination channels. The SRH channel saturation and lifetime increase with carrier density was previously observed in synthetic diamonds,[203] where defects acting as centers of nonradiative recombination were saturated at high photoexcitation levels.

The dominance of either SRH or interface recombination channel can be determined by varying the excitation wavelength.[204,205] In this study, this is achieved by measuring carrier lifetime in shallow and deep interface.

In GaN buffer with $Al_{0.13}Ga_{0.87}N$ barrier the lifetime τ^{GaN} increases by switching from deep to shallow interface (see continuous and dashed blue lines in Figure 17a). This is an indication that the defect concentration is decreasing with increasing effective layer thickness (decreasing depth), and that the interface has a minor impact on carrier recombination. A similar carrier lifetime increase with increasing layer thickness occurs in bulk GaN due to a decrease in dislocation density.[206–210] The opposite case is observed in the heterostructures with barriers richer in Al content (see gray and yellow lines for $Al_xGa_{1-x}N$/GaN heterostructures with x = 0.2 and 0.34, respectively). Here, switching from the deep to shallow interface results in a decrease in the carrier lifetime τ^{GaN}. This trend indicates the increasing role of the interface recombination channel.

The increasing Al content in the AlGaN barrier causes another few important and non-intuitive changes in the $\tau^{GaN}(N)$ curves (seen in Figure 17a).

As the barrier Al content increases from 13% to 34%, the lifetime in the GaN buffer decreases by a factor of ~2 (calculated as the average shallow interface τ^{GaN}). Furthermore, the onset of the increase in $\tau^{GaN}(N)$ shifts to higher carrier densities. Finally, the ratio between the deep and the shallow interface lifetimes τ^{GaN} increases with the barrier Al content: from ~1.2 (x = 0.2) to 1.4 (x = 0.34) at the lowest carrier densities. At first glance, the Al content in the AlGaN barrier has a direct effect on the carrier recombination in the GaN buffer.

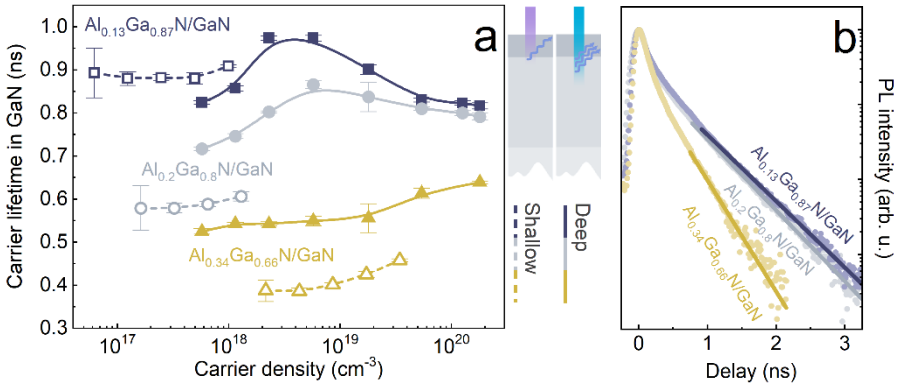

Figure 17. a) Carrier lifetime τ^{GaN} in GaN buffers with AlGaN barriers of various composition as a function of initial photoexcited carrier density; τ^{GaN} was assessed from the TRPL transients recorded at the shallow and deep interface of the AlGaN/GaN heterostructures using excitation pulses of 266 nm and 355 nm wavelength, respectively. **b)** High-excitation TRPL transients recorded at the deep interface of the heterostructures with the barriers of various composition; solid lines denote exponential fits. *Unpublished.*

To determine if the variation in lifetime τ^{GaN} between the samples is related to the barrier composition only, deep interface τ^{GaN} was additionally assessed in samples with different barrier defect origins (each sample corresponding to one point in Figure 16). The relation between τ^{GaN} and τ_{SRH2}^{AlGaN} is demonstrated in Figure 18a, where τ^{GaN} scales linearly with τ_{SRH2}^{AlGaN} for all samples. This correlation also holds for samples of similar barrier composition but different structural quality (see symbols of matching color in Figure 18a). Apparently, the carrier lifetime decrease in GaN cannot be attributed to a particular barrier defect and is controlled by the overall AlGaN barrier quality.

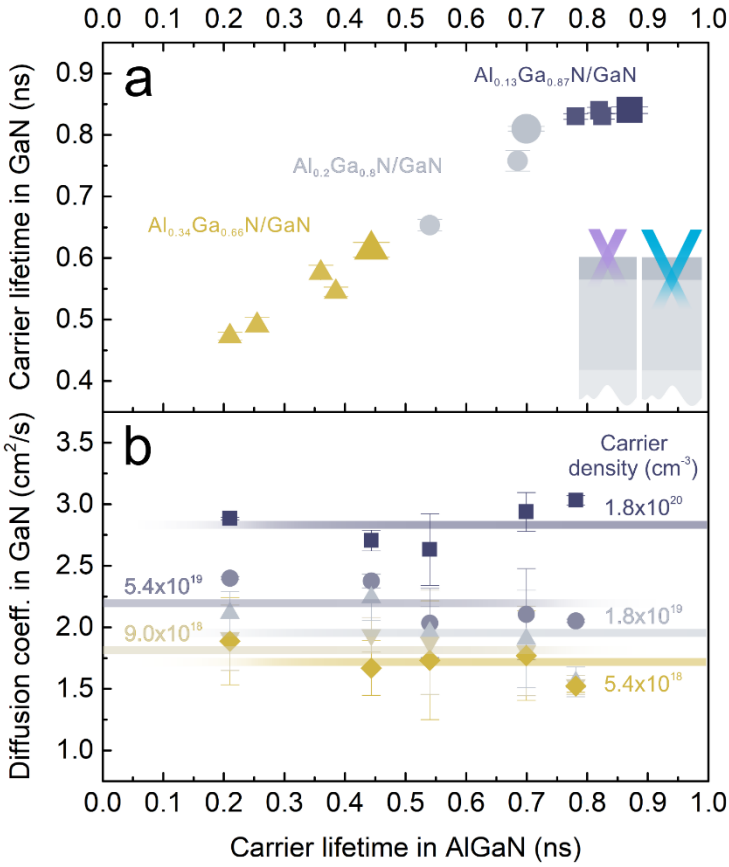

Figure 18. a) Carrier lifetime τ^{GaN} at fixed carrier density $\Delta N = 5.4\times10^{19}$ cm^{-3}; **b)** diffusion coefficient D^{GaN} at various ΔN in GaN buffers as a function of carrier lifetime τ_{SRH2}^{AlGaN} in AlGaN barriers; τ^{GaN}, D^{GaN} were assessed from the LITG transients recorded with pulses of 355 nm wavelength, while τ_{SRH2}^{AlGaN} – with pulses of 266 nm wavelength. *Unpublished*.

The effects of barrier quality on carrier scattering in GaN were assessed from the diffusion coefficient D^{GaN} measurements; the values of D^{GaN} as a function of τ_{SRH2}^{AlGaN} at various carrier densities ΔN in GaN are demonstrated in Figure 18b. No dependence of carrier diffusivity in buffer on carrier lifetime τ_{SRH2}^{AlGaN} in barrier was observed throughout the explored ΔN range (from 5.4×10^{18} to 1.8×10^{20} cm^{-3}). However, dependence of D^{GaN} on density ΔN was detected: average D^{GaN} increases from 1.7 to 2.8 cm^2/s with increasing ΔN. Similar diffusion coefficients at comparable carrier densities are reported for thick high-quality HVPE-grown GaN,[118] where increase in carrier diffusivity with ΔN was attributed to carrier degeneracy.[118] Identical diffusivity properties between the studied GaN buffers with different AlGaN barriers

indicate the absence of barrier effect on carrier scattering in GaN, contrary to the barrier influence on carrier lifetime τ^{GaN}.

The extracted D^{GaN} values are required for a more detailed analysis of diffusion-limited interface recombination pathway at the AlGaN/GaN interface. Such analysis was performed by fitting LITG transients with the following ABC model and assessing the interface recombination velocity (S_i):

$$\frac{\partial N(x,z,t)}{\partial t} = \nabla[D^{GaN}\nabla N(x,z,t)] - \frac{N(x,z,t)}{\tau_{SRH}^{GaN}} - B^{GaN}N^2(x,z,t) + G(x,z,t) \quad (9)$$

$$\left.\frac{\partial N(x,z,t)}{\partial z}\right|_{z=0} = \frac{S_i N(x,0,t)}{D^{GaN}}$$

$$\left.\frac{\partial N(x,z,t)}{\partial z}\right|_{z=d} = 0$$

where τ_{SRH}^{GaN} – SRH lifetime in GaN, B^{GaN} – radiative recombination coefficient in GaN, $G(x, z, t)$ – spatially modulated carrier generation rate in GaN, and d – the GaN buffer thickness. This model is similar to that described in section *Light-induced transient gratings* (see Eq. (4)), except for the omitted Auger term and the neglected recombination at the GaN/sapphire interface. In the model (9), the radiative recombination coefficient B^{GaN} is considered identical between the buffers. The B^{GaN} value was assessed in the sample with the highest quality barrier and equals to 1.5×10^{-11} cm^3/s, which is close to the previously reported values in thick ELO- and HVPE-grown GaN layers.[118,119]

Three LITG transients recorded at $\Delta N = 5.4\times10^{19}$ cm^{-3} in GaN buffers with various quality AlGaN barriers are depicted with fits (according to Eq. (9)) in the inset of Figure 19; the corresponding S_i and τ_{SRH}^{GaN} values are illustrated as larger colored circles in Figure 19a and b, respectively. These values (and the fitting results for all other samples and carrier densities) are shown as a function of the carrier lifetime in the AlGaN barrier τ_{SRH2}^{AlGaN}. A strong S_i dependence on barrier quality is observed: S_i increases from 2×10^3 to 2×10^5 cm/s as τ_{SRH2}^{AlGaN} decreases from 0.9 to 0.2 ns at $\Delta N = 5.4\times10^{19}$ cm^{-3} (circles in Figure 19a). Compared to bare-surface GaN layers, where surface recombination velocity, S, typically reaches $(1\text{-}5)\times10^4$ cm/s,[175–177,211] buffers with high quality barriers ($\tau_{SRH2}^{AlGaN} > 0.7$ ns) display improved boundary properties. Such improvement is observed in a wide range of III/V and II/VI material interfaces, e.g., $S \approx 1\times10^7$ cm/s in bare-surface GaAs[182] is greatly reduced with a cap based on p^+ GaAs layer ($S_i = 1.5\times10^4$ cm/s),[204] Ga_2O_3 layer ($S_i \approx 4.5\times10^3$ cm/s),[182] GaAs/AlAs superlattice ($S_i = 40$ cm/s),[212] AlGaAs layer ($S_i = 18$ cm/s),[213] or GaInP layer ($S_i = 1.5$ cm/s).[183] However, the GaN

buffers with moderate to low quality AlGaN barriers (τ_{SRH2}^{AlGaN} < 0.7 ns) suffer a substantial decrease in interface quality (Figure 19a). This trend has not been reported for nitride interfaces.

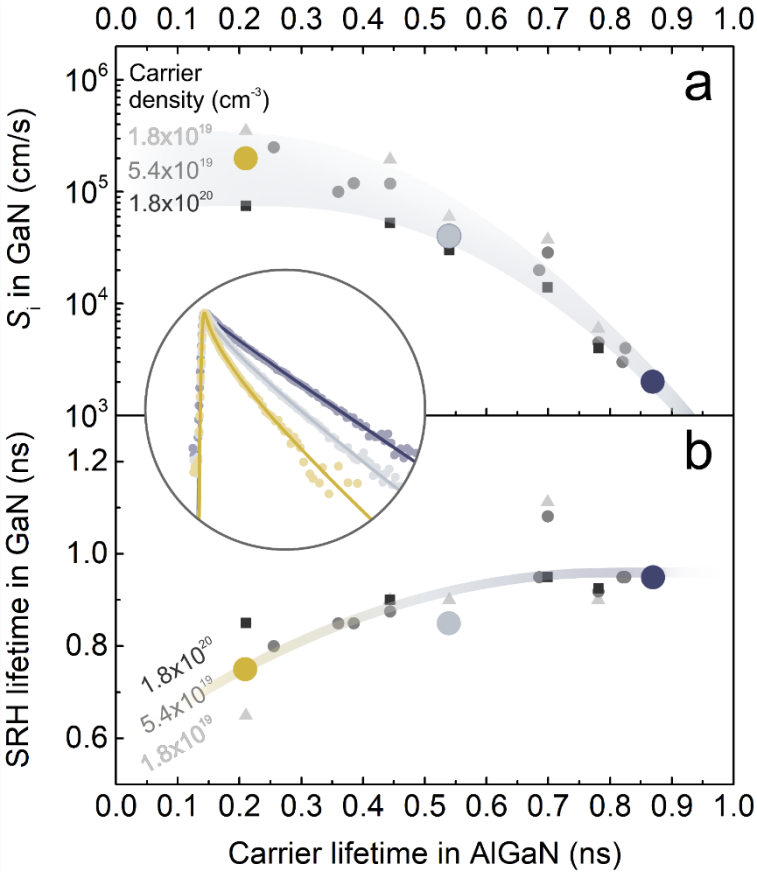

Figure 19. Interface recombination velocity S_i **(a)** and SRH carrier lifetime τ_{SRH}^{GaN} **(b)** at various carrier densities ΔN in GaN buffers as a function of carrier lifetime τ_{SRH2}^{AlGaN} in AlGaN barriers; the S_i and τ_{SRH}^{GaN} values signified as larger colored circles are extracted from the LITG transients demonstrated in the inset; inset transients (points) were recorded with pulses of 355 nm at $\Delta N = 5.4\times10^{19}$ cm^{-3} in GaN buffers; inset lines denote fitting with the (9) model. *Unpublished*.

Interface recombination velocity depends not only on the interface (barrier) quality but also on the carrier density. In the buffer with low quality barrier ($\tau_{SRH2}^{AlGaN} \approx 0.2$ ns) S_i gradually decreases from 3.5×10^5 to 7.5×10^4 cm/s with ΔN increasing from 1.8×10^{19} to 1.8×10^{20} cm^{-3}. However, increase in barrier quality weakens this dependence (see Figure 19a). Density-driven S_i decrease can be attributed to the saturation of interface recombination

channel, mirroring the $\tau^{GaN}(N)$ dependences discussed in the section of Figure 17.

Compared to the S_i dependence on τ_{SRH2}^{AlGaN}, the impact of barrier quality on the τ_{SRH}^{GaN} term is diminished: τ_{SRH}^{GaN} time features only a ~20% decrease as τ_{SRH2}^{AlGaN} decreases from 0.9 to 0.2 ns at $\Delta N = 5.4\times10^{19}$ cm^{-3} (circles in Figure 19b). Meanwhile, growth in carrier density ΔN causes a ~30% increase in the lifetime τ_{SRH}^{GaN} in the buffer with low quality barrier ($\tau_{SRH2}^{AlGaN} \approx 0.2$ ns), but has no perceptible effect on $\tau_{SRH}^{GaN}(N)$ dependence in buffers with higher quality barriers.

The depth-wise expansion of the barrier influence is implied by the shifting balance between the volume- and interface-bound recombination channels (characterized with τ_{GaN}^{SRH} and S_i coefficients, respectively). Moderate and high quality samples ($\tau_{SRH2}^{AlGaN} > 0.4$ ns) show little to no change in τ_{SRH}^{GaN}, while demonstrating significant variation in S_i (see respective dependences on τ_{SRH2}^{AlGaN} in Figure 19a, b), pointing to an interface-bound defective area. The depth-wise expansion of the barrier influence for the low-quality samples ($\tau_{SRH2}^{AlGaN} < 0.4$ ns) is observed as a decrease in τ_{SRH}^{GaN} with decreasing τ_{SRH2}^{AlGaN}. A mechanism of quality deterioration for the GaN buffer volume may be attributed to the diffusion of interface-degrading impurities, such as carbon and oxygen, or point defects, such as V_N and V_{Ga}, from the barrier (or the interface) to the buffer volume. For instance, multidirectional diffusion of V_N and V_{Ga} in GaN is expected at MOCVD-characteristic temperatures.[214,215] Such speculation is further supported by the saturation of the S_i increase with decreasing τ_{SRH2}^{AlGaN} paired with the simultaneous acceleration of τ_{SRH}^{GaN} decrease (see Figure 19): this juxtaposition implies a possible defect redistribution from the interface to the volume.

To finalize the characterization of the interface recombination processes in AlGaN/GaN heterostructures, an insight into the relation between the recombination velocity S_i and the internal quantum efficiency IQE is provided. For a model single quantum well (SQW) heterostructure with, say, one electrically active interface, the IQE can be roughly estimated using a simple rate equation:[175]

$$IQE = \frac{BN}{BN + 1/\tau_{SRH} + S_i/d} \quad (10)$$

where d is the thickness of the active region. Following this model, the IQE in a $d = 5$ nm SQW (AlGaN/GaN/AlGaN) drops by two orders of magnitude with the decrease in interface quality (with the increase in S_i from 2×10^3 to

2×10^5 cm/s) at $\Delta N = 1.8\times10^{19}$ cm^{-3}. In comparison, the adverse impact of surface recombination on a device wall-plug efficiency has been previously theoretically evaluated to be 5-7 percentage points for an InGaN-based LED and higher for UV LEDs.[178] The study in this thesis shows that in AlGaN/GaN heterostructures low-quality heterointerfaces may cause drop in the device efficiency significantly larger than that predicted before.

Highlights

- Carrier recombination and diffusion are studied in AlGaN/GaN heterointerfaces with AlGaN barriers of different quality, grown on identical GaN buffers
- The adverse barrier influence on carrier dynamics in the underlying buffer is revealed: AlGaN barrier accelerates the nonradiative carrier recombination in the GaN buffer
- The interface recombination velocity in the buffer increases hundredfold with decreasing barrier quality, and the dominating recombination mechanism switches from SRH to interface recombination. These phenomena are governed by a cumulative effect of various interface-deteriorating barrier defects
- Barrier-accelerated interface recombination can become a major carrier loss mechanism in AlGaN/GaN interface and may substantially limit the efficiency in nitride-based UV LEDs
- Contrary to the influence on carrier recombination, the AlGaN barrier does not affect the carrier diffusivity in the GaN buffer

Key finding C

- In AlGaN/GaN heterointerfaces, interface-deteriorating defects in AlGaN barrier alter and govern the carrier dynamics in the underlying GaN buffer: the interface recombination velocity in the buffer is increased with decreasing barrier quality, and the interface recombination pathway is transformed from the insignificant to the dominant one

Research opportunities

- In-depth analysis of atomic-scale AlGaN/GaN interface properties; identification of interface-deteriorating defects
- Study on carrier dynamics in other III-nitride-based interfaces, such as InGaN/GaN system


InN

Chapter D: Carrier dynamics in as-grown InN

In this chapter, I explore properties of carrier recombination and minority hole diffusion in as-grown InN with intrinsically high background electron concentration. Following the established pattern, I approach this study using density dependences of carrier lifetime (τ) and diffusion coefficient (D) as a main tool.

Since density dependence of τ can reveal the dominating recombination mechanism, extraction of this function has been an attractive and frequent target in previous studies. Unfortunately, the results of these works have been rather contradictory. Some studies report sublinear τ decrease with increasing carrier density (N),[216] while others – linear.[217–223] Some argue that carrier recombination is governed by SRH mechanism,[216,217,219,223] while others suggest trap-assisted Auger[218,222] as well as degeneracy-limited Auger channels.[220,221] Given the same data, some conclude that $\tau \propto N^{-1}$ dependence cannot be attributed to direct Auger recombination,[217,219] while others – profoundly disagree.[220] Alternatively, when studies agree on dominant recombination mechanism, dispute on other properties and parameters emerges (e.g., on discrepancies between reported N ranges where agreed upon recombination channel prevails). In general, picture on carrier recombination in InN is far from complete, and is clouded by ambiguous carrier lifetime/density estimation, observation of narrow density range, and reliance on small sample sets as well as widely scattered data.

Studies on carrier transport, especially that of holes, are more unanimous but less frequent. Theoretically, room temperature hole[g] mobility, μ_h, should reach ~200 cm^2/Vs in dislocation-free lightly-doped InN (with donor concentration, N_d, and hole concentration, P_h, below ~1×10^{17} cm^{-3}).[224] In moderately-doped n-InN (with N_d above ~1×10^{18} cm^{-3}), hole mobility should not exceed ~150 cm^2/Vs, while in moderately-doped p-InN (with P_h above ~1×10^{18} cm^{-3}) – ~100 cm^2/Vs.[224] Unfortunately, experimental confirmation of these fringe cases has been challenging. On one hand, InN is plagued by intrinsically high background electron concentration (N_e) and extreme surface electron accumulation (see Box D). On the other hand, conventional mobility measurements target majority carriers, and have difficulties with mixed-conductivity samples[h]. Therefore, extraction of hole mobility requires both

[g] Here, light and heavy holes are not distinguished.

[h] Heavily-doped p-InN still exhibits n-type conductivity at the layer surface due to surface electron accumulation.[275,276]

p-type InN (achieved at high acceptor concentrations exceeding N_d) and rather intricate experiments.

X. Wang et al.[225] extracted majority hole mobility μ_h = 17–36 cm^2/Vs in Mg-doped p-InN with Mg concentration of 6×10^{18} cm^{-3} and hole concentration $P_h = (1.4–3)\times10^{18}$ cm^{-3} from *sheet conductivity* measurements. Xie et al.[226] measured majority Hall mobility μ_h = 20-30 cm^2/Vs in p-InN with Mg concentration ranging from 10^{18} to 10^{20} cm^{-3} and $P_h = (0.8\text{-}3.5)\times10^{17}$ cm^{-3} using *infrared spectroscopic ellipsometry*. K. Wang et al.[227] combined *electrolyte capacitance voltage*, *thermopower*, *Hall*, and *sheet conductivity* experiments to estimate majority hole mobility μ_h = 55-66 cm^2/Vs in p-InN with Mg concentration of 1.1×10^{19} cm^{-3} and $P_h = (1\text{-}1.5)\times10^{18}$ cm^{-3}, as well as μ_h = 15-23 cm^2/Vs in InN with Mg concentration of 5×10^{19} cm^{-3} and $P_h = (2.1–3)\times10^{18}$ cm^{-3}. Anderson et al.[53] managed to extract mobilities for both majority heavy and light holes (μ_h = 50 cm^2/Vs and μ_h = 600 cm^2/Vs, respectively) in p-InN with Mg concentration of 3×10^{20} cm^{-3} using *variable magnetic field Hall* approach. Anderson's results suggest that hole mobility values reported in other studies (listed above) mainly depict transport of [majority] heavy holes.

Meanwhile, transport of minority holes has been investigated only skin-deep.[228,229] In one of the studies by Chen et al.,[228] minority hole mobility $\mu_h \approx 40$ cm^2/Vs was measured in unintentionally doped n-InN with low $N_e = 3.7\times10^{17}$ cm^{-3} using LITG technique[i]. Surprisingly, this μ_h value is not higher than those measured for majority holes in moderately-doped p-InN, and is much smaller than that predicted theoretically (for a given N_e, mobility should reach $\mu_h \approx 150$ cm^2/Vs).[224] Such discrepancy highlights strong dislocation scattering dominating at low acceptor concentrations.[224]

In this chapter, I investigate minority hole transport in yet unexplored electron density range spanning two orders of magnitude from 10^{18} to 10^{20} cm^{-3}. Additionally, I study unresolved properties of carrier recombination in a density range encompassing multiple recombination channels. This work features a large set of MOCVD- and MBE-grown samples as well as femtosecond-resolution temporal approach, avoiding ambiguities in carrier lifetime evaluation and carrier density calibration found in previous experiments. Results discussed here are published in Paper D.

[i] LITG approach does not require p-type conductivity for hole mobility evaluation; on the contrary, LITG-extracted ambipolar diffusion coefficient is governed by minority and/or low-diffusivity carriers. More on this in section *Carrier diffusion*.

LITG transients for InN feature single-to-multiple exponential components: single – at the lowest carrier densities, and multiple – at the highest. In this short section, extraction of transient decay rates from select transient components is described. Carrier dynamics parameters evaluated in a following manner are analyzed in the final thesis Chapters D and E.

Figure 20 shows LITG transients recorded in select InN epilayer (with intrinsic electron concentration $N_e = 1.3\times10^{19}$ cm^{-3}) at different photoexcited carrier densities ΔN; these transients are typical for all studied InN samples. One can see that carrier decay in InN becomes faster with increasing peak ΔN and slower with increasing delay. Due to this nonlinearity, instantaneous decay time is assessed in two fringe cases: either from the initial (τ_1; noted in Figure 20) or the tail (τ_2) transient component. The initial component is exploited to study carrier recombination and diffusion properties at various total carrier densities, $N = N_e + \Delta N$ – due to the well-defined ΔN. The tail transient region is used to study carrier dynamics at various background electron concentrations, N_e – in this regime, the photogenerated carrier density is diminished due to recombination, and is negligible compared to the background electron concentration ($\Delta N \ll N_e$).

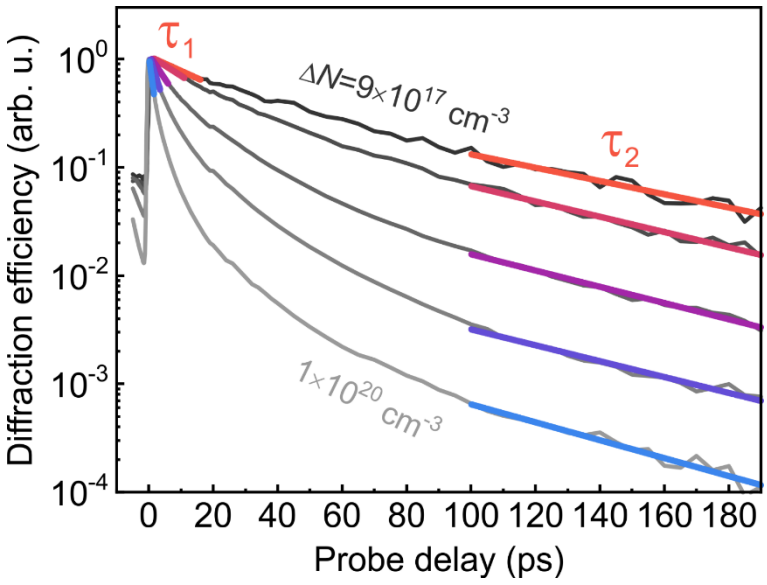

Figure 20. Normalized LITG transients recorded at different photoexcited carrier densities ΔN in InN epilayer with intrinsic $N_e = 1.3\times10^{19}$ cm^{-3}. Exponential fits in the initial (<20 ps) and tail (>100 ps) transient components are indicated by solid lines. *Adapted from Paper D*.

Figure 21a shows background electron concentration N_e dependence of carrier lifetime τ_2 extracted in low ΔN regime ($\Delta N \ll N_e$); each point corresponds to a different sample. For comparison, the carrier lifetimes reported in Ref.[218] for thin MBE-grown epilayers are also provided. The carrier lifetime values in thin (<0.4 μm) MOCVD-grown samples vary from 2 ps to 250 ps and are comparable to those in thin (<0.7 μm) MBE-grown epilayers with similar N_e, thus indicating a common recombination channel. The extracted MOCVD-lifetimes are among the longest reported for such-grown InN epilayers,[230] but shorter than those observed in the best >5.5-μm thick MBE-grown epilayers ($\tau \approx 1.3$ ns [223] or even 5.4 ns [228]). However, higher lifetime values may manifest in thicker MOCVD-InN, since quality of InN compounds is strongly bound to layer thickness (see Box D).

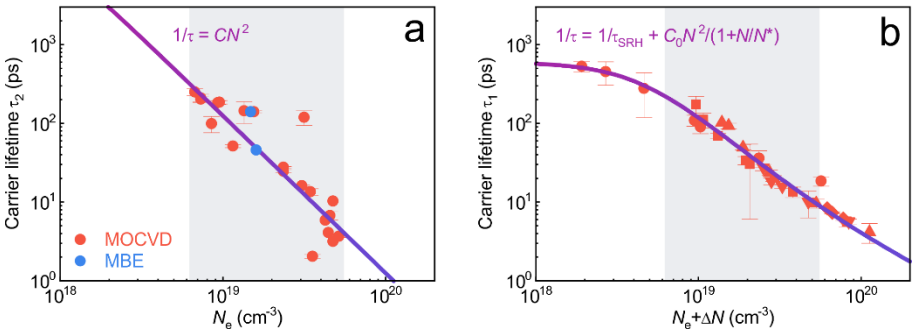

Figure 21. (a) Carrier lifetime τ_2 as a function of background electron concentration N_e in thin MOCVD- and MBE-grown epilayers; each point corresponds to a different sample. The solid line shows the fit $\tau = 1/CN^2$ with $C = 8\times10^{-29}$ cm^6/s. **(b)** τ_1 as a function of total electron density $N_e + \Delta N$; different symbols correspond to different samples. The solid line shows the fit according to Eq. (11) with the parameters $\tau_{SRH} = 600$ ps, $N^* = 5\times10^{19}$ cm^{-3}, and $C_0 = 8\times10^{-29}$ cm^6/s. Grey field in **(a)** and **(b)** highlights shared density range where $\tau \propto N^{-2}$ dependence is valid. *Adapted from Paper D.*

Box D. Control of background electron concentration

In InN, Hall-measured background electron concentration, N_e, comprises surface and bulk terms, one of which is intrinsic, while the other strongly depends on growth conditions and layer thickness.

In ultrathin InN layers, Hall N_e is governed by electrons accumulated at the interface between InN/buffer (or InN/substrate)[231] and at the surface layer.[232] *Surface electron accumulation* is an intrinsic InN property originating from extraordinary low Γ-point conduction band minima, causing donor-type surface states to be located in the conduction band.[233] Such accumulation occurs within the initial ~5 nm of InN surface (interface) and results in the localized N_e reaching ~4×10^{20} cm^{-3};[234] this N_e value does not depend (or depends weakly) on the overall layer thickness and growth conditions.[235]

In thick InN layers, Hall N_e is defined by thickness- and growth-dependent bulk N_e. In this case, Hall N_e decreases with increasing thickness due to the decreasing concentration of native donor-like defects induced by lattice mismatch.[236] Such defects may be bound to dislocations,[235] nitrogen vacancies,[235,237] or other structural faults.

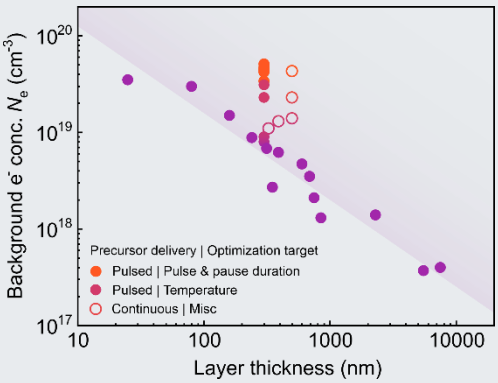

Figure D. Hall electron concentration N_e as a function of InN layer thickness; layers thinner than 500 nm were grown using MOCVD technique, while layers thicker than 600 nm – MBE; significant portion of MBE-data is obtained from Refs.[218,223,228]

The combination of surface- and bulk-governed N_e properties results in approximately linear thickness dependence of Hall N_e, demonstrated in Figure D for studied MOCVD-layers (thinner than 500 nm) and state of the art MBE-layers (thicker than 600 nm); MBE-data are collected from this study and Refs.[218,223,228] Although substantial portion of MOCVD-data follows the same thickness function as MBE-data (see purple circles), several MOCVD-samples (corresponding to orange and red circles) feature higher than optimal N_e values. This is due to low bulk structural quality deteriorated by growth at suboptimal conditions. For instance, data depicted by full orange circles correspond to series of growth efforts intended for optimization of pulse and pause durations (pulsed precursor delivery case); full red circles – for optimization of interlayer and layer growth temperatures (pulsed precursor delivery case); and open circles – for simultaneous optimization of growth temperature and gas flow rates (continuous precursor delivery case; additional info on sample growth is provided in *Samples* section). Meanwhile, growth-optimized MOCVD-layers feature rather low N_e values (for a given sample thickness), and depict CVD-based approaches as a promising alternative to expensive and hardly scalable MBE approach.

In Figure 21a, τ_2 scales as $1/N_e^2$, thus suggesting direct Auger recombination as dominant recombination channel in InN. This dependence can be fitted using the function $\tau = 1/CN^2$ with Auger coefficient $C = 8\times10^{-29}$ cm^6/s (see solid line), and the extracted Auger coefficient fits well to a general trend of C versus the material bandgap.[127] However, super-linear $\tau_2 \propto N_e^{-2}$ dependence contradicts the previously reported trends $\tau \propto N^{-1}$ or $N^{-0.5}$.[216–223] Such discrepancy is probably caused by ambiguities in the lifetime determination and carrier density calibration found in previous studies. For instance, photoreflectance spectroscopy (used in studies[216,217,219,221]) is sensitive to a depth-wise carrier diffusion, while LITG experiments performed in transmission geometry (like measurements in this thesis) are unsusceptible to this issue.[238] The differential transmission spectroscopy (used in studies[217,222,223]) provides different transient decay rates for different probe wavelengths, thus hindering evaluation of actual carrier recombination rates.[222] Finally, previous LITG experiments[218] were limited in temporal resolution (25 ps in Ref.[218] vs. 250 fs in this work).

Next, properties of carrier recombination are explored in a wider density range, expanded both towards lower and higher density wings. Higher carrier densities are achieved by elevating the photogenerated portion (ΔN) of total electron density $N = N_e + \Delta N$ and by analyzing τ_1 transient component. Lower density wing is attained by inclusion of higher quality sample – 2.3-μm thick MBE-grown InN epilayer. The $\tau_1(N)$ dependence obtained from select few samples is demonstrated in Figure 21b. Here, grey field highlights the initial density range ($N \approx 7\times10^{18} \div 5\times10^{19}$ cm^{-3}) studied in Figure 21a as well as the N range for valid $\tau_1 \propto N^{-2}$ trend. At densities outside this field, $\tau_1(N)$ dependence deviates from the conventional Auger form. This deviation can be accounted for using the following model:

$$\frac{1}{\tau} = \frac{1}{\tau_{SRH}} + C(N)N^2 \tag{11}$$

which includes the SRH term ($1/\tau_{SRH}$) dominating at low N as well as the state filling-affected Auger term ($C(N)N^2$) prevailing at high N; and excludes the negligible radiative recombination term. At extremely high carrier densities (such as those beyond the grey field in Figure 21b), carrier degeneracy- and state filling-affected Auger coefficient tends to decrease with increasing N, thus saturating Auger recombination rate, as reported in phosphides, arsenides as well as nitrides.[125,220,239] This $C(N)$ trend can be described using the same approach as that applied to density-dependent $B_{rad}(N)$ coefficient in AlGaN-case (see Chapter A):[125]

$$C(N) = \frac{C_0}{\left(1+\frac{N}{N^*}\right)} \tag{12}$$

Here, C_0 is the initial Auger coefficient and N^* is a material-specific carrier density indicating the transition from the pre-degenerate to the degenerate Auger recombination. Combination of Eq. (11) and (12) with the parameters $N^* = 5\times10^{19}$ cm^{-3} and $C_0 = 8\times10^{-29}$ cm^6/s provided a good fit to the experimental data (see Figure 21b); this C_0 value is the same as C value estimated for data in Figure 21a. Although electrons become degenerate in InN at a rather low carrier density (~3×10^{17} cm^{-3} according to calculations), high N^* value implies that the impact of degeneracy on the carrier recombination emerges much later. This may be due to high hole mass and late hole degeneracy.

Carrier diffusion

Figure 22a shows the ambipolar diffusion coefficient (D_1; extracted from the initial LITG transient components) as a function of the total electron density; the data depicted here correspond to the same samples as those analyzed in Figure 21b. The ambipolar diffusion coefficient is related to the monopolar electron (hole) diffusion coefficients $D_{e(h)}$ by the expression:

$$D = \frac{N+P}{\frac{P}{D_e}+\frac{N}{D_h}} \tag{13}$$

where $N = N_e + \Delta N$ and $P = \Delta P = \Delta N$ are the total electron and hole densities, respectively. According to Eq. (13), if $N \gg P$, then $D \approx D_h$, i.e., the ambipolar carrier diffusion is defined by the minority hole diffusion. In the studied InN samples, this condition is satisfied for densities below mid-10^{19} cm^{-3}. At higher N values, ambipolar diffusion coefficient gradually deviates from D_h.

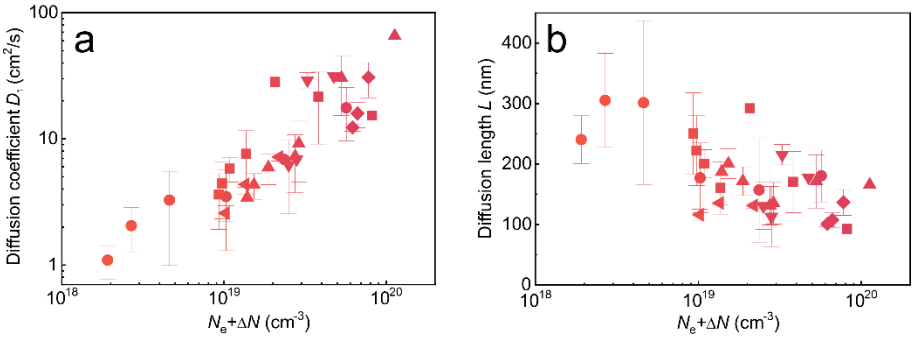

Figure 22. Dependences of diffusion coefficient D_1 **(a)** and diffusion length L **(b)** on total electron density; different symbols correspond to different samples. *Adapted from Paper D.*

As shown in Figure 22a, the increase in carrier density from $N \approx 2\times10^{18}$ cm^{-3} to 1×10^{20} cm^{-3} results in an increase in the diffusion coefficient from $D_1 = 1$ cm^2/s to 30-65 cm^2/s. At a low carrier density, the observed diffusion coefficient is similar to that reported for high-quality MBE-InN epilayers with a low background electron concentration ($D \approx 2$ cm^2/s at $N_e \approx (0.4\text{-}1.4)\times10^{18}$ cm^{-3} [228,229]). However, the subsequent growth of D_1 to such an extent is highly unusual: the previously reported nondegenerate heavy hole and light hole mobilities in InN ($\mu_h = 50$ cm^2/Vs and 600 cm^2/Vs)[53] correspond to the hole diffusion coefficients ($D_h \approx 1.25$ cm^2/s and 15 cm^2/s, respectively) much smaller than the peak D_1 values measured in this study. Such extreme carrier diffusivity becomes more sound considering carrier degeneracy as well as picosecond-scale carrier transport phenomena – discussed in the following paragraph.

In the case of degenerate system, the hole diffusion coefficient is related to the hole mobility by the generalized Einstein expression:[240]

$$D_h = \frac{kT}{e}\mu_h \frac{F_{1/2}}{F_{-1/2}} \tag{14}$$

where k is the Boltzmann constant, e is the elementary charge, and $F_{\pm1/2}$ are the Fermi-Dirac integrals. According to Eq. (14), the degeneracy of heavy holes at a density equal to 10^{20} cm^{-3} can account for the increase in D_1 up to a value of 20 cm^2/s – anything higher than that requires contribution of high-mobility light holes. In InN, population of light holes can be expected within a timescale of carrier thermalization. Conveniently, carrier lifetimes extracted at a high carrier density are comparable to carrier thermalization time.[241] Therefore, extreme D_1 values observed at both a high carrier density (see Figure 22a) and short carrier lifetime (see Figure 21) may be a result of degenerate light hole transport. Additionally, short-timescale diffusivity may be enhanced by ballistic-like hole transport, which is a similar phenomenon to a velocity-overshoot observed in short-carrier-lifetime GaAs.[242]

Next, the extracted diffusion coefficient (D_1) and carrier lifetime (τ_1) are used to estimate the diffusion length ($L = \sqrt{\tau_1 D_1}$), which is a key parameter describing the performance of a bipolar device. In Figure 22b, the assessed diffusion length is depicted as a function of the total electron density; here, L values correspond to the same samples as those analyzed in Figure 21b and Figure 22a. Usually, a decrease in a carrier lifetime causes a decrease in a diffusion length. In contrast to such trend, this study shows that in InN the drop in τ_1 is compensated by the simultaneous increase in D_1 (see Figure 21 and Figure 22a). Therefore, the diffusion length varies insignificantly with

carrier density: in a density range from 2×10^{18} to 1×10^{19} cm^{-3}, the average L decreases from ~280 nm to ~160 nm, while at densities above 1×10^{19} cm^{-3}, L remains approximately constant at ~160 nm (see Figure 22b).

As a simple assessment of the carrier extraction conditions in a hypothetical bipolar device, one can check if the carrier diffusion length L exceeds the light absorption depth, $1/\alpha$, where α stands for the optical absorption coefficient. As the absorption edge in the studied epilayers increases from ~0.7 to 1 eV with the background electron concentration (a.k.a. *Burstein-Moss* shift[243–246] – a common phenomenon in InN), the value of α was picked at 1.2 eV. In this case, the measured α is higher than 6×10^{4} cm^{-1} in any investigated sample, while the average L does not decrease below ~160 nm in the observed N range, thus allowing for carrier transit within the region of $1/\alpha$ without recombination. This first-order assessment shows that the extraction of the photogenerated carriers in InN is essentially possible even in the lowest quality InN compounds with the highest electron concentrations.

Highlights

- Carrier recombination and minority hole diffusion were studied in as-grown InN within a wide range of carrier density, controlled by a sample growth and photoexcitation
- Carrier lifetimes in thin MOCVD-grown InN reach ~250 ps and are comparable to those in thin MBE-grown epilayers
- Direct Auger recombination is the dominant recombination mechanism at elevated carrier densities and is described with Auger coefficient $C = 8\times10^{-29}$ cm^6/s; at the highest carrier densities, Auger recombination is hindered by a phase-space filling phenomenon
- Minority hole diffusion coefficient increases more than tenfold with increasing carrier density; such significant increase is linked to the cumulative effect of hole degeneracy and picosecond-scale carrier transport phenomena
- Density-induced decrease in carrier lifetime is compensated by the simultaneous increase in carrier diffusion coefficient, thus causing insignificant variation in carrier diffusion length confined within ~160 – 280 nm range

Key finding D

- In u-InN, properties of carrier dynamics are strongly bound to the total electron density (corresponding to the background and excess electrons): at densities above mid-10^{18} cm^{-3}, the diffusion coefficient increases super-linearly with increasing electron density, while the carrier lifetime decreases; the latter is governed by the direct Auger recombination and the phase-space filling phenomenon

Research opportunities

- Study of carrier recombination at various temperatures for estimation of radiative recombination coefficient *B*
- Confirmation of extreme minority hole diffusivity using other than LITG approach
- Investigation of carrier dynamics properties in p-type InN

Chapter E: Carrier dynamics in proton-irradiated InN

In this chapter, I study impact of spacelike energetic particle radiation on carrier dynamics in InN; gauge radiation resistance in InN; and compare it to that in other semiconductors employed in space-bound photovoltaic (PV) applications; these results are published in Paper E. On first glance, investigation of radiation resistance in the material featuring single-percent power conversion efficiencies[45,57] seems to be rather futile. However, low efficiency values may be non-essential in radiation-harsh environments, where material parameters at the end of life are more important than the initial ones.[247] In such environments, nitride family member – GaN – proved to be strikingly resilient,[248,249] suggesting not-too-far performance for InN as well.

The existing investigative efforts into radiation effects on InN are scarce and mostly limited to Hall measurements.[54,234,250] These studies demonstrate that electron, proton, and He^+ ion irradiation causes an increase in the background electron concentration in InN or in In-rich InGaN compounds,[234,250] contrary to GaN or GaAs,[234] and propose that irradiation can be used as a manner for n-type doping control.[250] Despite interesting proposals, current research still lacks data on basic carrier dynamics parameters (such as carrier lifetime) in irradiated InN; comparison between radiation resistances in InN and other materials;[j] and tuning of synthetic irradiation conditions against space-bound environment.

In space, the naturally occurring particles causing the highest damage are protons trapped in the magnetosphere (within the Van Allen belts) and protons ejected during solar particle/proton events (SPEs; such as solar flares and coronal mass ejections); the former dominate in low earth orbit (or in the vicinity of other planets with strong magnetic field), while the latter – in deep space environment.[251] The most harmful protons responsible for displacement of atoms have energies on the order of kiloelectronvolts – just above the atomic displacement threshold, while protons of higher velocity are less damaging.[252] This energy-dependent proton damage coefficient is characterized by material-specific nonionizing energy loss (NIEL) function – the rate at which particle energy is transferred to the lattice due to atomic displacements;[253] NIEL(E) curve for InN is depicted in Figure 23. Usually, semiconductor devices are protected by shielding and/or the active region of

[j] An informative comparison of radiation resistance in InN to that in $In_xGa_{1-x}N$ alloy family, GaAs, and GaInP is present in Ref.[274] – however, the analysis is performed for a narrow range of radiation doses and is limited to a single InN sample.

the device is not in the extreme surface. In this case, most-damaging low-energy protons lack the penetration depth and are stopped,[k] while low-impact high-energy protons are slowed down. A fraction of latter protons is slowed down to harmful low energies, however, the impact of these protons to device degradation is small due to limited proton flux in high-energy wing of solar proton spectra.[253,254] Taking this into account, the energy of protons reaching the active device region and contributing to device degradation the most shifts towards higher values, specifically: $1 \div 10$ MeV[253,255] (noted in Figure 23). Since protons of this energy replicate harmful space environment most closely, they are usually employed for radiation testing of uncovered materials in a particle accelerator; considering that, this work used protons accelerated to 1.4 MeV.

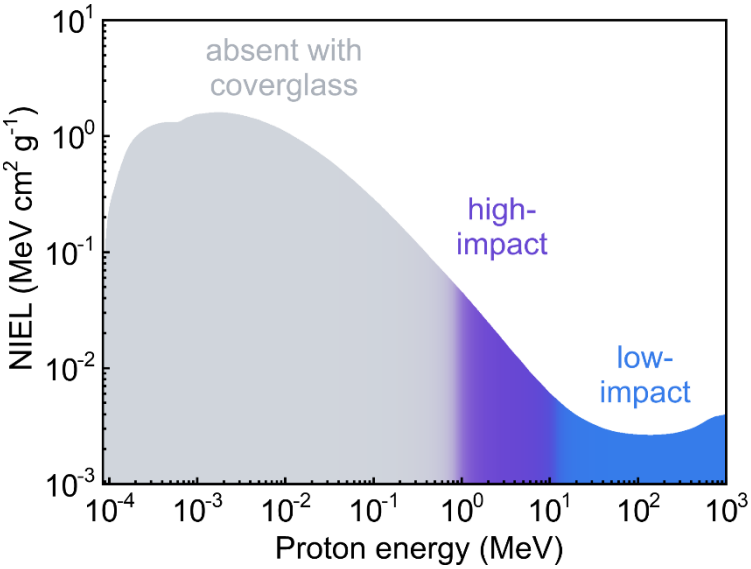

Figure 23. The energy dependence of nonionizing energy loss (NIEL) for protons in InN; curve was obtained using the SR-NIEL calculator.[256]

In space-bound environment, proton flux/fluence depends on particle energy and solar activity both in case of trapped particles and SPEs. For trapped particles, 1-MeV proton flux can reach ~10^7 cm^{-2}s^{-1} in the inner Van Allen belt,[257,258] while for SPEs, annual 1-MeV proton fluence can be as high as 10^{11} cm^{-2} in interplanetary space[254] (corresponding to the average flux on the order of $10^3 \div 10^4$ cm^{-2}s^{-1}). In comparison, this work features proton

[k] Coverglass of ~76-μm thickness will stop protons with energies <3 MeV incident at >60° angle.[253]

fluences reaching 10^{16} cm^{-2}. Radiation intensity approaching the latter value can be encountered during exceptionally intense SPEs (e.g., 1-MeV proton fluence of mid-10^{11} cm^{-2} was accumulated during the *Carrington* event (September 1-2, 1859) – the largest event observed in the past 500 years);[259] after exoatmospheric nuclear detonations (e.g., the *Starfish Prime* test increased the trapped electron flux by a factor of 100[260]); and in the Jovian magnetosphere (a factor of several thousands higher proton flux than that in the Earth's magnetosphere[260]).

For this study, three MOCVD-grown samples with background electron concentrations of $N_e = 1.3\times10^{19}$ cm^{-3} (sample *S1*), 5.9×10^{19} cm^{-3} (*S2*), and 1.9×10^{19} cm^{-3} (*S3*) were selected from the sample set investigated in Chapter D. To replicate the effects of spacelike radiation environment, the samples were irradiated with 1.4 MeV protons using a *Tandetron* ion accelerator coupled with a *Hiconex* Cs-ion sputter source; the procedure was performed by Dr. Vitalij Kovalevskij (Center for Physical Sciences and Technology, Lithuania). Each of the three samples (S1-S3) was cut into six parts, and five of the parts were exposed to different proton fluences. The proton fluence (ϕ) was varied by selecting the exposure time and ranged from $\phi = 1\times10^{12}$ to 1×10^{16} cm^{-2}. The incoming particles were treated as swift ions since the penetration depth of the 1.4 MeV protons in InN (~25 μm) substantially exceeds the layer thickness (<390 nm). The calculation for the proton penetration depth was performed with widely used SRIM (*the Stopping and Range of Ions in Matter*) freeware.[261] Finally, irradiation-induced changes in the carrier dynamics were studied using the LITG technique.

Irradiation impact on carrier dynamics

The evolution of carrier lifetime τ_2 with proton irradiation is demonstrated in Figure 24a; τ_2 was extracted from the tail LITG decay region governed by N_e (see *Extraction of LITG decay rates* section in Chapter D for details). The carrier lifetime in the virgin InN epilayers ranges from ~100 ps (in higher-quality samples S1 and S3) to 13 ps (in lower-quality sample S2), and is linked to the background electron concentration (see *Carrier recombination* section in Chapter D). In the irradiated epilayers, carrier lifetime does not change with proton fluence up to $\phi = 10^{14}$ cm^{-2}. However, irradiation with a proton fluence above 10^{14} cm^{-2} results in a sharp decrease in carrier lifetime, and fluence of 10^{16} cm^{-2} reduces τ_2 to several picoseconds in all samples (see Figure 24a). Provided that the primary nonradiative process in InN at high carrier densities is Auger recombination, the irradiation-induced decrease in the carrier lifetime should be related to the creation of additional background carriers.

This surge of free electrons coinciding with the drop in τ_2 was confirmed by the Hall N_e measurements and is demonstrated in Figure 24b.

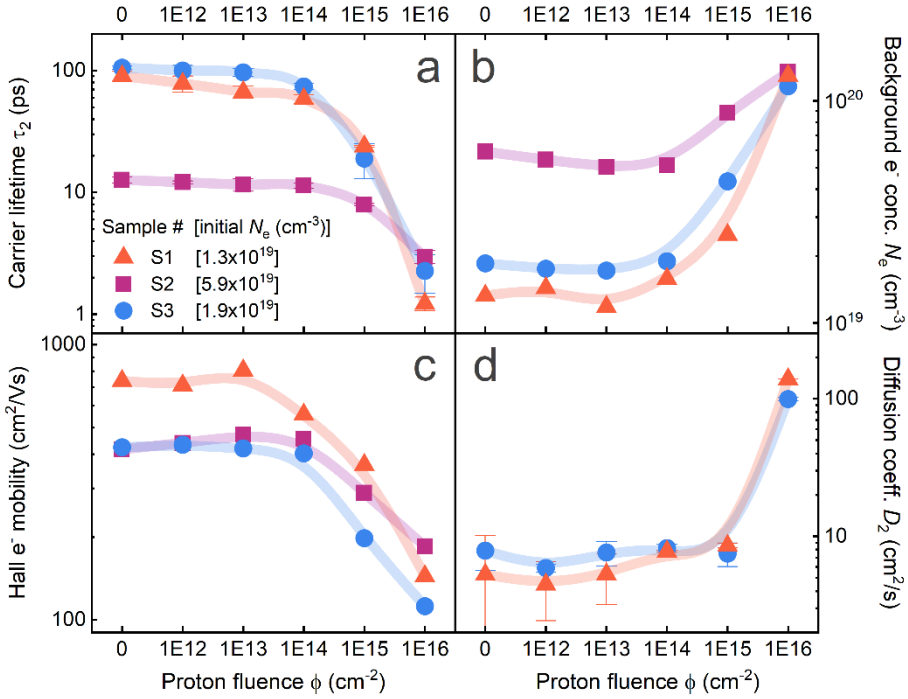

Figure 24. Carrier lifetime **(a)**, background electron concentration **(b)**, Hall electron mobility **(c)**, and ambipolar diffusion coefficient **(d)** dependence on the proton fluence in InN epilayers with different initial background electron concentrations (indicated). *Adapted from Paper E*.

Free electrons in as-grown InN originate from: the surface states (a.k.a. *surface electron accumulation* phenomenon),[52] impurities, such as hydrogen[262] and oxygen,[263,264] native point defects, such as nitrogen vacancies,[265,266] and dislocations;[235] several of these cases were briefly discussed in Chapter D (see Box D). In irradiated InN, choice of irradiation-induced free electron 'sources' is more limited. On first glance, irradiation-induced incorporation of donor-like impurities is sound for H^+ ions (protons), however, H^+ introduction is implausible due to large 1.4-MeV proton penetration depth (~25 μm) compared to the sample thickness (<390 nm). In surface electron accumulation case, surface electron concentration is limited by surface Fermi level pinning energy, which is irradiation-independent.[234] Similarly to that, dislocation density is also not affected by irradiation, or affected insignificantly.[267] That leaves native point defects as most probable irradiation-induced free electron source, in agreement with the experimental

results by Walukiewicz et al.[250] Meanwhile, calculations for defect formation energies by Van De Walle et al.[264] can tentatively identify these defects. Such approach seeks for candidates of donor-like nature with low formation energy and converges to – nitrogen vacancy V_N.

Next, irradiation impact on carrier transport is investigated. The dependence of the Hall electron mobility, μ_e, on the proton fluence is shown in Figure 24c. The Hall electron mobilities in virgin samples vary from 420 to 810 cm^2/Vs and do not correlate with the background electron concentration. Although such lack of correlation is generally not expected,[262,265,266] it has been occasionally reported and tentatively attributed to various differences in InN structural quality.[250] In irradiated samples, the electron mobility decreased to 110 – 190 cm^2/Vs with increase in proton fluence up to 10^{16} cm^{-2}, and hidden correlation between μ_e and N_e – emerged. This correlation can be described using a function $\mu_e \propto N_e^{-0.9}$, and can be attributed to enhanced electron scattering by irradiation-induced point defects,[250] specifically – triply and singly charged donors.[168]

So far, the presented effects of proton irradiation on the InN properties follow a predictable pattern, and the changes in electron concentration or mobility correspond well to those previously reported. However, analysis of the previously unreported irradiation effects on hole diffusivity presents unanticipated results.

Figure 24d shows the dependence of the ambipolar diffusion coefficient D_2 on the proton fluence in two InN epilayers with similar background electron concentrations (samples S1 and S3). The depicted D_2 values are extracted from the tail transient region governed by N_e and correspond to minority hole diffusion, $D \approx D_h$ (according to Eq. (13) in Chapter D). The most striking proton-irradiation effect is the more than ten-fold increase in the diffusion coefficient from values of 5 – 8 cm^2/s in the virgin layers up to 100 – 140 cm^2/s in the layers irradiated with proton fluences up to 10^{16} cm^{-2}; analogous increase in D_2 was replicated at various excitation levels. Such a high hole diffusion coefficient has not been reported in InN before. Not only that, hole transport in general could not been observed in highly-irradiated InN using conventional majority-carrier techniques, since irradiation-introduced donor-like defects switch the p-type conductivity into an n-type at relatively low particle fluences.[54]

Taking cue from the study in Chapter D, further investigation of carrier dynamics concerns the relationship between the total electron density, $N = N_e + \Delta N$, and both the diffusion coefficient D_1 and the lifetime τ_1. Here, D_1 and τ_1 values are extracted from the initial LITG decay region, governed

by both background and excess carriers. Excess carrier density ΔN is controlled by photoexcitation intensity, while background electron concentration N_e – by growth conditions (initial N_e) and proton irradiation (increase in N_e). As a result of these efforts (combination of different epilayers, irradiated and photoexcited at various levels), a set of >40 distinct data for D_1 and τ_1 is obtained, and the range of the total electron density spanning from 1.4×10^{19} to 1.5×10^{20} cm^{-3} is covered.

The extracted D_1 and τ_1 values are depicted in Figure 25a and b, respectively, vs. the total electron density. In Figure 25a, the carrier lifetime decreases super-linearly from 60 ps to 1 ps with increasing electron density N, similarly to $\tau_1(N)$ dependence for virgin MOCVD- and MBE-InN discussed in Chapter D. Such decrease is governed by direct Auger recombination (suppressed by phase-space filling) and can be described using the same ABC form as that exploited in Chapter D (see Eq. (11) and (12), also noted in Figure 25a). This model paired with the coefficients $N^* = 5\times10^{19}$ cm^{-3} (characteristic carrier density) and $C_0 = 8\times10^{-29}$ cm^6/s (initial, 'pre-degenerate' Auger coefficient) provided a good fit to the entire data set (see line in Figure 25a), and the coefficients matched those reported in Chapter D. Meanwhile, impact of SRH recombination ($1/\tau_{SRH}$ term in Eq. (11)) was insignificant in the given density range and thus – neglected. The fact that carrier recombination in virgin and irradiated samples of different quality, photoexcited at various levels, and grown using different techniques can be described by a single equation with the same set of parameters indicates that: (i) free electron origin (intrinsic, photogenerated, or irradiation-raised) does not affect carrier recombination — electron density does; (ii) the impact of defects (growth- and irradiation-induced) to carrier recombination at high electron densities is limited to that of an electron source to the Auger process.

In case of $D_1(N)$ function, the increase in electron density results in a super-linear increase in the diffusion coefficient (see Figure 25b). At electron densities $N \approx 10^{19} \div 10^{20}$ cm^{-3}, the observed D_1 values replicate those reported for virgin MOCVD- and MBE-InN ($D_1 \approx 3 \div 65$ cm^2/s; see Figure 22a in Chapter D). Meanwhile, densities above 10^{20} cm^{-3} (not observed in Chapter D) result in diffusion coefficient as high as ~190 cm^2/s (at $N = 1.5\times10^{20}$ cm^{-3}). Similarly to carrier recombination case, match between D_1 values for virgin and irradiated samples (at corresponding N) indicates that free electron origin has little-to-no effect on hole diffusion. Additionally, such match implies that it is not irradiation per se that enhances hole diffusivity, but irradiation-increased N and -decreased τ, i.e., the conditions when simultaneous

contributions from carrier degeneracy and picosecond-scale carrier transport effects are expected (see *Carrier diffusion* in Chapter D).

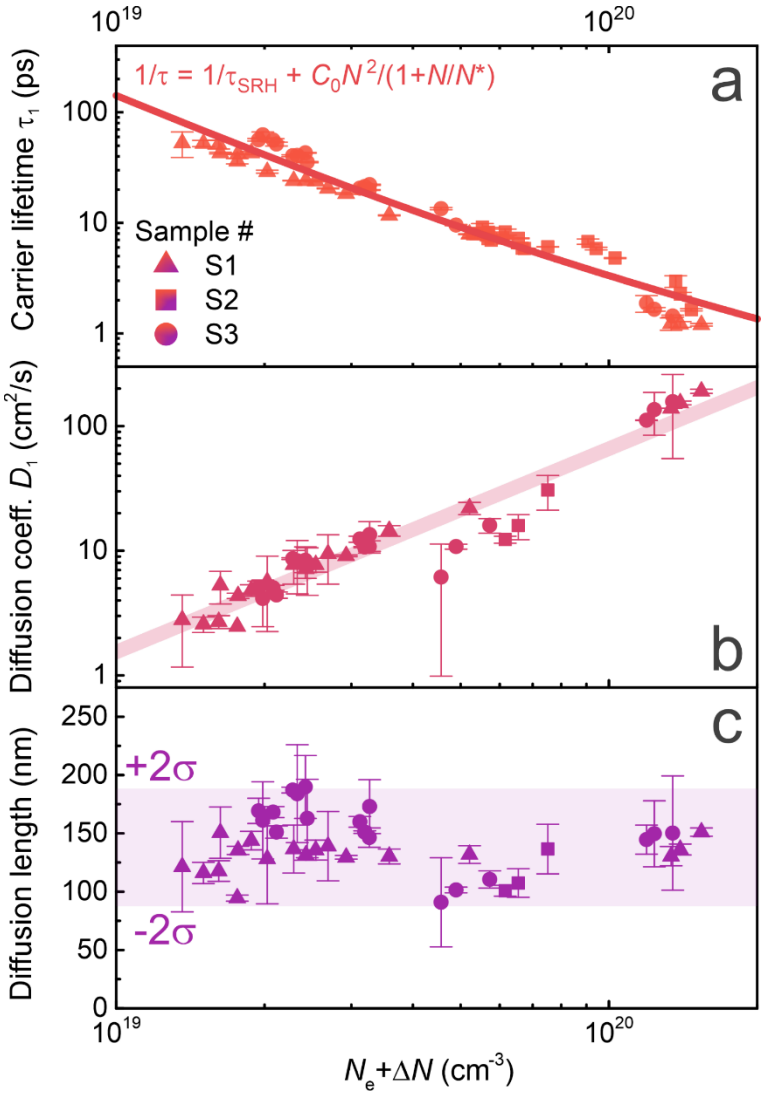

Figure 25. Dependence of the carrier lifetime **(a)**, ambipolar diffusion coefficient **(b)**, and diffusion length **(c)** on the total electron density in InN epilayers. Line denotes fitting with the modified ABC model in **(a)** and a guide for the eye in **(b)**. *Adapted from Paper E*.

Next, impact of an increasing carrier density (irradiation- and photoexcitation-increased, or intrinsically higher) on carrier diffusion length ($L = \sqrt{\tau_1 D_1}$) is investigated (depicted in Figure 25c as $L(N)$). Such monitoring of L is important in space-bound devices (e.g., photodetectors or

solar cells), where radiation response of L controls the end-of-life parameters.[268] This study shows that an increasing carrier density causes a substantial decrease in the carrier lifetime (Figure 25a). However, in the studied N range, the average diffusion length remains approximately constant at ~140 nm due to a simultaneous increase in the diffusion coefficient (see Figure 25c, b). This L value is similar to that in virgin MOCVD- and MBE-InN ($L \approx 160$ nm in corresponding N range; see Figure 22b) and exceeds the light absorption depth $1/\alpha$ for band-to-band excitation. The latter condition allows for carrier transit within the region of $1/\alpha$ without recombination and shows that the extraction of the photogenerated carriers in thin InN is essentially possible even at the highest irradiation levels and electron densities. Nevertheless, in an actual bipolar device, irradiation-induced degradation of other critical parameters (such as p-type conductivity) could prevail and considerably affect carrier transport.

Resistance to spacelike radiation

A basic parameter describing the rate of irradiation-caused τ degradation (and the material radiation resistance) is the lifetime damage factor, $K_\tau = (1/\tau_\phi - 1/\tau_0)/\phi$,[269] where $\tau_{0(\phi)}$ is the carrier lifetime before(after) irradiation. For the InN irradiated in this study by 1.4 MeV protons, K_τ is equal to 8×10^{-5} cm^2/s, while for rad-soft GaAs compounds $K_\tau \approx 67\times10^{-5}$ cm^2/s (measured for 1.8 MeV proton irradiation).[269] The comparison of these K_τ values depicts InN as more radiation resistant than GaAs, although the difference is smaller than expected (considering superior rad-resistance in GaN). However, K_τ-description may be inaccurate and rather superficial: K_τ only describes the degradation rate above a certain threshold of particle fluence ϕ, but not the threshold itself. Additionally, K_τ depends on particle energy, making data comparison between different studies and materials challenging.

For a more appropriate comparison of the radiation resistance in InN with that in other semiconductors, one can compare normalized τ dependences on displacement damage dose, D_d – a unique dose unit suggested by Naval Research Laboratory (NRL) and tailored to describe degradation of photovoltaic parameters by a single curve for all particle energies.[253] NRL methodology is applicable for traversing particles (electrons or protons) and is most accurate for particle energies in range $0.1 \div 10$ MeV (for protons), where interaction between incident proton and the target atom is primarily Rutherford in nature.[253] The conversion of proton fluence to displacement damage dose is achieved using the following equation:[253]

$$D_{\mathrm{d}} = \phi \times S(E) \tag{15}$$

where $S(E)$ is the energy-dependent, material-specific damage coefficient, corresponding to the nonionizing energy loss function (NIEL; the function can be obtained using the SR-NIEL calculator[256]).

The dependence of the carrier lifetime on the displacement damage dose for InN epilayers (data for samples S1 and S2 from Figure 24a), GaAs-, InGaAs-, and InGaN-based LEDs (data from previous reports[269–272]) is shown in Figure 26. The carrier lifetime data for the high-energy (68 – 506 MeV) proton-irradiated bulk GaAs LEDs were obtained from direct measurements performed by Barry et al.[269] The analogous degradation curve for 10 MeV-proton-irradiated bulk GaAs LED was obtained from the light output intensity, I, measurements performed by Warner et al.,[272] assuming that $I \propto \tau$.[272,273] The degradation curves for the directly measured and the estimated carrier lifetimes match fairly well between different GaAs samples irradiated with protons of different energies, reinforcing the validity of the NRL method and the $I \propto \tau$ assumption. Based on the latter verification, degradation curves for InGaAs[270] and blue InGaN[271] quantum well (QW) LEDs (irradiated with 10-MeV protons) were also obtained from the I measurements due to lack of τ data.

As demonstrated in Figure 26, the proton-radiation resistance in InN (circles) surpasses that in GaAs-based LEDs (triangles and diamonds) and the InGaN LED (squares). However, the degradation rates for InN samples with different initial background electron concentration ($N_e^{\phi=0}$) are not unanimous: higher $N_e^{\phi=0}$coincides with higher lifetime drop-off threshold. Such discrepancy invites the speculation whether the apparent high damage threshold in the studied InN would still manifest in a low-electron-concentration InN. This notion could be examined by predicting the τ degradation curve for a hypothetical InN layer with $N_e^{\phi=0} = 0$, provided the same model ensures a good fit to the experimental data for the studied InN samples (circles in Figure 26).

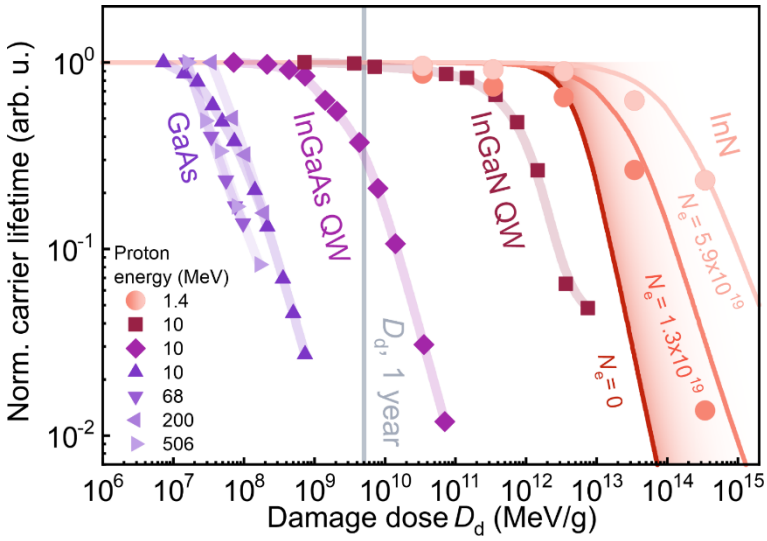

Figure 26. Dependence of the normalized carrier lifetime on the displacement damage dose in proton-irradiated InN samples (S1, S2) with different initial background electron concentrations (circles, $N_e^{\phi=0}$ indicated) and the corresponding dependence previously obtained for bulk GaAs LEDs[269,272] (triangles), InGaAs QW LED[270] (diamonds), and blue InGaN QW LED[271] (squares). The opaque lines depict the carrier lifetime degradation curves calculated for samples S1, S2, and a hypothetical zero-electron-concentration InN ($N_e^{\phi=0} = 0$). The vertical gray line indicates the upper limit of predicted solar proton damage dose accumulated in InN in a year-long space mission. *Adapted from Paper E*.

Since the lifetime in InN is governed by Auger recombination regardless the origin of free carriers (as shown in Figure 25a and discussed above), lifetime degradation can be described using Eq. (11). For InN data depicted in Figure 26 (τ extracted from tail transient components) the total electron density N was expressed as:

$$N = N_e = N_e^{\phi=0} + N_e^{\phi>0}(\phi) \tag{16}$$

where the insignificant photogenerated electron density term (ΔN) is neglected, and the function of irradiation-dependent electron concentration ($N_e^{\phi>0}(\phi)$) is estimated from Figure 24b. Next, the $N_e^{\phi>0}(\phi)$ term was converted to $N_e^{\phi>0}(D_d)$ using Eq. (15), and, finally, the dependence $\tau(D_d)$ was obtained. The $\tau(D_d)$ curves were calculated using the parameters $N^* = 5\times10^{19}$ cm^{-3}, $C_0 = 8\times10^{-29}$ cm^6/s (evaluated from fits in Figure 25a and Figure 21), $\tau_{SRH} = 5.4$ ns (the longest reported carrier lifetime for InN[228]), and Hall-measured initial background electron concentration $N_e^{\phi=0}$, resulting in a

good fit to the experimental data (see opaque lines for calculated curves and circles for experimental data in Figure 26). With this simple model corroborated, the degradation rate for a hypothetical zero-electron-density InN layer is predicted (see opaque line for $N_e^{\phi=0} = 0$ in Figure 26): the corresponding damage threshold is by an order of magnitude lower than that in the studied InN samples. Nevertheless, the predicted threshold still exceeds those in the compared semiconductors, thus reaffirming the high radiation resistance in InN.[l] This conclusion is also supported by a study on radiation resistance in high quality ($N_e^{\phi=0}$ = 7×10^{17} cm^{-3}) MBE-grown InN epilayer.[274] The PL intensity values reported therein endure 2 MeV proton irradiation at fluences corresponding to $D_\mathrm{d} \approx 2\times10^{12} \div 1\times10^{13}$ MeV/g and do not violate now-estimated lower limit of radiation resistance (data does not fall below the $N_e^{\phi=0} = 0$ degradation curve). Such remarkable radiation hardness in InN may be attributed to the absence of mid-gap irradiation-induced defects contributing to SRH recombination.[274]

To evaluate the radiation resistance in InN under the conditions encountered in space, one can estimate the upper limit of solar proton damage dose ($D_\mathrm{d}^{1\mathrm{yr}}$) accumulated in InN in a year-long space mission. Such prediction is made by integrating the product of the cumulative[m] solar proton fluence spectrum[254] and the energy-dependent NIEL function.[256] The estimated $D_\mathrm{d}^{1\mathrm{yr}}$ is equal to ~5×10^9 MeV/g (noted in Figure 26), which is substantially lower than the corresponding τ drop-off threshold, demonstrating that the proton irradiation expected in space should not affect carrier dynamics in InN for decades. This outstanding result highlights the potential of InN-based devices for applications in the most severe radiation environments, such as those encountered in the Jovian magnetosphere, during exceptional solar particle events and exoatmospheric nuclear detonations.

[l] This conclusion holds (compared to rad-resistance in GaAs-based semiconductors) even with the presumed τ_{SRH} lifetime in InN being equal to 1 ms — the value far exceeding that in typical GaAs samples.[277]

[m] The spectrum is predicted for the following conditions: proton energy range – 1 ÷ 300 MeV; environment and distance from Sun – interplanetary space at 1 astronomical unit; mission duration – 1 solar active year; confidence level – 95%, i.e., there's a 5% probability that the predicted cumulative fluence will be exceeded in real-world conditions.

Highlights

- Carrier recombination and minority hole diffusion were studied in InN epilayers irradiated with 1.4-MeV protons, replicating spacelike radiation environment
- At high irradiation levels (corresponding to high free electron concentrations) carrier lifetime is governed by direct Auger recombination described with the same coefficient, $C = 8\times10^{-29}$ cm^6/s, as that for as-grown InN
- Similarly to as-grown InN case, irradiated epilayers feature rapid increase in hole diffusion coefficient with increasing electron density (and proton fluence), reaching D values as high as 190 cm^2/s
- Carrier diffusion length varies insignificantly with proton irradiation and does not decrease below ~140 nm; additionally, L exceeds light absorption depth and thus would be sufficient for carrier extraction in InN-based PV devices even in the most severe radiation environments
- Displacement damage dose required for carrier lifetime deterioration in InN exceeds that in the most rad-hard semiconductors and corresponds to the radiation dose received in a decades-long space mission

Key finding E

- In proton-irradiated u-InN, displacement damage dose required for carrier lifetime deterioration exceeds that in the most radiation-resistant semiconductors; such rad-resistance originates from relatively small impact of radiation-induced defects limited to that of an electron source to the Auger process

Research opportunities

- Study on carrier dynamics in proton-irradiated p-InN, nonpolar InN, nanowire-InN, or in InN comprising all of these cases

Santrauka

Įvadas

Šiuo metu neorganinių kristalinių struktūrų duomenų bazėje yra užregistruota daugiau nei 3000 unikalių nitridinių junginių,[1,2] iš kurių trys – InN, GaN, AlN ir jų trinariai bei keturnariai analogai – yra susilaukę ženklaus tyrinėtojų dėmesio. Pagrindinė pastarųjų nitridų patrauklumo priežastis yra siejama su galimybe derinti jų draustinių energijų tarpą itin plačiame energijų intervale: pradedant IR diapazonu (nuo 0.65 eV InN junginyje) ir ištisu matomo spektro ruožu (InGaN junginiuose), ir baigiant UV sritimi (iki 6 eV AlN junginyje). Ši savybė leidžia III grupės nitridams vyrauti daugybėje taikymų, pvz.: AlGaN sistema vaidina kertinį vaidmenį UV srities optoelektronikoje; GaN palaipsniui tampa neatsiejama galios elektronikos dalimi, lenkiančia Si technologiją tokiais parametrais kaip našumas, maksimali darbinė įtampa/dažnis bei atsparumas įvairiems aplinkos faktoriams (aukštoms temperatūroms, apšvitinimo lygiams ir t.t.); tuo tarpu InGaN jau kurį laiką dominuoja puslaidininkinio apšvietimo rinkoje, orientuotoje į faktiškai nedegraduojančius šviestukus matomos spinduliuotės ruože.

Nepaisant išskirtinių nitridų savybių, puoselėtų dešimtmečius, ir gausos taikymų, siekiančių milijonus vartotojų, nitridų vardas iki šiol buvo žinomas tik industriniame ir akademiniame lygyje, priešingai nei silicio. Laimei, šiais metais galio nitridas buvo pagaliau pastebėtas žiniasklaidos milžinų, tokių kaip *The Verge*, ir buvo pramintas ateities siliciu.[3] Tuo tarpu elektronikos kompanijoms, tokioms kaip *Anker*, GaN vardas tapo įvaizdžio ir reklaminio turinio dalimi, garsinančia ypač mažus ir galingus GaN pagrindo įkroviklius bei išorines baterijas, skirtas kasdieniams mobiliesiems prietaisams.[4] Vis dėlto šis nitridų viešumo proveržis žymi ne tik pozityvų jų atpažinimą, bet ir ženklią medžiagos brandą, tam tikrų tyrimų stagnaciją bei vykstančius/artėjančius pokyčius ateities studijose.

Tradicinių III grupės nitridų technologinės brandos lygis neseniai buvo įvertintas Tsao ir kt. tyrėjų[5] remiantis šiais parametrais: (i) legiravimo technologijos išsivystymu; (ii) padėklų dydžiu/prieinamumu; ir (iii) gamybos apimtimi/kaina, kurią lemia rinkos dydis. Pagal šią klasifikaciją GaN junginys, tam tikros sudėties AlGaN (akcentuojami aliuminiu skurdūs junginiai) ir InGaN (skirti mėlyniems bei žaliems šviestukams) yra laikomi brandžiais puslaidininkiais, tuo tarpu aliuminiu turtingi AlGaN junginiai, AlN, didelės In dalies InGaN junginiai bei InN yra nebrandūs.

Brandžios medžiagų sistemos atveju didžioji dalis bazinių medžiagos savybių yra jau ištirta, o medžiagų auginimo optimizavimas ir prietaisų dizaino tobulinimas yra perduotas industriniam sektoriui. Akademinis sektorius tuo tarpu tolsta nuo rutininiu medžiagų charakterizavimu grįstų tyrimų ir krypsta link novatoriškų taikymų paieškų, dažnai apjungiančių kelias disciplinas. Tokios paieškos apima GaN mikroprocesorių[6] ir neutronų detektorių[7] atšiaurioms kosminėms aplinkoms vystymą; nitridinių paviršių ir sandūrų, jungiančių sintetines medžiagas ir biologinius objektus, nagrinėjimą;[8,9] GaN fotocheminių diodų, skirtų vandens molekulių skaidymui, vystymą;[10] kambario temperatūroje vykstančios vienfotonės emisijos realizavimą pasitelkiant nitridinių junginių defektus;[11] ar stebinančių savybių, tokių kaip deimantui prilyginamo atsparumo mechaniniam poveikiui, atradimą.[12]

Technologiškai nebrandžių nitridinių junginių (tokių kaip InN ar aliuminiu turtingų AlGaN junginių) atveju žinios apie bazines medžiagos savybes (tokias kaip krūvininkų dinamikos ypatybės) yra tik paviršinio lygio, o šių savybių tyrimai – tik ankstyvojoje stadijoje ir sąlyginai reti. Ši tyrimų stoka, sąlygojanti vienas kitam prieštaraujančių rezultatų gausą, yra nulemta daugelio persipynusių veiksnių: sudėtingo minėtųjų medžiagų auginimo, žemos bandinių kokybės, komplikuotų eksperimentų IR ir UV-C spinduliuotės srityse ir proveržį skatinančių prietaisų, atradimų ar tiesiog susidomėjimo stygiaus. Nepaisant šių trūkumų, mažiau brandūs nitridiniai junginiai išlieka be galo vertingais tyrimų objektais, galimai slepiančiais unikalias savybes šiuo metu esančiose charakterizavimo spragose.

Tikslas ir naujumas

Ši disertacija yra sudaryta iš grupės individualių tyrimų, nagrinėjančių krūvininkų dinamikos savybes įvairiuose III-N junginiuose (konkrečiau – AlGaN, GaN ir InN), besiskiriančiuose tiek sudėtimi, tiek technologinės brandos lygiu. Tiriant skirtingo technologinio išsivystymo medžiagas darbui suformuluotas dvejopas tikslas:

> Nebrandžių nitridinių junginių atveju siekiama užpildyti tuščias spragas baziniame krūvininkų rekombinacijos ir difuzijos charakterizavime; tuo tarpu brandžių junginių atveju siekiama apibūdinti sunkiau aptinkamus ir rečiau nagrinėjamus reiškinius, tokius kaip rekombinacija skatintos defektų reakcijos ar sandūrinė rekombinacija, bei įvertinti šių reiškinių vaidmenį esamuose taikymuose.

Iš viso darbe yra pateikti penki unikalūs tyrimai, sprendžiantys penkis individualiai reikšmingus uždavinius.

Pirmasis tyrimas (skyrius A; paremtas straipsniu A) nagrinėja krūvininkų rekombinacijos savybes tiek aliuminiu skurdžiuose, tiek turtinguose AlGaN sluoksniuose, ir apibūdina juose vykstančių spindulinių bei nespindulinių procesų evoliuciją keičiantis nepusiausviryjų krūvininkų tankiui. Remiantis dvejomis metodikomis – laikinės skyros dinaminių difrakcinių gardelių (DDG) ir laike integruotos fotoliuminescencinės spektroskopijos (FL) – nustatomi iki šiol nežinoti spindulinės rekombinacijos koeficientai. Nors tokio pobūdžio charakterizavimas nebūtų itin ypatingas InGaN junginių atveju, jis yra gan unikalus AlGaN tyrimų erdvėje, stokojančioje išsamaus krūvininkų dinamikos savybių aprašymo.

Antrasis tyrimas (skyrius B; paremtas straipsniu B) nagrinėja retai akcentuojamą rekombinacija skatintos defektų reakcijos reiškinį (angl. Recombination-enhanced defect reactions, REDR) AlGaN junginiuose. REDR efektą galima būtų apibūdinti kaip tam tikrą neterminio defektų atkaitinimo formą, aktyvuojamą nespindulinės nepusiausviryjų krūvininkų rekombinacijos esant ypač aukštiems krūvininkų tankiams. Šiame darbe tiriamuose AlGaN sluoksniuose tokie aukšti krūvininkų tankiai pasiekiami sluoksnius *fotomodifikuojant,* t.y., apšviečiant intensyvia lazerine spinduliuote.

Istoriškai, REDR efektas buvo stebėtas faktiškai visuose technologiškai svarbiuose puslaidininkiuose, ir buvo kaltinamas dėl daugybės prietaisų degradacijos. Nitridiniuose junginiuose REDR reiškinys buvo identifikuotas tik kelis kartus, ir buvo susietas su nespindulinės rekombinacijos centrų generacija. Šiame tyrime yra siekiama rasti fotomodifikuojamos medžiagos parametrus, kontroliuojančius REDR indukuotų rekombinacijos centrų prieauglį, ir lemiančius junginio jautrumą fotomodifikacijai. Papildomai, tyrime yra nagrinėjama fotomodifikacijos įtaka krūvininkų difuzijai, ir yra atskleidžiamas netikėtas rezultatas – krūvininkų difuzijos koeficiento ir difuzijos ilgio padidėjimas fotomodifikuotuose bandiniuose.

Trečiasis tyrimas (skyrius C; nepublikuota) nagrinėja krūvininkų dinamikos procesus įprastose AlGaN/GaN heterosandūrose. Tokiose heterostruktūrose padėklas ar apatinis sluoksnis turėtų riboti viršutinių sluoksnių kokybę ir lemti ištiso prietaiso veikimą, tuo tarpu viršutinis sluoksnis turėtų pasyvuoti po juo esantįjį ir sumažinti sandūrinės rekombinacijos greitį. Vis dėlto, šiame tyrime yra stebima neįprasta atvirkštinė tendencija: viršutinio AlGaN barjero indukuota sandūros kokybės

degradacija ir nespindulinės rekombinacijos spartos augimas apatiniame GaN buferyje. Tyrimas atskleidžia sandūrinę rekombinaciją esant vienu svarbiausių krūvininkų žūties mechanizmų, tam tikrais atvejais ribojančiu prietaiso našumą. Šie rezultatai išryškina netikėtai žalingą pasyvių elementų įtaką nitridiniuose prietaisuose, ir akcentuoja, kad pastarieji elementai neturėtų būti ignoruojami tolesniame prietaisų vystyme.

Ketvirtasis tyrimas (skyrius D; paremtas straipsniu D) nagrinėja bazines krūvininkų rekombinacijos ir difuzijos savybes MOCVD (angl. metalorganic chemical vapor deposition) ir MBE (angl. molecular beam epitaxy) būdais užaugintuose InN sluoksniuose su skirtingomis pusiausvirųjų elektronų koncentracijomis. Krūvininkų rekombinacijos atveju darbas patikimai nustato dominuojantį (ir mokslinę bendruomenę polemizuojantį) rekombinacijos mechanizmą. Krūvininkų difuzijos atveju tyrimas atskleidžia nepaprastai aukštus šalutinių skylių difuzijos koeficientus iki šiol nenagrinėtame krūvininkų tankių diapazone. Remiantis šiais duomenimis tyrimas įvertina MOCVD būdu augintų InN junginių panaudojimo galimybes fotoelektriniuose prietaisuose. Lyginant su kitais darbais šis tyrimas išsiskiria didele bandinių imtimi ir pritaikytu femtosekundinės skyros DDG metodu, leidžiančiu stebėti šalutinių krūvininkų dinamikos procesus, nepasiekiamus tipiniais šios tyrimų srities eksperimentais.

Penktasis tyrimas (skyrius E; paremtas straipsniu E) nagrinėja ypatingai didelių įtėkių protonų apšvitinimo (energetiškai analogiško natūraliai kosminei spinduliuotei) įtaką krūvininkų dinamikai InN junginiuose, įvertina InN atsparumą apšvitinimui, ir palygina šį įvertį su kitų puslaidininkių atsparumais bei su apšvitinimo doze, akumuliuojama dešimtmečius trunkančioje kosminėje misijoje.

Dabartinių kosminių misijų trukmė pačiose atšiauriausiose radiacinėse aplinkose yra stipriai ribojama fotoelektrinių prietaisų, grįstų tradiciniais apšvitinimui neatspariais puslaidininkiais. Dėl pastarosios priežasties ir dėl šiuo metu atgimstančių kosmoso tyrinėjimų, vystomų tiek valstybinio, tiek komercinio sektorių iniciatyva, apšvitinimui atsparių puslaidininkių poreikis sparčiai auga. Šio poreikio įkvėptas yra ir penktasis tyrimas, atskleidžiantis InN junginį kaip nepaprastai atsparų kosminei spinduliuotei puslaidininkį.

Teiginys A: AlGaN junginiuose nepusiausvirųjų krūvininkų tankiui esant mažesniam už $\sim 10^{19}\,\mathrm{cm}^{-3}$ vidinis kvantinis našumas didėja tiek kylant krūvininkų tankiui, tiek Al daliai dėl spartėjančios spindulinės krūvininkų rekombinacijos; priešingame krūvininkų tankių sparne stebimas našumo krytis, indukuojamas nespindulinio kanalo spartėjimo (valdomo krūvininkų tankio prieaugiu) ir spindulinio kanalo gesimo (valdomo fazinės erdvės pildymu)

Teiginys B: $Al_xGa_{1-x}N$ junginių ($x \approx 0.2 \div 0.7$) fotomodifikacija ties itin aukštu krūvininkų tankiu ($6\times10^{19} \div 3.7\times10^{20}\ \mathrm{cm}^{-3}$), fotogeneruotu intensyvia impulsine lazerine spinduliuote, gali paspartinti nespindulinę krūvininkų rekombinaciją ir difuziją; šių pokyčių amplitudė priklauso nuo fotomodifikacijos impulsų skaičiaus, fotogeneruoto krūvininkų tankio ir Al dalies AlGaN junginyje

Teiginys C: AlGaN/GaN heterosandūros viršutiniame AlGaN barjere esantys defektai turi įtakos apatinio GaN sluoksnio krūvininkų dinamikos savybėms: defektams bloginant barjero kokybę sandūrinės rekombinacijos greitis didėja, o sandūrinės rekombinacijos mechanizmas tampa dominuojančiu

Teiginys D: Krūvininkų dinamikos savybės u-InN junginiuose yra stipriai susietos su suminiu elektronų tankiu (atitinkančiu pusiausviruosius ir nepusiausviruosius elektronus): elektronų tankiui viršijus $\sim 5\times10^{18}\,\mathrm{cm}^{-3}$, difuzijos koeficientas didėja sparčiau nei tiesiškai, o krūvininkų gyvavimo trukmė mažėja; pastarasis mažėjimas yra kontroliuojamas tiesioginės Ožė rekombinacijos ir fazinės erdvės pildymo efektų

Teiginys E: u-InN junginių atsparumas apšvitinimui protonais (vertinamas krūvininkų gyvavimo trukmės pokyčiu) viršija daugumos analogiškų puslaidininkinių; to priežastis yra sąlyginai maža apšvitinimo indukuotų defektų įtaka krūvininkų rekombinacijos procesams: pastarieji defektai tėra elektronų šaltinis Ožė rekombinacijos kanalui

Eksperimentų aprašas

Bandiniai

Šiame darbe tirti AlGaN ir InN bandiniai bus identifikuojami pasitelkiant kelis paprastus parametrus: Al molinę dalį junginyje (x), krūvininkų lokalizacijos gylį (σ), t.y., būsenų tankio (juostos krašte), aprašomo Gausiniu pasiskirstymu, standartinį nuokrypį, ir pusiausvirųjų krūvininkų koncentraciją (N_e). Šie parametrai ir kitos bandinių savybės, tokios kaip sluoksnio storis ar buferio būvis (yra/nėra), bei kelios auginimo detalės yra pateiktos lentelėse 1 ir 2, atitinkamai skirtose AlGaN ir InN bandiniams.

$Al_xGa_{1-x}N/GaN$ heterosandūros buvo užaugintos ant c plokštumos safyro padėklų MOCVD būdu. 130 – 300 nm storio $Al_xGa_{1-x}N$ barjerai buvo užauginti esant tai pačiai temperatūrai (1090 °C) ir tam pačiam tri-metil-aliuminio (TMAl) dujų srautui (1.21×10^{-5} mol/min); barjero Al molinė dalis buvo keičiama varijuojant tri-metil-galio (TMGa) srautą (nurodyta lentelėje 1). Siekiant užauginti skirtingos struktūrinės kokybės barjerus buvo varijuojamas ir amoniako srautas. Tokiu būdu buvo gauti trys bandinių rinkiniai, išsiskiriantys tiek bandinių kokybe (rinkinio viduje), tiek vidutine Al koncentracija (tarp rinkinių), siekiančia $\bar{x}$ = (0.13, 0.2 ir 0.34); santykinis x nuokrypis rinkinyje – $\lesssim$10%. Priešingai barjerų atvejui, 4 µm storio GaN buferių auginimo sąlygos nebuvo varijuojamos: temperatūra buvo lygi T = 1080 °C, TMGa srautas – 1.77×10^{-4} mol/min, o NH_3 srautas – 0.232 mol/min. Visi aptarti $Al_xGa_{1-x}N/GaN$ bandiniai buvo pasitelkti tiriant krūvininkų dinamikos savybes AlGaN/GaN sandūrose (skyrius C); keli AlGaN barjerai taip pat buvo panaudoti tiriant krūvininkų rekombinacijos savybes (skyrius A) ir fotomodifikacijos reiškinį (skyrius B) AlGaN junginiuose.

700 nm storio **$Al_{0.46}Ga_{0.54}N$** sluoksnis buvo užaugintas ant c plokštumos AlN/safyro šablono MOCVD būdu ties T = 1090 °C temperatūra ir 3.23×10^{-5} mol/min TMAl srautu. Šis bandinys buvo pasitelktas tiriant fotomodifikacijos reiškinį AlGaN junginiuose (skyrius B).

Likę ~1 µm storio **Al turtingi ($x \geq 0.48$) $Al_xGa_{1-x}N$ sluoksniai** buvo užauginti MEMOCVD būdu (angl. migration-enhanced metalorganic chemical vapor deposition) ant c plokštumos AlN/safyro šablonų. Šie bandiniai buvo pasitelkti tiriant krūvininkų rekombinacijos savybes (skyrius A) ir fotomodifikacijos reiškinį (skyrius B) AlGaN junginiuose.

Lentelė 1. Disertacijoje tirtų AlGaN sluoksnių/barjerų elektriniai parametrai ir auginimo detalės.

Bandinys	***σ*** **(meV)**	**Auginimo metodas**	**TMGa (mol/min)**	**NH_3 (mol/min)**
$Al_{0.11}Ga_{0.89}N/GaN$		MOCVD	1.25×10^{-4}	0.223
$Al_{0.12}Ga_{0.88}N/GaN$		MOCVD	1.25×10^{-4}	0.179
$Al_{0.13}Ga_{0.87}N/GaN$		MOCVD	1.25×10^{-4}	0.134
$Al_{0.14}Ga_{0.86}N/GaN$	13	MOCVD	1.25×10^{-4}	0.089
$Al_{0.19}Ga_{0.81}N/GaN$		MOCVD	7.76×10^{-5}	0.112
$Al_{0.20}Ga_{0.80}N/GaN$	21	MOCVD	7.76×10^{-5}	0.089
$Al_{0.21}Ga_{0.79}N/GaN$		MOCVD	7.76×10^{-5}	0.067
$Al_{0.32}Ga_{0.68}N/GaN$		MOCVD	3.84×10^{-5}	0.112
$Al_{0.33}Ga_{0.67}N/GaN$	30	MOCVD	3.84×10^{-5}	0.089
$Al_{0.34}Ga_{0.66}N/GaN$		MOCVD	3.84×10^{-5}	0.067
$Al_{0.35}Ga_{0.65}N/GaN$		MOCVD	3.84×10^{-5}	0.045
$Al_{0.38}Ga_{0.62}N/GaN$		MOCVD	3.84×10^{-5}	0.022
$Al_{0.46}Ga_{0.54}N$		MOCVD	6.65×10^{-5}	0.179
$Al_{0.48}Ga_{0.52}N$	45	MEMOCVD		
$Al_{0.60}Ga_{0.40}N$	48	MEMOCVD		
$Al_{0.60}Ga_{0.40}N$	57	MEMOCVD		
$Al_{0.60}Ga_{0.40}N$	60	MEMOCVD		
$Al_{0.60}Ga_{0.40}N$	60	MEMOCVD		
$Al_{0.64}Ga_{0.36}N$	34	MEMOCVD		
$Al_{0.65}Ga_{0.35}N$	50	MEMOCVD		
$Al_{0.68}Ga_{0.32}N$	65	MEMOCVD		
$Al_{0.71}Ga_{0.29}N$	50	MEMOCVD		

Ploni (30 – 400 nm) **InN** sluoksniai (sudarantys 21 bandinio rinkinį; žr. lentelę 2) buvo užauginti MOCVD būdu ant c plokštumos GaN/safyro šablonų arba tiesiogiai ant safyro padėklų. Sluoksniai buvo auginami ties pastovia arba auginimo metu tolygiai keliama temperatūra (570 – 630 °C intervale). Prekursorių tiekimas buvo pasirinktinai nuolatinis arba impulsinis. Kaip yra įprasta InN junginiams, tikslingai nelegiruotų sluoksnių laidumas buvo n tipo (plačiau apie tai – *Box D. Control of background electron concentration* intarpe); pusiausvirųjų elektronų koncentracija juose siekė nuo 6×10^{18} cm^{-3} iki 5×10^{19} cm^{-3} (įvertinta Holo metodu). Visi pastarieji bandiniai buvo pasitelkti tiriant krūvininkų dinamikos savybes InN sluoksniuose (skyrius D). Analizuojant protonų apšvitinimo įtaką krūvininkų dinamikos savybėms (skyrius E) iš pastarojo bandinių rinkinio buvo pasitelkti trys sluoksniai (**S1, S2 ir S3;** įvardinti lentelėje 2), besiskiriantys struktūrine kokybe ir pusiausvirųjų elektronų koncentracija.

Lentelė 2. Disertacijoje tirtų InN sluoksnių elektriniai parametrai ir auginimo detalės.

#	N_e (cm^{-3})	Storis (nm)	Buferis	Metodas	Prekurs. tiekimas	Aug. *T*
	5.1×10^{19}	300	✓	MOCVD	impulsinis	pastovi
	4.7×10^{19}	300	✓	MOCVD	impulsinis	pastovi
	4.7×10^{19}	300	✓	MOCVD	impulsinis	pastovi
	4.5×10^{19}	300	✓	MOCVD	impulsinis	pastovi
	4.4×10^{19}	300	✓	MOCVD	impulsinis	pastovi
	4.2×10^{19}	300	✓	MOCVD	impulsinis	pastovi
	3.5×10^{19}	26	✓	MOCVD	impulsinis	kylanti
S2	$(3.4/5.9)\times10^{19}$	300	✓	MOCVD	impulsinis	pastovi
	3.1×10^{19}	300	✓	MOCVD	impulsinis	pastovi
	3.0×10^{19}	79	✓	MOCVD	impulsinis	kylanti
	2.3×10^{19}	300	✓	MOCVD	impulsinis	pastovi
	2.3×10^{19}	300	✓	MOCVD	impulsinis	pastovi
	1.5×10^{19}	158	✓	MOCVD	impulsinis	kylanti
S3	$(1.3/1.9)\times10^{19}$	390	×	MOCVD	nuolatinis	pastovi
	1.1×10^{19}	326	✓	MOCVD	nuolatinis	kylanti
	9.0×10^{18}	300	✓	MOCVD	impulsinis	kylanti
	8.8×10^{18}	236	✓	MOCVD	impulsinis	kylanti
S1	$(8.0/13)\times10^{18}$	300	✓	MOCVD	impulsinis	kylanti
	6.8×10^{18}	315	✓	MOCVD	impulsinis	kylanti
	6.8×10^{18}	315	✓	MOCVD	impulsinis	kylanti
	6.2×10^{18}	394	✓	MOCVD	impulsinis	kylanti
	1.4×10^{18}	2300	✓	MBE		

Storiausias (2.3 µm) ir aukščiausios kokybės ($N_e = 1.4\times10^{18}$ cm^{-3}) disertacijoje tirtas InN sluoksnis buvo užaugintas RF-PAMBE būdu (angl. radio frequency plasma-assisted MBE) ant c plokštumos safyro padėklo. Šis bandinys buvo pasitelktas krūvininkų dinamikos savybių tyrime (skyrius D).

Metodai

Didžioji dalis disertacijoje atliktų eksperimentų yra paremti bekontakčiais optiniais metodais: fotoliuminescencinės spektroskopijos (kvazinuostoviųjų sąlygų bei laikinės skyros) ir dinaminių difrakcinių gardelių.

Kvazinuostoviųjų sąlygų fotoliuminescencinės spektroskopijos metodika buvo pritaikyta tiriant fotomodifikacijos reiškinį (skyrius B), bei vertinant vidinį kvantinį našumą (skyrius A) ir krūvininkų lokalizacijos gylį (skyriai A ir B; σ vertės pateiktos lentelėje 1) AlGaN junginiuose.

Lokalizacijos gylio parametras buvo nustatytas iš FL spektro smailės temperatūrinės priklausomybės remiantis Eliseev modeliu[103] (detalus metodo aprašymas pateiktas *Quasi-stationary photoluminescence spectroscopy* skyriuje). Bandinių žadinimui buvo panaudotas impulsinis (impulso trukmė – 4 ns) YAG:Nd lazeris (*Ekspla*), veikiantis 10 Hz dažniu. Žadinimo bangos ilgis buvo pasirinktas atsižvelgiant į Al molinę dalį AlGaN sluoksniuose: $x \leq 0.33$ Al dalies junginiai buvo žadinami 266 nm spinduliuote (IV lazerio harmonika), tuo tarpu $x \geq 0.48$ atitinkantys junginiai – 213 nm spinduliuote (V harmonika).

Laikinės skyros fotoliuminescencinės spektroskopijos metodas buvo pritaikytas tiriant krūvininkų rekombinacijos savybes AlGaN/GaN sandūroje. Bandinių žadinimui buvo panaudotas trumpų impulsų (impulso trukmė – 25 ps) YAG:Nd lazeris (*Ekspla*), veikiantis 10 Hz dažniu. Selektyviam barjero/buferio žadinimui buvo pasitelkta 266/355 nm spinduliuotė. Skirtingo bangos ilgio impulsai taip pat buvo pasitelkti buferio žadinimo gyliui keisti. Šių matavimų rezultatai yra pateikti išskirtinai *Chapter C: Carrier dynamics in AlGaN/GaN interface* skyriuje.

Šviesa indukuotų dinaminių difrakcinių gardelių metodas buvo pritaikytas tiriant krūvininkų dinamikos procesus tiek InN, tiek GaN ir AlGaN junginiuose. Šie eksperimentai sudaro didžiausią darbe atliktų matavimų dalį, o jų rezultatai formuoja kiekvieno disertacijos skyriaus pamatą.

DDG eksperimentas yra pagrįstas dviejų koherentinių žadinimo pluoštelių, susikertančių kampu Θ ties bandinio paviršiumi, interferencija, indukuojančia nepusiausvirųjų krūvininkų tankio erdvinę moduliaciją periodu $\Lambda = \lambda/(2\sin\Theta/2)$, kur λ yra žadinančiojo pluoštelio bangos ilgis. Ši krūvininkų tankio moduliacija sąlygoja medžiagos lūžio rodiklio moduliaciją, kurios amplitudė yra proporcinga nepusiausvirųjų krūvininkų tankiui (ΔN). Pastaroji lūžio rodiklio moduliacija atitinka dinaminę difrakcinę gardelę, yrančią dėl dviejų procesų: krūvininkų rekombinacijos ir difuzijos. Eksperimento metu dinaminės difrakcinės gardelės irimas yra stebimas detektuojant trečiojo, zonduojančio pluoštelio – vėlinamo ir nesugeriamo medžiagoje – difragavusią komponentę.

Dinaminės gardelės irimo trukmė (τ_G) yra įvertinama remiantis funkcija $\eta \propto \exp(-2t/\tau_G)$, kur η yra difrakcijos efektyvumas – difragavusios ir praėjusios zonduojančio pluoštelio komponenčių [intensyvumų] santykis. Nepusiausvirųjų krūvininkų rekombinacijos trukmė (τ) ir ambipolinis difuzijos koeficientas (D) yra nustatomi remiantis lygtimi $1/\tau_G = 1/\tau + 4\pi^2 D/\Lambda^2$, kur τ_G yra gardelės periodo Λ funkcija. Išsamus (bei

iliustruotas) krūvininkų dinamikos parametrų τ ir D nustatymo DDG metodu aprašas ir kiti DDG eksperimento ypatumai yra pateikti *Light-induced transient gratings* skyriuje.

AlGaN ir GaN bandinių žadinimui buvo panaudotas trumpų impulsų (impulso trukmė – 25 ps) YAG:Nd lazeris (*Ekspla*), veikiantis 10 Hz dažniu. GaN buferių AlGaN/GaN heterostruktūrose žadinimui buvo pasitelkta III lazerio harmonika (atitinkanti 355 nm bangos ilgio impulsus), AlGaN sluoksnių su Al kiekiu $x \leq 0.38$ žadinimui – IV harmonika (266 nm), o sluoksnių su $x \geq 0.46$ žadinimui – V harmonika (213 nm). Fotomodifikacijos reiškinio tyrime visi bandiniai buvo žadinti V lazerio harmonika nepaisant junginių sudėties. Bandinių zondavimui buvo pasitelkta I harmonika (1064 nm).

InN bandinių žadinimui buvo panaudotas ultratrumpų impulsų (impulso trukmė – 250 fs) *Pharos* lazeris (*Šviesos konversija*), veikiantis 30 kHz dažniu. I lazerio harmonika (1030 nm) buvo pasitelkta žadinti tiek bandinius, tiek *Orpheus* optinį parametrinį stiprintuvą (*Šviesos konversija*), tuo tarpu pastarojo stiprintuvo generuojama 2400 nm bangos ilgio spinduliuotė atliko zonduojančio pluoštelio vaidmenį. Detalus AlGaN/GaN ir InN bandiniams skirtų DDG eksperimento sistemų techninis aprašas yra pateiktas *Light-induced transient gratings* skyriuje.

Skyrius A: Krūvininkų rekombinacija AlGaN junginiuose

Šiame skyriuje yra nagrinėjami spinduliniai ir nespinduliai rekombinacijos procesai plačiame krūvininkų tankių diapazone įvairios sudėties AlGaN sluoksniuose. Vertingiausias tyrimo rezultatas – iki šiol nežinotų bimolekulinės rekombinacijos koeficiento (B) verčių atskleidimas ir prigimties aprašymas. Šis rezultatas yra pasiektas apjungiant DDG ir kvazinuostoviųjų sąlygų FL eksperimentus, taip išvengiant duomenų neapibrėžtumo ir dviprasmiškumo.

DDG metodu įvertintų bimolekulinės rekombinacijos koeficiento ir Šoklio-Rydo-Holo (SRH) nespindulinės rekombinacijos trukmės (τ_{SRH}; detali įvertinimo procedūra aprašyta *Evaluation of recombination coefficients* skyriuje) priklausomybės nuo $Al_xGa_{1-x}N$ sluoksnių sudėties yra pateiktos Pav. 1: tiek SRH, tiek bimolekulinės rekombinacijos sparta auga didėjant Al molinei daliai, x, junginyje.

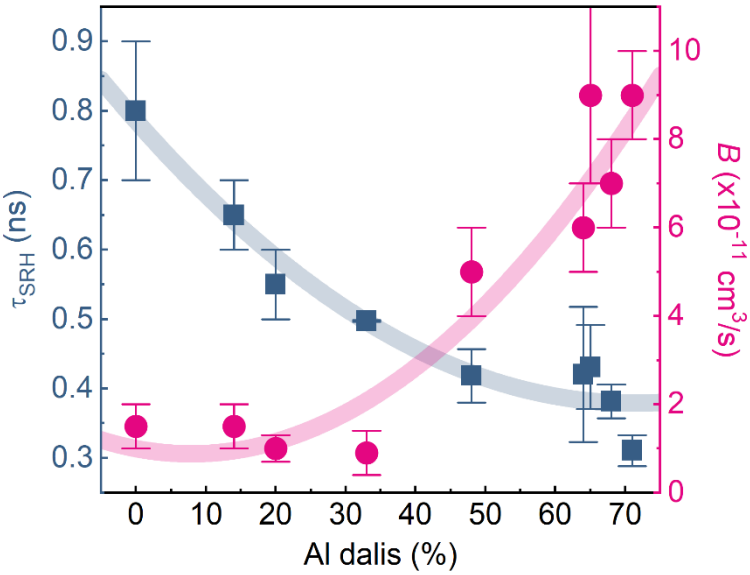

Pav. 1 Nespindulinės rekombinacijos trukmės τ_{SRH} (mėlyni stačiakampiai) ir bimolekulinės rekombinacijos koeficiento B (rausvi apskritimai) priklausomybės nuo Al molinės dallies AlGaN junginiuose. *Adaptuota pagal straipsnį A.*

SRH rekombinacijos atveju, τ_{SRH} trukmės mažėjimą nuo ~0.8 iki 0.4 ns (Al daliai augant $x = 0 \div 0.7$ intervale) galima apibūdinti dvejomis tendencijomis: staigiu kritimu mažų Al kiekių srityje ($x < 0.3$), ir įsisotinimu didelių x diapazone. Šių tendencijų buvimą lemia skirtingas krūvininkų lokalizacijos laipsnis: Al skurdžioje srityje τ_{SRH} trukmė apibūdina laisvųjų

krūvininkų rekombinacijos spartą, jautrią defektų (nespindulinės rekombinacijos centrų) koncentracijos pokyčiams; tuo tarpu Al turtingoje srityje τ_{SRH} aprašo lokalizuotų krūvininkų rekombinaciją, silpniau pavaldžią defektų koncentracijos svyravimams. Krūvininkų lokalizacijos gylio σ didėjimas augant Al kiekiui AlGaN junginyje yra matomas lentelėje 1.

Bimolekulinės rekombinacijos atveju, netiesinės rekombinacijos koeficientas B padidėja nuo 1×10^{-11} iki 9×10^{-11} cm^3/s Al koncentracijai x pakilus nuo 0 iki 0.7. DDG metodu nustatytą B koeficientą laikant išskirtinai spindulinės rekombinacijos koeficiento atitikmeniu, lygties $IQE = \frac{BN}{A+BN}$ pagalba galima įvertinti vidinį kvantinį našumą (IQE); čia, $A = 1/\tau_{SRH}$. Šiuo būdu nustatytų IQE verčių priklausomybė nuo AlGaN junginių sudėties ties mažu krūvininkų tankiu ($\Delta N \approx 3\times10^{18}$ cm^{-3}) yra pateikta Pav. 2 (rausvi apskritimai): jame stebimas IQE augimas kylant Al koncentracijai. Panaši tendencija yra gaunama IQE vertes nustatant ir kitokiu – FL metodu (vertės pažymėtos mėlynais stačiakampiais Pav. 2), kuris remiasi IQE prilyginimu FL intensyvumų ties 300 K ir 8 K temperatūromis santykiui (tariama, kad IQE = 100% ties 8 K).

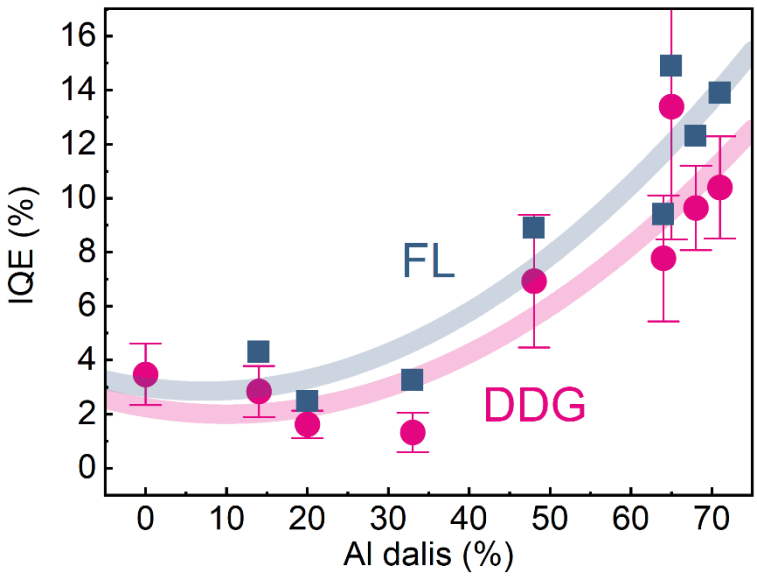

Pav. 2. Vidinio kvantinio našumo ties $\Delta N \approx 3\times10^{18}$ cm^{-3} nepusiausviruųjų krūvininkų tankiu priklausomybė nuo Al koncentracijos AlGaN junginyje. IQE vertės nustatytos FL (mėlyni stačiakampiai) ir DDG (rausvi apskritimai) eksperimentais. *Adaptuota pagal straipsnį A.*

Situacija aukštų krūvininkų tankių srityje yra kitokia: FL ir DDG metodais nustatytų IQE verčių priklausomybės nuo ΔN nebesutampa (žr. Pav. 3). DDG

atveju (rausvi apskritimai), IQE vertės tolygiai didėja kylant ΔN, ir artėja link 100% ribos. FL atveju (mėlyni stačiakampiai), IQE(ΔN) priklausomybė patiria našumo krytį. Atsižvelgiant į tai, kad FL būdu užfiksuota IQE(ΔN) priklausomybė yra pagrįsta tiesioginiu liuminescencijos kryčio stebėjimu, kitokia DDG metodo IQE(ΔN) tendencija verčia abejoti pastarosiomis IQE vertėmis ir joms nustatyti pasitelktais bimolekulinės rekombinacijos koeficientais. Galimai, DDG būdu įvertintas B koeficientas atspindi ne tik spindulinius rekombinacijos procesus, bet ir netiesinius nespindulinius, nežymius mažų krūvininkų tankių srityje, bet itin sparčius ties aukštais ΔN.

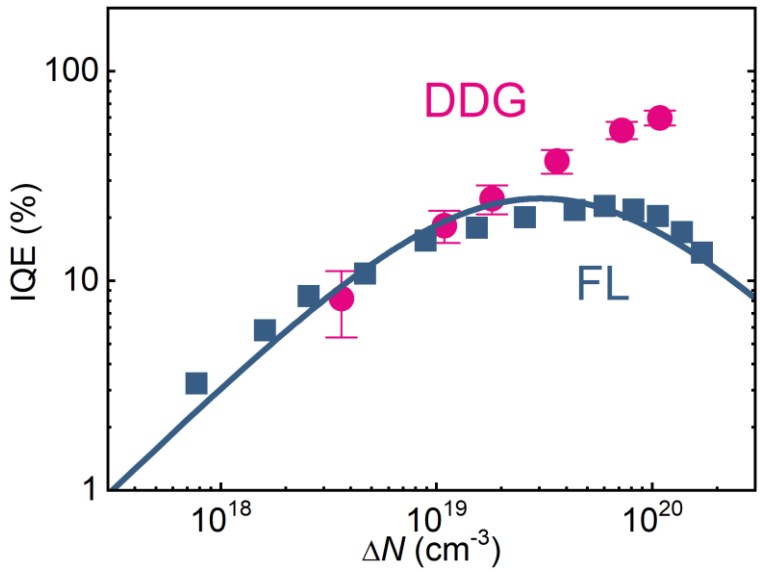

Pav. 3. Vidinio kvantinio našumo, įvertinto FL (mėlyni stačiakampiai) ir DDG (rausvi apskritimai) metodais, priklausomybė nuo nepusiausvirųjų krūvininkų tankio $Al_{0.48}Ga_{0.52}N$ junginyje. Mėlyna kreivė apskaičiuota remiantis išraiška $IQE = B_{rad}(N)N/\{A + [B_{rad}(N) + B_{nr}(N)]N\}$. *Adaptuota pagal straipsnį A.*

Netiesinės rekombinacijos koeficientams B pakoreguoti – juose slypinčių spindulinio ir nespindulinio sandų evoliucijai kintant ΔN apibūdinti – buvo pasitelkta $IQE = \frac{B_{\mathrm{rad}}(N)N}{A+BN}$ išraiška, kuria aprašoma IQE(N) kreivė buvo sutapatinta su FL IQE eksperimentinėmis vertėmis; čia, $B = B_{\mathrm{rad}}(N) + B_{\mathrm{nr}}(N) = const$ – naujoji B koeficiento išraiška, talpinanti spindulinį, $B_{\mathrm{rad}}(N)$, ir nespindulinį, $B_{\mathrm{nr}}(N)$, sandus. $B_{\mathrm{rad}}(N)$ funkcijai aprašyti pasitelkta $B_{\mathrm{rad}}(N) = B_{\mathrm{rad0}}/(1 + N/N^{*})$ išraiška,[124,125] apibūdinanti spindulinės bimolekulinės rekombinacijos virsmą monomolekuline dėl krūvininkų išsigimimo – fazinės erdvės pildymo; čia, B_{rad0} yra pradinis spindulinės rekombinacijos koeficientas, atspindintis B_{rad} ties mažu krūvininkų tankiu, ir

prilygintas Pav. 1 pavaizduotoms B vertėms; N^* yra tapatinimo parametras, aprašantis junginiui būdingą krūvininkų tankį, ties kuriuo $B_{rad} = 0.5B_{rad0}$. Šiame tyrime N^* parametras taip pat vaizduoja ribą, kurią viršijus B_{nr} sandas tampa dominuojančiu. Pavyzdinio $Al_{0.48}Ga_{0.52}N$ bandinio atveju, IQE kryčio kreivė, apskaičiuota remiantis naująja IQE išraiška, atitinka eksperimentinius duomenis geriausiai su $N^* = 3\times10^{19}$ cm^{-3} parametru (žr. mėlyną kreivę ir stačiakampius Pav. 3). N^* vertės likusiems bandiniams (kartu su B_{nr} vertėmis ties aukštu tankiu, $\Delta N = 1\times10^{20}$ cm^{-3}) yra pateiktos Pav. 4.

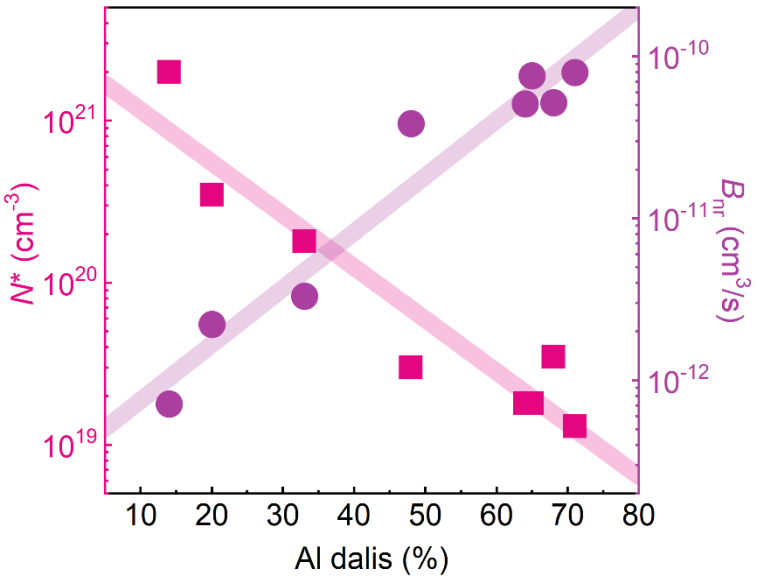

Pav. 4. Charakteringo krūvininkų tankio N^* (rausvi stačiakampiai) ir netiesinės nespindulinės rekombinacijos koeficiento B_{nr} (violetiniai apskritimai) priklausomybės nuo Al koncentracijos AlGaN junginiuose; B_{nr} vertės atitinka $\Delta N = 1\times10^{20}$ cm^{-3} nepusiausvirųjų krūvininkų tankį.

Kaip matyti Pav. 4, N^* krūvininkų tankis mažėja, o B_{nr} koeficientas didėja kylant Al koncentracijai AlGaN junginiuose. Tai reiškia, kad netiesinės nespindulinės rekombinacijos kanalo aktyvavimo slenkstis mažėja, o sparta didėja (ties fiksuotu ΔN), atitinkamai; šias tendencijas galimai lemia *Reduced effective volume* reiškinys,[126] detaliai aprašytas *Recombination trends* skyriuje.

Reziumuojant galima pasakyti, kad netiesinius spindulinės bei nespindulinės rekombinacijos procesus AlGaN junginiuose stipriai lemia junginių sudėtis ir nepusiausvirųjų krūvininkų tankis; šiems procesams aprašyti pakanka DDG ir FL metodais įvertintų B (Pav. 1) ir N^* (Pav. 4) parametrų rinkinio ($\Delta N = 10^{18} \div 10^{20}$ cm^{-3} ir $x = 0 \div 0.7$ diapazonuose).

Skyrius B: AlGaN junginių fotomodifikacija

Šiame skyriuje nagrinėjamos krūvininkų dinamikos savybės fotomodifikuotuose – apšvitintuose itin intensyvia lazerine spinduliuote – AlGaN sluoksniuose. Pastarojo apšvitinimo indukuotiems pokyčiams paaiškinti pasitelkiama REDR efekto (angl. recombination-enhanced defect reactions) interpretacija. REDR – tai atomų migracijos ar defektų transformacijos (difuzijos, disociacijos, generacijos ar anihiliacijos) mechanizmas, aktyvuojamas vibracinės energijos, atpalaiduotos nespindulinės nepusiausvirųjų krūvininkų rekombinacijos metu, pagalba.[129–131] REDR efektas pasireiškia bene visuose technologiškai svarbiuose puslaidininkiuose, o jo padariniai apsunkina daugelio puslaidininkinių prietaisų degradacijos uždavinį. Nepaisant to, nitridinių junginių erdvėje REDR mechanizmo tyrimai yra nepaprastai reti, o pats mechanizmas – neįsisavintas ir nepažabotas.

Šiame tyrime AlGaN sluoksniai buvo fotomodifikuojami kambario temperatūroje pasitelkiant impulsinę (impulso trukmė – 25 ps, dažnis – 10 Hz) 213 nm bangos ilgio lazerio spinduliuotę, bandinyje sugeriamą tarpjuostiniu būdu. Fotomodifikacijos trukmė buvo matuojama impulsų skaičiumi; impulsu generuojamas nepusiausvirųjų krūvininkų tankis (fotomodifikacijos krūvininkų tankis, N_{mod}) buvo kontroliuojamas keičiant spinduliuotės intensyvumą. Fotomodifikacijos įtaka krūvininkų dinamikos savybėms buvo vertinama DDG metodu ties saugiu nepusiausvirųjų krūvininkų tankiu, $N_{DDG} = 3\times10^{19}$ cm^{-3}. Papildomai, bandiniai buvo fotomodifikuojami ilgesniais – 4 ns – impulsais, ir charakterizuojami kvazinuostoviųjų sąlygų FL metodu; šie rezultatai disertacijos santraukoje nėra pateikiami.

Normuoto difrakcijos efektyvumo, η, ir SRH tipo nespindulinės rekombinacijos trukmės, τ_{SRH}, priklausomybės nuo fotomodifikacijos krūvininkų tankio N_{mod} yra pateiktos Pav. 5. Šios priklausomybės nustatytos fotomodifikuojant jautriausią bandinį, $Al_{0.71}Ga_{0.29}N$ (jautrumo tendencijos aprašytos toliau); kiekvienas duomenų taškas atitinka 1600 impulsų trukmės fotomodifikaciją, atliktą prieš tai nemodifikuotame bandinio plotelyje; η efektyvumas buvo vertinamas ties DDG kinetikos piku. Kaip matyti paveiksle, η ir τ_{SRH} parametrai mažėjo didinant N_{mod} panašiomis spartomis (pvz., ties $N_{mod} \approx 3\times10^{20}$ cm^{-3} abu parametrai sumažėjo ~50%). Pastarasis mažėjimas buvo aktyvuotas viršijus tam tikrą N_{mod} slenkstį; $Al_{0.71}Ga_{0.29}N$ bandinyje šis slenkstis buvo lygus $N_{mod} \approx 6\times10^{19}$ cm^{-3}, tuo tarpu kituose bandiniuose – aukštesnis. Koreliacija tarp $\eta(N_{mod})$ ir $\tau_{SRH}(N_{mod})$ tendencijų yra nulemta tiesioginės η priklausomybės nuo τ_{SRH}; ši koreliacija leidžia naudotis

lengvai išmatuojamu η parametru kaip fotomodifikacijos indukuoto nespindulinės rekombinacijos spartos pokyčio rodikliu. Nespindulinės rekombinacijos trukmė, savo ruožtu, mažėjo didinant N_{mod} dėl augančios defektų, generuojamų REDR būdu, koncentracijos.[128]

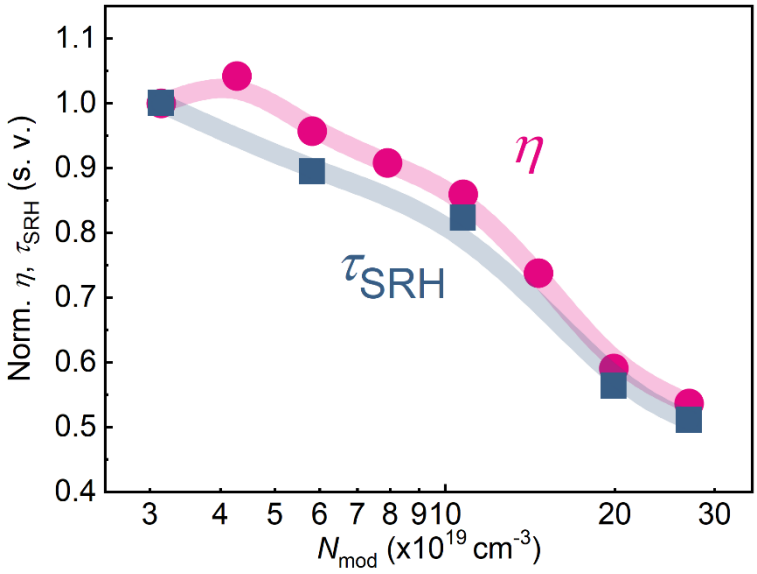

Pav. 5. Normuoto difrakcijos efektyvumo η ir nespindulinės rekombinacijos trukmės τ_{SRH} priklausomybės nuo fotomodifikacijos krūvininkų tankio N_{mod} $Al_{0.71}Ga_{0.29}N$ junginyje, fotomodifikuotame 1600 lazerio impulsais. *Adaptuota pagal straipsnį B.*

Fotomodifikacijos poveikio amplitudę valdantiems parametrams nustatyti buvo fotomodifikuojami įvairių charakteristikų AlGaN bandiniai: difrakcijos efektyvumo priklausomybės nuo fotomodifikacijos trukmės skirtingos sudėties, bet tapačiai fotomodifikuotuose junginiuose yra pateiktos Pav. 6; čia, kiekvienas taškas atitinka fotomodifikaciją ties $N_{mod} = 2\times10^{20}$ cm^{-3} krūvininkų tankiu. Paveiksle matyti stipri Al koncentracijos įtaka bandinių jautrumui – nespindulinės rekombinacijos trukmės krytis yra didžiausias Al turtinguose junginiuose. Tą lemia didelių krūvininkų tankių srityje vyraujanti itin sparti netiesinė nespindulinė krūvininkų rekombinacija (apibūdinama B_{nr} koeficientu), labiausiai išreikšta aukštos Al koncentracijos bandiniuose (žr. Pav. 4). Ši sparti rekombinacija sąlygoja daugybės krūvininkų žūtį, gausų REDR reakcijų kiekį ir didelį REDR generuotų defektų – SRH rekombinacijos centrų – prieaugį. Kitų parametrų (tokių kaip termalizacijos energija ar pradinė τ_{SRH} trukmė) įtaka fotomodifikacijos baigčiai yra aptariama *The procedure and the aftermath* skyriuje.

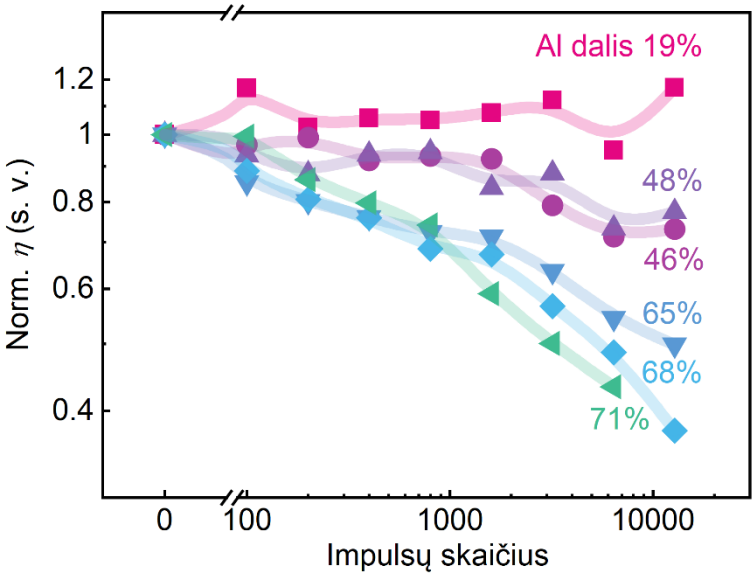

Pav. 6. Normuoto difrakcijos efektyvumo priklausomybė nuo fotomodifikacijos trukmės įvairios sudėties AlGaN sluoksniuose, fotomodifikuotuose ties $N_{mod} \approx 2\times10^{20}$ cm^{-3} krūvininkų tankiu. *Adaptuota pagal straipsnį B.*

Fotomodifikacija turėjo įtaką ne tik krūvininkų rekombinacijai, bet ir difuzijai. Pastarasis efektas yra matomas Pav. 7 pateiktose kreivėse: difuzijos koeficiento, D, ir efektyvios rekombinacijos trukmės, τ, priklausomybėse nuo fotomodifikacijos impulsų skaičiaus $Al_{0.48}Ga_{0.52}N$ junginyje, fotomodifikuotame ties $N_{mod} = 2\times10^{20}$ cm^{-3} krūvininkų tankiu. Rekombinacijos trukmę atitinkanti priklausomybė atkartoja Pav. 6 pateiktas tendencijas – τ tolygiai mažėja ilgėjant fotomodifikacijai. Skirtingai nuo krūvininkų rekombinacijos, fotomodifikacijos poveikis difuzijai nėra monotoniškas: trumpų fotomodifikacijų srityje stebimas staigus D augimas, tuo tarpu ilgų – tolydus mažėjimas. Pradinis D padidėjimas (kartu su nežymiu τ sumažėjimu) lemia ir difuzijos ilgio, $L = \sqrt{\tau D}$, išaugimą, aukščiausiame taške (atitinkančiame 200 impulsų trukmės fotomodifikaciją) siekiantį 45% didesnes nei pradinės vertes. Krūvininkų difuzijos savybių fotomodifikacija kontroliniame $Al_{0.19}Ga_{0.81}N$ bandinyje yra aptariama *The procedure and the aftermath* skyriuje.

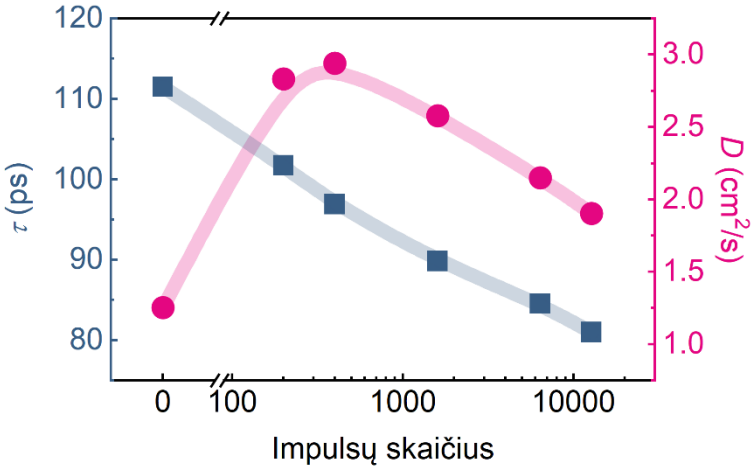

Pav. 7. Krūvininkų gyvavimo trukmės (mėlyni stačiakampiai) ir difuzijos koeficiento (rausvi apskritimai) priklausomybės nuo fotomodifikacijos trukmės $Al_{0.48}Ga_{0.52}N$ sluoksnyje, fotomodifikuotame ties $N_{mod} = 2\times10^{20}$ cm^{-3} krūvininkų tankiu. *Adaptuota pagal straipsnį B.*

Trumpos fotomodifikacijos indukuotą difuzijos koeficiento prieaugį galimai lemia REDR aktyvuotas kristalinės struktūros persitvarkymas, t.y., atomų persiskirstymas ir migracija.[155,166–168] Šis persiskirstymas gali anihiliuoti krūvininkų sklaidos centrus ir padidinti krūvininkų judrį. Analogiškai, dideliu fotomodifikuojančių impulsų skaičiumi indukuojamą D sumažėjimą galimai sąlygoja REDR valdoma sklaidos centrų generacija. Lygiagrečiai sklaidos centrams REDR efektas generuoja ir SRH rekombinacijos centrus. Pastarieji defektai galėtų būti priskiriami azoto vakansijoms,[155,162,163,169,170] aliuminio ir galio oksidams[155,171–174] bei sudėtingesniems šių ir kitų defektų kompleksams.

Apibendrinant galima pasakyti, kad fotomodifikacijos poveikis krūvininkų dinamikos savybėms yra tuo stipresnis, kuo ilgesnė yra fotomodifikacijos trukmė, aukštesnis fotomodifikacijos metu generuojamų nepusiausvirųjų krūvininkų tankis ar Al koncentracija fotomodifikuojamuose AlGaN junginiuose. Paskutinės dvi tendencijos yra nulemtos spartaus netiesinio nespindulinės rekombinacijos kanalo, vyraujančio didelių krūvininkų tankių srityje Al turtinguose junginiuose.

Skyrius C: Krūvininkų dinamika AlGaN/GaN sandūroje

Šiame skyriuje yra tiriamos krūvininkų dinamikos savybės AlGaN/GaN heterosandūrose, ypatingą dėmesį skiriant sandūrinės rekombinacijos (analogiškos paviršinei rekombinacijai nuogo medžiagos paviršiaus atveju) mechanizmo charakterizavimui. Tyrimų apie nitridinius junginius erdvėje yra įprasta manyti, kad paviršinės rekombinacijos įtaka nitridinių prietaisų veikimui nėra žymi dėl sąlyginai žemo paviršinės rekombinacijos greičio,[175–179] trumpo difuzijos ilgio ties darbiniais krūvininkų tankiais[180,181] ir tariamai efektingo prietaise esančių apatinių sluoksnių/sandūrų pasyvavimo viršutiniais. Priešingai šiai nuomonei, tyrimas atskleidžia AlGaN/GaN heterosandūrose paviršinę rekombinaciją esant neįprastai sparčiu ir netgi dominuojančiu rekombinacijos procesu, galimai mažinančiu pastaraisiais junginiais grindžiamų prietaisų našumą.

Tyrime buvo charakterizuojamos 12 AlGaN/GaN heterosandūrų (išvardintos lentelėje 1), sudarytų iš skirtingos sudėties ($\bar{x}$ = (0.13, 0.2 ir 0.34)) ir kokybės AlGaN barjerų, užaugintų ant identiškų GaN buferių. Krūvininkų dinamikos savybės buvo nustatomos DDG ir laikinės skyros fotoliuminescencinės spektroskopijos metodikomis (šioje santraukoje aptariami tik DDG matavimų rezultatai). Selektyviam barjerų/buferių žadinimui buvo pasitelkta 266/355 nm bangos ilgio spinduliuotė, atitinkamai; šios žadinimo konfigūracijos yra pavaizduotos Pav. 8.

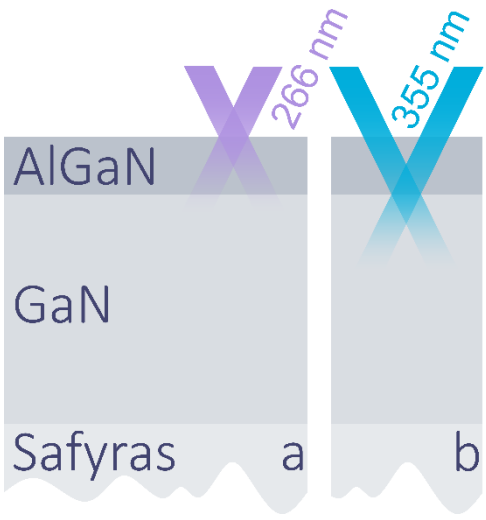

Pav. 8. Supaprastinta DDG eksperimento žadinimo konfigūracijų schema: **a)** AlGaN barjero žadinimas 266 nm bangos ilgio spinduliuote; **b)** GaN buferio žadinimas 355 nm pluošteliu.

Siekiant užauginti skirtingos kokybės AlGaN barjerus buvo varijuojamas prekursorių V/III santykis (lygus dujų srautų santykiui NH_3/(TMGa + TMAl)); barjerų kokybės matu buvo pasirinktas SRH rekombinacijos trukmės, τ_{SRH}^{AlGaN}, parametras. τ_{SRH}^{AlGaN} trukmės skirtingos sudėties AlGaN barjeruose priklausomybė nuo prekursorių V/III santykio yra pateikta Pav. 9. Jame matyti, kad tiek skirtingai augintų, tiek skirtingos sudėties AlGaN barjerų kokybė išties skiriasi. Šiuos skirtumus lemia skirtingi efektai: (i) mažų V/III santykių (valdomų NH_3 srautu) srityje trukmę τ_{SRH}^{AlGaN} kontroliuoja azoto atomų deficito mastas; šiuose bandiniuose galimi azoto vakansijoms (V_N) ir priemaišoms, užimančioms N vietą AlGaN gardelėje, gimininigi defektai; (ii) didelių V/III santykių srityje junginio kokybę riboja N perteklius, stabdantis Al ir Ga atomų migraciją auginamo sluoksnio paviršiuje; šiuose bandiniuose galimi Al ir Ga vakansijoms (V_{Al}, V_{Ga}) gimininigi defektai; (iii) junginiuose su aukštesne Al koncentracija struktūrinės kokybės degradacija įprastai priskiriama žemo Al atomų judrio nulemtiems efektams; šiuo atveju bandiniuose gali vyrauti tiek įvairūs taškiniai (gimtieji ir priemaišiniai), tiek linijiniai defektai, taip pat – fazių atskyrimo ar moduliacijos sukurti defektai. Platesnė diskusija (kartu su ją lydinčiais literatūros šaltiniais) apie AlGaN junginiuose sutinkamus sudėties ar auginimo parametrų sąlygojamus defektus yra pateikta *Carrier dynamics in AlGaN barriers* skyriuje.

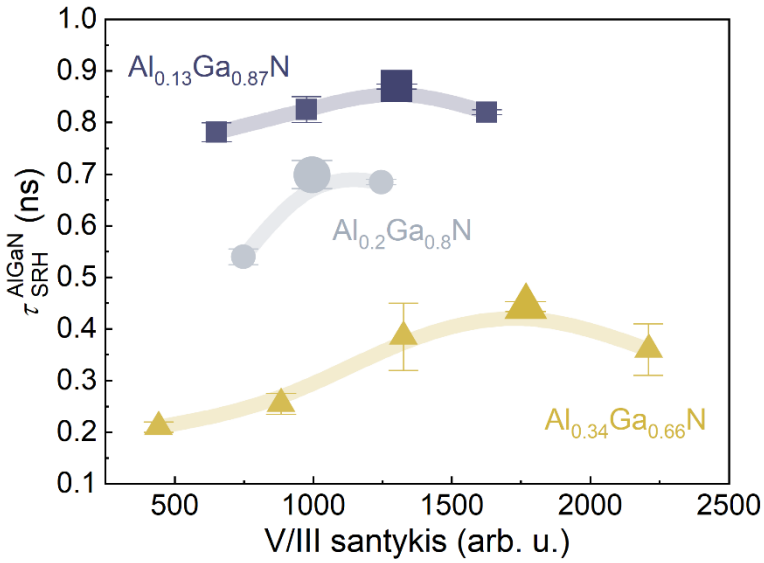

Pav. 9. Nespindulinės rekombinacijos trukmės skirtingos sudėties AlGaN barjeruose priklausomybė nuo prekursorių V/III santykio.

AlGaN barjero kokybė valdė krūvininkų rekombinacijos savybes ne tik pačiame barjere, bet ir po juo esančiame GaN buferyje. Ši [neigiama] barjero įtaka buvo pastebėta pasitelkus efektyvios krūvininkų gyvavimo trukmės GaN buferyje (τ^{GaN}; ši trukmė atspindi nespindulinės rekombinacijos trukmę) priklausomybę nuo SRH rekombinacijos trukmės AlGaN barjere, τ_{SRH}^{AlGaN} (žr. Pav. 10; čia, kiekvieną duomenų tašką atitinka individuali AlGaN/GaN heterosandūra su skirtingos sudėties ir kokybės AlGaN barjeru, charakterizuotu Pav. 9). Kaip matyti Pav. 10, τ^{GaN} trukmė tolygiai mažėja prastėjant barjero kokybei; ši koreliacija išlieka tiek tarp bandinių su skirtingos sudėties barjerais, atitinkančiais optimalias auginimo sąlygas (t.y., optimalius V/III santykius; žr. didelius simbolius), tiek tarp bandinių su panašios sudėties, bet skirtingos kokybės barjerais, atitinkančiais N deficito bei pertekliaus sąlygas (žr. vienodos spalvos simbolius). Panašu, kad rekombinacijos trukmės mažėjimą GaN buferyje lemia ne išimtinai vienos rūšies defektas AlGaN barjere, bet įvairių defektų kombinacija – bendra barjero kokybė.

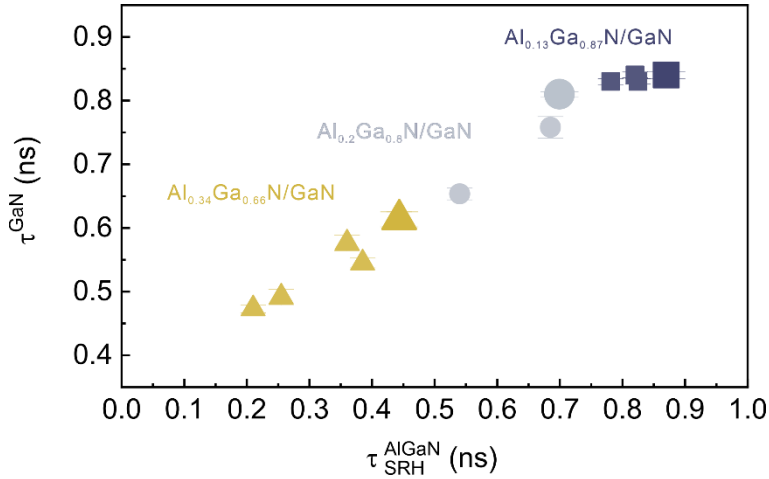

Pav. 10. Krūvininkų gyvavimo trukmės GaN buferyje ties $\Delta N = 5.4\times10^{19}$ cm^{-3} krūvininkų tankiu priklausomybė nuo nespindulinės rekombinacijos trukmės AlGaN barjere.

Detalesniam AlGaN barjero paveiktų nespindulinės rekombinacijos procesų GaN buferyje aprašymui buvo pasitelktas dinaminis ABC modelis: modelio kreivės buvo tapatinamos su GaN buferyje išmatuotomis DDG kinetikomis (detalus tapatinimo procedūros/modelio aprašymas yra pateiktas *Carrier dynamics in GaN buffers* skyriuje). Šis tapatinimas leido atskleisti GaN buferiuose vyraujančius rekombinacijos kanalus (sandūrinės

rekombinacijos arba SRH) bei įvertinti jų spartas. Vieno iš pastarųjų įverčių – sandūrinės rekombinacijos greičio GaN buferyje (S_i) – priklausomybė nuo AlGaN barjero kokybės (τ_{SRH}^{AlGaN}trukmės) ties skirtingais nepusiausvirųjų krūvininkų tankiais ΔN yra pateikta Pav. 11.

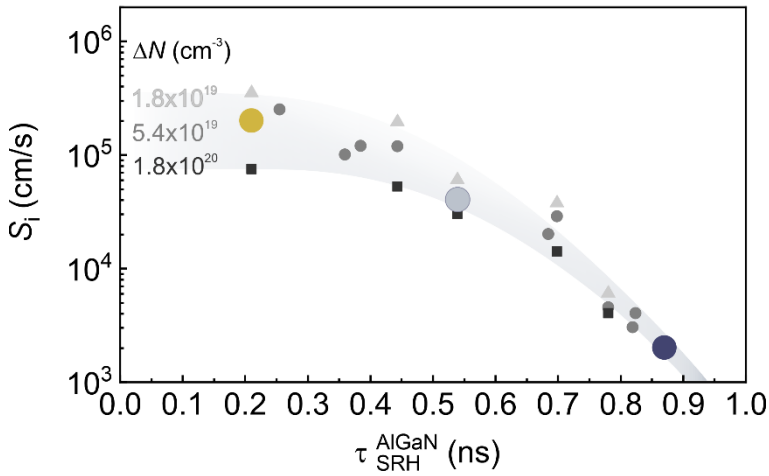

Pav. 11. Sandūrinės rekombinacijos greičio GaN buferyje ties skirtingais nepusiausvirųjų krūvininkų tankiais *ΔN* priklausomybė nuo SRH rekombinacijos trukmės AlGaN barjere.

Kaip matyti paveiksle, krūvininkų žūtis sandūroje neabejotinai spartėja prastėjant barjero kokybei: ties $\Delta N = 5.4\times10^{19}$ cm^{-3} krūvininkų tankiu (žr. apskritimus) S_i greitis sparčiai auga nuo 2×10^3 iki 2×10^5 cm/s τ_{SRH}^{AlGaN} trukmei mažėjant nuo 0.9 iki 0.2 ns. Tuo pačiu metu stebima ir sandūrinės rekombinacijos greičio priklausomybė nuo nepusiausvirųjų krūvininkų tankio: S_i lėtai mažėja didėjant ΔN (tik prastos kokybės bandiniuose; žr. Pav. 11) dėl nespindulinės rekombinacijos centrų sotinimo laisvaisiais krūvininkais. Nepaisant šio mažėjimo, sandūrinės rekombinacijos kanalo sparta bei barjero nulemtas S_i prieaugis išlieka žymiai didesni už SRH rekombinacijos GaN buferyje spartą, $1/\tau_{SRH}^{GaN}$, bei jos prieaugį ($\tau_{SRH}^{GaN}(\tau_{SRH}^{AlGaN})$ priklausomybė santraukoje nepateikta). Tai rodo sandūrinės rekombinacijos mechanizmą esant dominuojančiu (bent jau prasčiausios kokybės bandiniuose), o barjero žalą esant dalinai lokalizuota sandūros srityje.

Skyriaus pabaigai galima pasakyti, kad sparčios sandūrinės rekombinacijos pasekmės prietaiso veikimui yra sunkios. Šių pasekmių pavyzdžiu gali būti IQE(S_i) pokytis hipotetinėje 5 nm storio AlGaN/GaN/AlGaN kvantinėje duobėje: ties aukščiausiomis tyrime nustatytomis S_i vertėmis IQE duobėje sumažėtų net dvejomis eilėmis.

Skyrius D: Krūvininkų dinamika InN junginiuose

Šiame skyriuje yra tiriamos krūvininkų rekombinacijos ir šalutinių skylių difuzijos savybės tikslingai nelegiruotuose n-tipo InN junginiuose su aukštomis pusiausvirųjų elektronų koncentracijomis. Krūvininkų rekombinacijos atveju, tyrimas siekia išvengti praeities studijas kamavusių problemų – tokių kaip dviprasmiško krūvininkų tankio ar gyvavimo trukmės vertinimo, rekombinacijos procesų charakterizavimo siauroje krūvininkų tankių srityje ir išvadų formavimo remiantis mažais bandinių rinkiniais bei aukštos dispersijos duomenų masyvais – ir atskleisti InN junginiuose vyraujančius rekombinacijos mechanizmus nekeliančiu abejonių būdu. Krūvininkų difuzijos atveju, tyrimas siekia charakterizuoti šalutinių skylių pernašą iki šiol nenagrinėtoje elektronų tankių srityje, apimančioje $N = 10^{18} – 10^{20}$ cm^{-3} diapazoną.

Vyraujantiems rekombinacijos mechanizmams InN junginiuose atskleisti buvo nustatyta efektinės rekombinacijos trukmės, τ, priklausomybė nuo krūvininkų tankio, N; pastaroji priklausomybė yra pateikta Pav. 12. Čia, N atitinka suminį pusiausvirųjų, N_e, ir nepusiausvirųjų, ΔN, elektronų tankį, $N = N_e + \Delta N$; N_e sandas yra bandinio kokybės funkcija, tuo tarpu ΔN – žadinimo intensyvumo. Rekombinacijos trukmėms τ patikimai įvertinti buvo pritaikytas itin tikslus femtosekundinės skyros DDG metodas (detali vertinimo procedūra yra aprašyta *Extraction of LITG decay rates* skyriuje; DDG metodo privalumai lyginant su kitomis laikinės skyros metodikomis yra pateikti *Carrier recombination* skyriuje). Bandinių spektrui ir stebimam elektronų tankio diapazonui išplėsti buvo pasitelkti įvairios kokybės/storio MOCVD ir MBE būdais auginti InN sluoksniai su skirtingomis pusiausvirųjų elektronų koncentracijomis (sluoksniai atrinkti iš 2 lentelėje pateikto bandinių komplekto).

Kaip matyti paveiksle, krūvininkų gyvavimo trukmė įvairiuose InN junginiuose (besiskiriančiuose kokybe ir prigimtimi) paklūsta bendrai elektronų tankiu valdomai tendencijai. Ši tendencija patiria kelias transformacijas: (i) diapazone $N \approx 10^{18} \div 5\times10^{18}$ cm^{-3} rekombinacijos trukmė τ silpnai priklauso nuo N, ir atspindi SRH rekombinacijos trukmę; (ii) diapazone $N \approx 7\times10^{18} \div 5\times10^{19}$ cm^{-3} rekombinacijos trukmė τ sparčiai mažėja kylant N pagal dėsnį $\tau \propto N^{-2}$, apibūdinantį tiesioginės Ožė rekombinacijos mechanizmą; (iii) intervale $N \gtrsim 5\times10^{19}$ cm^{-3} τ kritimas lėtėja – Ožė rekombinacijos sparta sotinasi. Šioms transformacijoms aprašyti ir rekombinacijos koeficientams įvertinti buvo pasitelkta $\frac{1}{\tau} = \frac{1}{\tau_{\mathrm{SRH}}} + C(N)N^2$ išraiška, suformuota iš žemuose krūvininkų tankiuose vyraujančio SRH

rekombinacijos sando $(1/\tau_{SRH})$ ir aukštuose N dominuojančio Ožė rekombinacijos sando $(C(N)N^2)$. Ožė rekombinacijos lėtėjimui ties itin aukštais N aprašyti pasitelkta $C(N) = \frac{C_0}{\left(1+\frac{N}{N^*}\right)}$ išraiška, apibūdinanti Ožė rekombinacijos koeficiento, C, mažėjimą dėl fazinės erdvės pildymo ir krūvininkų išsigimimo; čia, C_0 yra pradinis Ožė koeficientas, atspindintis Ožė rekombinacijos spartą ties mažu N, o N^* yra junginiui charakteringas krūvininkų tankis, ties kuriuo $C = 0.5C_0$. Pastarosiomis išraiškomis paremtą $\tau(N)$ kreivę sutapatinus su eksperimentinėmis τ vertėmis (žr. Pav. 12) buvo įvertinti rekombinacijos koeficientai: $\tau_{SRH} = 600$ ps, $N^* = 5\times10^{19}$ cm^{-3} ir $C_0 = 8\times10^{-29}$ cm^6/s. Vienas iš jų – C_0 – sutampa su Ožė koeficiento vertėmis kituose analogiško draustinių energijų tarpo puslaidininkiuose.[127] Šis sutapimas patvirtina tiesioginės Ožė rekombinacijos kaip vyraujančio rekombinacijos mechanizmo InN junginiuose (ties aukštais N) hipotezę.

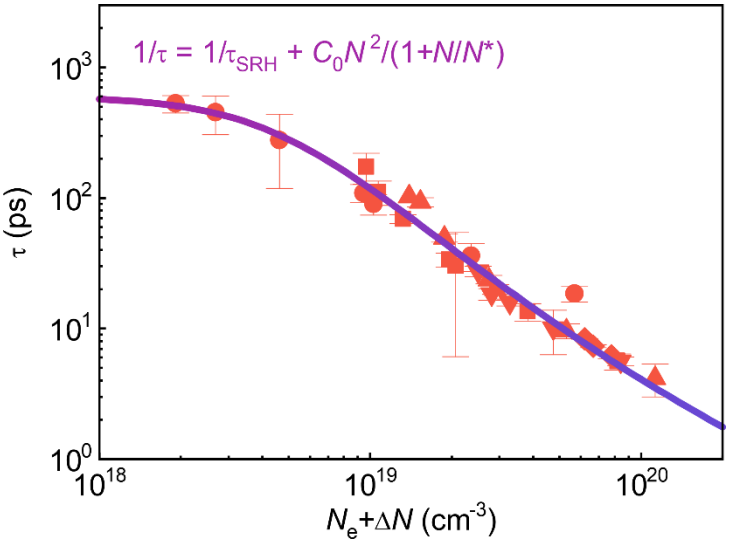

Pav. 12. Krūvininkų gyvavimo trukmės priklausomybė nuo suminio elektronų tankio InN junginiuose; skirtingi simboliai atitinka skirtingus bandinius. Ištisinė kreivė yra apskaičiuota remiantis paveiksle nurodyta išraiška. *Adaptuota pagal straipsnį D.*

Krūvininkų pernašos savybės InN junginiuose buvo charakterizuojamos DDG būdu tapačiame rekombinacijos savybių tyrimui bandinių rinkinyje ir elektronų tankio diapazone. Šio charakterizavimo rezultatas – atskleistos iki šiol nenagrinėtos šalutinių skylių difuzijos koeficientų, D, ir difuzijos ilgių, $L = \sqrt{\tau D}$, priklausomybės nuo suminio elektronų tankio $N = 10^{18} – 10^{20}$ cm^{-3} srityje; priklausomybės yra pateiktos Pav. 13. Pažymėtina, kad pastarajame

paveiksle pavaizduotos krūvininkų difuzijos koeficientų vertės faktiškai aprašo ambipolinę krūvininkų pernašą, prilyginamą skylių pernašai tik $N \lesssim 5\times10^{19}$ cm^{-3} diapazone (plačiau apie tai – *Carrier diffusion* skyriuje).

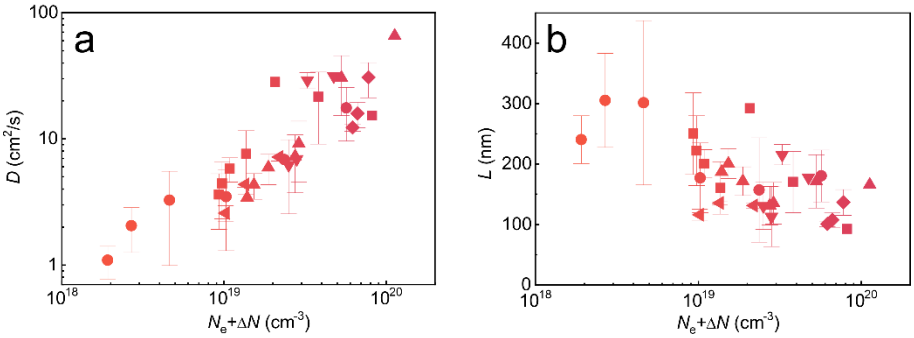

Pav. 13. Krūvininkų difuzijos koeficiento **(a)** ir difuzijos ilgio **(b)** priklausomybės nuo suminio elektronų tankio InN junginiuose; skirtingi simboliai atitinka skirtingus bandinius. *Adaptuota pagal straipsnį D.*

Kaip matyti paveiksle (žr. Pav. 13a), elektronų tankio prieaugis nuo $N \approx 2\times10^{18}$ cm^{-3} iki 1×10^{20} cm^{-3} sąlygoja difuzijos koeficiento padidėjimą nuo $D = 1$ cm^2/s iki 30-65 cm^2/s. Dalis šių verčių – atitinkančių žemo elektronų tankio sritį – yra įprastos ir atkartojančios anksčiau publikuotąsias aukštos kokybės MBE būdu augintuose InN sluoksniuose su žema pusiausvirųjų elektronų koncentracija ($D \approx 2$ cm^2/s ties $N_e \approx (0.4\text{-}1.4)\times10^{18}$ cm^{-3} [228,229]). Likusios D vertės – atitinkančios aukšto elektronų tankio sritį – yra neįprastai didelės ir pirmą kartą stebimos InN junginiuose. Šis staigus D padidėjimas galimai yra nulemtas krūvininkų išsigimimo ir ultra sparčių pernašos efektų, tokių kaip lengvųjų skylių pernaša prieš įvykstant termalizacijai ar balistinė krūvininkų pernaša. Detalesnis pastarųjų efektų aprašas yra pateiktas *Carrier diffusion* skyriuje.

Krūvininkų difuzijos ilgio priklausomybė nuo elektronų tankio InN junginiuose (žr. Pav. 13b) yra ne mažiau unikali: L beveik nesikeičia kylant N dėl viena kitą kompensuojančių $\tau(N)$ ir $D(N)$ tendencijų. Be to, vidutinė L vertė nenukrenta žemiau 160 nm ribos, tapačios maksimaliam šviesos sugerties gyliui tirtuose InN sluoksniuose. Faktiškai, tai rodo fotogeneruotų krūvininkų ekstrakciją esant įmanoma net ir prasčiausios kokybės InN junginiuose, ir žymi InN bazę tinkama fotoelektriniams taikymams.

Apibendrinant galima pasakyti, kad elektronų tankis yra vienas svarbiausių InN junginį charakterizuojančių parametrų, valdančių ne tik paprastą elektrinio laidumo matą, bet ir kompleksines krūvininkų rekombinacijos bei difuzijos savybes.

Skyrius E: Krūvininkų dinamika protonais apšvitintuose InN junginiuose

Šiame skyriuje yra tiriama kosminę spinduliuotę atitinkančio apšvitinimo protonais įtaka krūvininkų dinamikos savybėms InN junginiuose, įvertinamas InN atsparumas apšvitinimui, bei atliekamas detalus šio įverčio palyginimas su kitų puslaidininkių, formuojančių dabartinę kosmose eksploatuojamų fotoelektrinių prietaisų bazę, atsparumu. Tyrimas yra paskatintas artimo InN junginiams III-N grupės nario – GaN – taikymų ypatingai atšiauriose kosminėse aplinkose vystymo,[6,7] grindžiamo itin aukštu GaN atsparumu aukštos energijos dalelių poveikiui.[248,249] Tyrime pasirinkti uždaviniai ir jų sprendimo būdas yra unikalūs analogiškų InN tyrimų erdvėje, retai peržengiančioje tradicinį legiravimo problemos nagrinėjimo ir Holo eksperimento formatą.[54,234,250]

Tyrimui buvo pasirinkti trys skirtingos pusiausvirųjų elektronų koncentracijos MOCVD būdu auginti InN sluoksniai: bandinys *S1*, atitinkantis $N_e = 1.3\times10^{19}$ cm^{-3}, *S2* – $N_e = 5.9\times10^{19}$ cm^{-3} ir *S3* – $N_e = 1.9\times10^{19}$ cm^{-3}; bandinių elektriniai parametrai yra pateikti 2 lentelėje. Toliau, bandiniai buvo apšvitinami Cs jonų šaltinio išspinduliuotais protonais, pagreitintais iki 1.4 MeV energijos jonų greitintuvu. Greitinamų dalelių rūšis ir energija buvo parinktos siekiant atkartoti prietaisams žalingą kosminės spinduliuotės foną; laboratorinėmis sąlygomis ši energija turi pakliūti į $1 \div 10$ MeV intervalą[253,255] (protonų atveju; to priežastys yra aprašytos *Chapter E: Carrier dynamics in proton-irradiated InN* skyriuje). Pažymėtina, kad parinktos energijos protonai faktiškai neprarado greičio/nebuvo sugeriami tirtuose InN bandiniuose dėl žymiai didesnio pastarųjų dalelių prasiskverbimo gylio (lygaus ~25 μm InN junginiuose; įvertinta SRIM programine įranga[261]) lyginant su InN sluoksnių storiu (<390 nm).

Tyrimo metu apšvitinimo „intensyvumas“, vertinamas protonų įtėkio parametru, ϕ, buvo varijuojamas plačiame intervale (nuo $\phi = 1\times10^{12}$ iki 1×10^{16} cm^{-2}) keičiant ekspozicijos trukmę. Lyginant su natūralia kosmine spinduliuote Žemės aplinkoje, tyrime pasiekti įtėkiai yra žymiai aukštesni: metinis Saulės įvykių metu (angl. Solar particle event; SPE) išspinduliuotų 1 MeV energijos protonų įtėkis 95% atvejų neviršija $\phi = 10^{11}$ cm^{-2} [254] (tarpplanetinėje erdvėje). Nors sintetiniai įtėkiai, atrodytų, realiomis sąlygomis nėra pasiekiami, tam tikrais atvejais „natūralios“ spinduliuotės intensyvumas gali išaugti šimtus ir tūkstančius kartų bei tapti palyginamu laboratoriniams, pvz., ypatingai retų ir intensyvių SPE įvykių, tokių kaip Karingtono,[259] egzoatmosferinės termobranduolinės bombos sprogdinimo,

tokio kaip *Starfish Prime* testas,[260] bei skrydžio aplink stiprios magnetosferos planetą, tokią kaip Jupiteris, metu.[260] Tai reiškia, kad šio tyrimo rezultatai prognozuoja krūvininkų dinamikos savybių evoliuciją InN junginiuose nepaprastai ilgų kosminių misijų ar ekstremalių radiacinių aplinkų sąlygomis.

Pirmasis tyrimo rezultatas – DDG būdu įvertintos krūvininkų gyvavimo trukmės, τ, priklausomybė nuo protonų įtėkio, ϕ, InN sluoksniuose su skirtingomis pradinėmis pusiausvirųjų elektronų koncentracijomis, N_e – yra pateiktas Pav. 14a. Jame matyti, kad τ trukmė neapšvitintuose sluoksniuose (ties $\phi = 0$) siekia nuo 13 ps (žemesnės kokybės bandinyje S2) iki ~100 ps (aukštesnės kokybės bandiniuose S1 ir S3), ir yra valdoma pradinės N_e vertės, susietos su Ožė rekombinacijos sparta (žr. skyrių D). Intensyvaus apšvitinimo sąlygomis (ties $\phi = 10^{16}$ cm^{-2}), τ visuose sluoksniuose sumažėja iki kelių pikosekundžių. Šis sumažėjimas yra sąlygotas išaugusios pusiausvirųjų elektronų koncentracijos (pavaizduota Pav. 14b) ir dėl to paspartėjusios Ožė rekombinacijos. N_e koncentracija, savo ruožtu, kyla augant apšvitinimo intensyvumui dėl didėjančios donorinių defektų[250] – galimai azoto vakansijų[264] – koncentracijos. $\tau(N)$ priklausomybė, suformuota remiantis $\tau(\phi)$ ir $N_e(\phi)$ tendencijomis (santraukoje nepateikta), gali būti apibūdinta analogiška neapšvitintų junginių atvejui išraiška $\frac{1}{\tau} = \frac{C_0 N^2}{\left(1+\frac{N}{N^*}\right)}$ su identiškais abiejų tipų bandiniams tapatinimo parametrais $N^* = 5\times10^{19}$ cm^{-3} ir $C_0 = 8\times10^{-29}$ cm^6/s. Šis rekombinacijos koeficientų sutapimas rodo, kad protonų apšvitinimo indukuoti defektai InN junginiuose tėra elektronų šaltinis Ožė rekombinacijos procesui.

Kitame tyrimo etape yra koncentruojamasi į protonų apšvitinimo įtaką krūvininkų pernašai: tiek elektronų, tiek skylių. Holo elektronų judrio, μ_e, priklausomybė nuo protonų įtėkio skirtingos kokybės InN sluoksniuose yra pavaizduota Pav. 14c. Jame matyti, kad elektronų judris stipriai apšvitintuose (ties $\phi = 10^{16}$ cm^{-2}) InN junginiuose tesiekia 110 – 190 cm^2/Vs, tuo tarpu nepaveiktuose bandiniuose – μ_e = 420 – 810 cm^2/Vs. Šis rezultatas yra dažnai sutinkamas, o jo paaiškinimas, siejamas su apšvitinimo indukuotų sklaidos centrų/donorinių defektų koncentracijos prieaugiu, yra retai ginčijamas.[168,250]

Priešingai elektronų pernašos tyrimams, skylių pernaša apšvitintuose InN junginiuose iki šiol nebuvo detaliai charakterizuota ir yra labiau netikėta: skylių difuzijos koeficientas, D, stipriai išauga kylant apšvitinimo intensyvumui (nuo D = 5 – 8 cm^2/s ties $\phi = 0$ iki D = 100 – 140 cm^2/s ties $\phi = 10^{16}$ cm^{-2}; žr. Pav. 14d). Šis D prieaugis yra analogiškais neapšvitintuose InN junginiuose stebėtai $D(N)$ priklausomybei (žr. Pav. 13a), ir galimai yra nulemtas padidėjusios pusiausvirųjų elektronų koncentracijos efektų:

krūvininkų išsigimimo, netermalizuotų lengvųjų skylių dalyvavimo pernašoje bei kt. (aprašytų *Carrier diffusion* skyriuje).

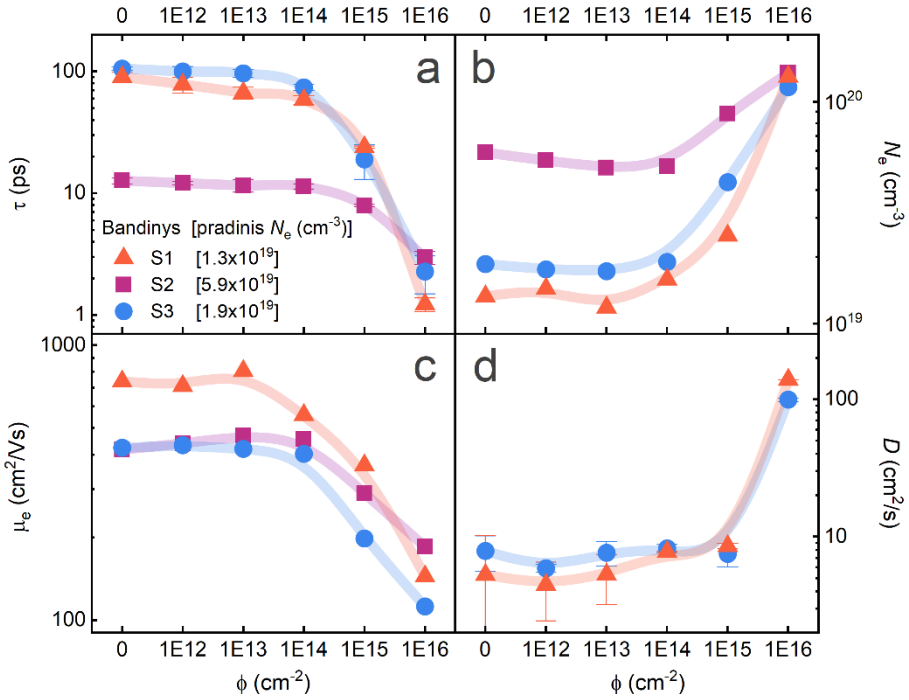

Pav. 14. Krūvininkų gyvavimo trukmės **(a)**, pusiausvirųjų elektronų koncentracijos **(b)**, Holo elektronų judrio **(c)** ir difuzijos koeficiento **(d)** priklausomybės nuo protonų įtėkio InN sluoksniuose su skirtingomis pradinėmis pusiausvirųjų elektronų koncentracijomis. *Adaptuota pagal straipsnį E.*

Paskutiniame tyrimo etape yra atliktas InN junginių atsparumo protonų apšvitinimui vertinimas ir šio įverčio palyginimas su kitų puslaidininkių atsparumu. Tam pasitelkta Naval Research laboratorijos metodologija[253] – prietaisų našumą lemiančio parametro (šiuo atveju – τ) degradacijos unikalaus dozės vieneto (poslinkio žalos dozės, D_d) skalėje nustatymas. Protonų įtėkio konvertavimas į D_d dozę yra atliktas pasitelkus išraišką $D_d = \phi \times S(E)$, kur $S(E)$ – savitasis medžiagos žalos koeficientas, priklausantis nuo dalelių energijos ir atitinkantis NIEL (angl. Nonionizing energy loss) funkciją; NIEL funkcijos apibūdinimas yra pateiktas *Chapter E: Carrier dynamics in proton-irradiated InN* skyriuje.

Eksperimentiškai įvertintų rekombinacijos trukmių priklausomybės nuo poslinkio žalos dozės InN junginiuose su aukšta N_e koncentracija (τ vertės yra tapačios Pav. 14a pateiktoms vertėms S1 ir S2 bandiniuose) bei GaAs, InGaAs

ir InGaN pagrindo šviestukuose (duomenys iš šaltinių[269–272]) yra pateiktos Pav. 15 (žr. įvairių geometrinių figūrų simbolius). Papildomai, paveiksle yra pateikta teoriškai įvertinta $\tau(D_d)$ degradacijos priklausomybė hipotetiniame nulinės elektronų koncentracijos InN junginyje (žr. „$N_e = 0$" kreivę; kreivės įvertinimo metodas aprašytas *Resistance to spacelike radiation* skyriuje). Kaip matyti iš sugretintų $\tau(D_d)$ degradacijos tendencijų, InN junginių atsparumas apšvitinimui yra akivaizdžiai aukščiausias, nepriklausomai nuo bandinio kokybės (N_e koncentracijos). Ši InN savybė – itin vėlyva τ degradacija – yra paaiškinama Ožė rekombinacijos kanalo dominavimu bei apšvitinimo indukuotų SRH rekombinacijos centrų trūkumu.[274]

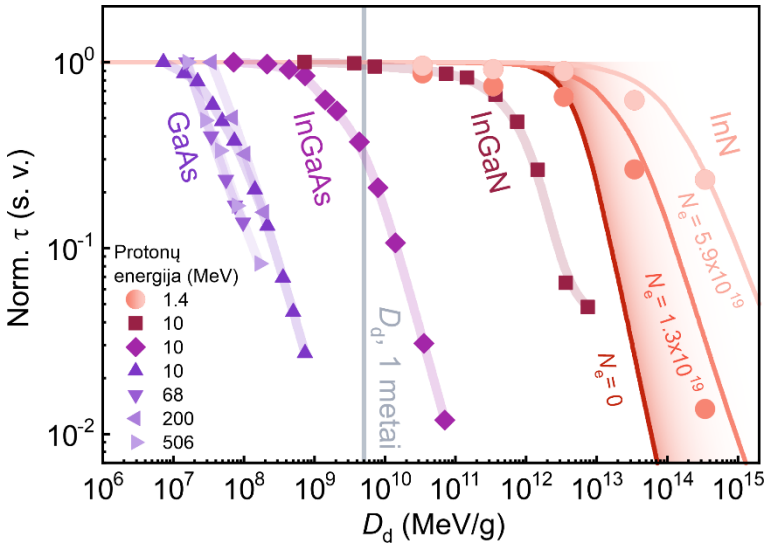

Pav. 15. Normuotos krūvininkų gyvavimo trukmės priklausomybė nuo poslinkio žalos dozės protonais apšvitintuose InN sluoksniuose (S1, S2) su skirtinga pradine pusiausvirųjų elektronų koncentracija (apskritimai), GaAs[269,272] (trikampiai), InGaAs[270] (rombai) ir InGaN[271] (stačiakampiai) pagrindo šviestukuose. Nepermatomos linijos vaizduoja krūvininkų gyvavimo trukmės degradacijos kreives, įvertintas sluoksnių S1, S2 ir hipotetinio nulinės elektronų koncentracijos InN junginio ($N_e = 0$) atvejams. Vertikali pilka linija žymi InN junginyje akumuliuotos Saulės protonų žalos dozės viršutinę metinę ribą tarpplanetinės aplinkos sąlygomis. *Adaptuota pagal straipsnį E.*

Skyriaus pabaigai galima palyginti InN degradacijos slenkstį su kosminės misijos metu akumuliuojama metine Saulės protonų žalos doze. Ši D_d vertė yra lygi ~5×10^9 MeV/g (pažymėta Pav. 15), tuo tarpu τ kryčio slenkstis viršija ~10^{12} MeV/g. Tai reiškia, kad krūvininkų dinamikos savybės InN junginiuose yra atsparios net ir dešimtmečius trunkančiam kosminės spinduliuotės poveikiui.

References

1. Inorganic Crystal Structure Database. Available at: https://icsd.fiz-karlsruhe.de.

2. Zakutayev, A. Design of nitride semiconductors for solar energy conversion. *J. Mater. Chem. A* **4**, 6742–6754 (2016).

3. Chen, A. The Verge. *Gallium nitride is the silicon of the future* (2019). Available at: https://www.theverge.com/2018/11/1/18051974/gallium-nitride-anker-material-silicon-semiconductor-energy. (Accessed: 19th June 2019)

4. Anker. Anker. *PowerPort Atom PD 1 | The World's Smallest Power Delivery Charger* (2019). Available at: https://www.anker.com/deals/powerport_atom. (Accessed: 19th June 2019)

5. Tsao, J. Y. *et al.* Ultrawide-Bandgap Semiconductors: Research Opportunities and Challenges. *Adv. Electron. Mater.* **4**, (2018).

6. Nowakowski, T. Phys. *Gallium nitride processor—next-generation technology for space exploration* (2017). Available at: https://phys.org/news/2017-12-gallium-nitride-processornext-generation-technology-space.html. (Accessed: 19th June 2019)

7. Malewar, A. Techexplorist. *NASA studies space applications for GaN crystals* (2018). Available at: https://www.techexplorist.com/nasa-studies-space-applications-gan-crystals/16010/?utm_source=feedburner&utm_medium=twitter&utm_campaign=Feed%3A+TechExplorist+%28Tech+Explorist%29. (Accessed: 19th June 2019)

8. Snyder, P. J. *et al.* Bioelectronics communication: encoding yeast regulatory responses using nanostructured gallium nitride thin films. *Nanoscale* **10**, 11506–11516 (2018).

9. Snyder, P. J., Kirste, R., Collazo, R. & Ivanisevic, A. Persistent Photoconductivity, Nanoscale Topography, and Chemical Functionalization Can Collectively Influence the Behavior of PC12 Cells on Wide Bandgap Semiconductor Surfaces. *Small* **13**, 1700481 (2017).

10. Chowdhury, F. A., Trudeau, M. L., Guo, H. & Mi, Z. A photochemical diode artificial photosynthesis system for unassisted high efficiency overall pure water splitting. *Nat. Commun.* **9**, 1707 (2018).

11. Berhane, A. M. *et al.* Bright Room-Temperature Single-Photon Emission from Defects in Gallium Nitride. *Adv. Mater.* **29**, 1605092

(2017).

12. Zeng, G., Tan, C. K., Tansu, N. & Krick, B. A. Ultralow wear of gallium nitride. *Appl. Phys. Lett.* **109**, 051602 (2016).

13. Nakamura, S., Mukai, T. & Senoh, M. High-Power GaN P-N Junction Blue-Light-Emitting Diodes. *Jpn. J. Appl. Phys.* **30**, L 1998-L 2001 (1991).

14. Nakamura, S., Mukai, T. & Senoh, M. Candela-class high-brightness InGaN/AlGaN double-heterostructure blue-light-emitting diodes. *Appl. Phys. Lett.* **64**, 1687–1689 (1994).

15. Narukawa, Y., Ichikawa, M., Sanga, D., Sano, M. & Mukai, T. White light emitting diodes with super-high luminous efficacy. *J. Phys. D. Appl. Phys.* **43**, (2010).

16. Hahn, B. *Closing the Green Efficiency Gap ... Status and recent approaches Motivation : The Green Gap Wall-Plug Efficiency*. (2016).

17. Li, P. P. *et al.* Very high external quantum efficiency and wall-plug efficiency 527 nm InGaN green LEDs by MOCVD. *Opt. Express* **26**, 33108 (2018).

18. Lv, Q. *et al.* Realization of Highly Efficient InGaN Green LEDs with Sandwich-like Multiple Quantum Well Structure: Role of Enhanced Interwell Carrier Transport. *ACS Photonics* **6**, 130–138 (2019).

19. Osram. Longer battery life for fitness trackers: Osram increases the efficiency of green LEDs by 40 percent. (2018). Available at: https://www.osram.com/os/press/press-releases/longer-battery-life-for-fitness-trackers-osram-increases-the-efficiency-of-green-leds-by-40-percent.jsp. (Accessed: 17th December 2018)

20. Asif Khan, M., Bhattarai, A., Kuznia, J. N. & Olson, D. T. High electron mobility transistor based on a GaN-AlxGa 1-xN heterojunction. *Appl. Phys. Lett.* **63**, 1214–1215 (1993).

21. Ambacher, O. *et al.* Two-dimensional electron gases induced by spontaneous and piezoelectric polarization charges in N- and Ga-face AlGaN/GaN heterostructures. *J. Appl. Phys.* **85**, 3222–3233 (1999).

22. Ambacher, O. *et al.* Two dimensional electron gases induced by spontaneous and piezoelectric polarization in undoped and doped AlGaN / GaN heterostructures. *J. Appl. Phys.* **87**, 334–344 (2000).

23. Smorchkova, I. P. *et al.* Polarization-induced charge and electron mobility in AlGaN/GaN heterostructures grown by plasma-assisted molecular-beam epitaxy. *J. Appl. Phys.* **86**, 4520–4526 (1999).

24. Ibbetson, J. P. *et al.* Polarization effects, surface states, and the

source of electrons in AlGaN/GaN heterostructure field effect transistors. *Appl. Phys. Lett.* **77**, 250–252 (2000).

25. Zhang, Y., Singh, J. & Introduction, I. Charge control and mobility studies for an AlGaN/GaN high electron mobility transistor. *J. Appl. Phys.* **85**, (1999).

26. Zhang, Y. *et al.* Charge control and mobility in AlGaN/GaN transistors : Experimental and theoretical studies. **87**, 7981–7987 (2000).

27. Hsu, L. & Walukiewicz, W. Effect of polarization fields on transport properties in AlGaN/GaN heterostructures. *J. Appl. Phys.* **89**, 1783–1789 (2001).

28. Mitani, E., Haematsu, H., Yokogawa, S., Nikaido, J. & Tateno, Y. Mass production of high voltage GaAs and GaN devices. in *CS Mantech Conference* 183–186 (2006).

29. Nitronex. *GaN Essentials: Substrates for GaN RF Devices*. (2008).

30. Yasan, A. *et al.* Top-emission ultraviolet light-emitting diodes with peak emission at 280 nm. *Appl. Phys. Lett.* **81**, 801–802 (2002).

31. Sun, W. *et al.* Continuous wave milliwatt power AlGaN light emitting diodes at 280 nm. *Japanese J. Appl. Physics, Part 2 Lett.* **43**, 1419–1421 (2004).

32. Max, S. *et al.* AlGaN Deep-Ultraviolet Light-Emitting Diodes with External Quantum Efficiency above 10%. *Appl. Phys. Express* **5**, 82101 (2012).

33. Takayoshi, T. *et al.* Deep-ultraviolet light-emitting diodes with external quantum efficiency higher than 20% at 275 nm achieved by improving light-extraction efficiency. *Appl. Phys. Express* **10**, 31002 (2017).

34. LG Innotek. LG Innotek Unveils the World's First '100mW' UV-C LED. (2017). Available at: http://www.lginnotek.com/en/itk_news/lg-innotek-unveils-worlds-first-100mw-uv-c-led/. (Accessed: 17th December 2018)

35. LG Innotek. *UV LED Product Catalog*. (2018).

36. Yoshida, H., Yamashita, Y., Kuwabara, M. & Kan, H. Demonstration of an ultraviolet 336 nm AlGaN multiple-quantum-well laser diode. *Appl. Phys. Lett.* **93**, 1–4 (2008).

37. Zhao, S. *et al.* An electrically injected AlGaN nanowire laser operating in the ultraviolet-C band. *Appl. Phys. Lett.* **107**, 1–6 (2015).

38. Zhao, S. *et al.* Three-dimensional quantum confinement of charge carriers in self-organized AlGaN nanowires: A viable route to

electrically injected deep ultraviolet lasers. *Nano Lett.* **15**, 7801–7807 (2015).

39. Zhao, S., Liu, X., Wu, Y. & Mi, Z. An electrically pumped 239 nm AlGaN nanowire laser operating at room temperature. *Appl. Phys. Lett.* **109**, (2016).

40. Gordon, L., Varley, J. B., Lyons, J. L., Janotti, A. & Van de Walle, C. G. Sulfur doping of AlN and AlGaN for improved n-type conductivity. *Phys. Status Solidi - Rapid Res. Lett.* **9**, 462–465 (2015).

41. Taniyasu, Y., Kasu, M. & Makimoto, T. An aluminium nitride light-emitting diode with a wavelength of 210 nanometres. *Nature* **441**, 325–328 (2006).

42. Zhao, S. *et al.* Aluminum nitride nanowire light emitting diodes: Breaking the fundamental bottleneck of deep ultraviolet light sources. *Sci. Rep.* **5**, 1–5 (2014).

43. Clarivate Analytics. Web of Science. (2018). Available at: http://apps.webofknowledge.com.

44. Chen, J., Cheng, G., Stern, E., Reed, M. A. & Avouris, P. Electrically excited infrared emission from InN nanowire transistors. *Nano Lett.* **7**, 2276–2280 (2007).

45. Nguyen, H. P. T., Chang, Y.-L., Shih, I. & Mi, Z. InN p-i-n Nanowire Solar Cells on Si. *IEEE J. Sel. Top. Quantum Electron.* **17**, 1062–1069 (2011).

46. Wu, G. G. *et al.* Near infrared electroluminescence from n-InN/p-GaN light-emitting diodes. *Appl. Phys. Lett.* **100**, (2012).

47. Wu, G. *et al.* Near-infrared electroluminescence emission from an n-InN nanodots/p-Si heterojunction structure. *J. Phys. D. Appl. Phys.* **45**, (2012).

48. Andreev, B. A. *et al.* Towards the indium nitride laser: Obtaining infrared stimulated emission from planar monocrystalline InN structures. *Sci. Rep.* **8**, 1–8 (2018).

49. Shatalov, M., Gaevski, M., Adivarahan, V. & Khan, A. Room-temperature stimulated emission from AlN at 214 nm. *Japanese J. Appl. Physics, Part 2 Lett.* **45**, 1286–1288 (2006).

50. Wu, J. *et al.* Unusual properties of the fundamental band gap of InN. *Appl. Phys. Lett.* **80**, 3967–3969 (2002).

51. Wu, J. *et al.* Effects of the narrow band gap on the properties of InN. *Phys. Rev. B* **66**, 201403 (2002).

52. Mahboob, I., Veal, T. D., McConville, C. F., Lu, H. & Schaff, W. J.

Intrinsic Electron Accumulation at Clean InN Surfaces. *Phys. Rev. Lett.* **92**, 036804 (2004).

53. Anderson, P. A. *et al.* Buried p -type layers in Mg-doped InN. *Appl. Phys. Lett.* **89**, 1–4 (2006).

54. Jones, R. E. *et al.* Evidence for p-type doping of InN. *Phys. Rev. Lett.* **96**, 1–4 (2006).

55. Zhao, Y. *et al.* Near infrared light-emitting diodes based on n-InN/p-NiO/p-Si heterojunction. *J. Lumin.* **173**, 1–4 (2016).

56. Zhao, Y. *et al.* Near infrared electroluminescence from p-NiO/n-InN/n-GaN light-emitting diode fabricated by PAMBE. *J. Lumin.* **186**, 243–246 (2017).

57. Ke, W. C., Liang, Z. Y., Yang, C. Y., Chan, Y. T. & Jiang, C. Y. Improved conversion efficiency of InN/p-GaN heterostructure solar cells with embedded InON quantum dots. *Appl. Phys. Lett.* **108**, 061603 (2016).

58. Le, B. H., Zhao, S., Tran, N. H. & Mi, Z. Electrically injected near-infrared light emission from single InN nanowire p-i-n diode. *Appl. Phys. Lett.* **105**, (2014).

59. Kobayashi, Y., Kumakura, K., Akasaka, T. & Makimoto, T. Layered boron nitride as a release layer for mechanical transfer of GaN-based devices. *Nature* **484**, 223–227 (2012).

60. Novoselov, K. S., Mishchenko, A., Carvalho, A. & Castro Neto, A. H. 2D materials and van der Waals heterostructures. *Science (80-.).* **353**, (2016).

61. Jariwala, D., Marks, T. J. & Hersam, M. C. Mixed-dimensional van der Waals heterostructures. *Nat. Mater.* **16**, 170–181 (2017).

62. Tan, C. *et al.* Recent Advances in Ultrathin Two-Dimensional Nanomaterials. *Chem. Rev.* **117**, 6225–6331 (2017).

63. Frisenda, R. *et al.* Recent progress in the assembly of nanodevices and van der Waals heterostructures by deterministic placement of 2D materials. *Chem. Soc. Rev.* **47**, 53–68 (2018).

64. Li, W. *et al.* Chemically diverse and multifunctional hybrid organic-inorganic perovskites. *Nat. Rev. Mater.* **2**, (2017).

65. Grätzel, M. The rise of highly efficient and stable perovskite solar cells. *Acc. Chem. Res.* **50**, 487–491 (2017).

66. Correa-Baena, J.-P. *et al.* Promises and Challenges of Perovskite Solar Cells in Portable Applications. *Science (80-.).* **358**, 739–744 (2017).

67. Kovalenko, M. V, Protesescu, L. & Bodnarchuk, M. I. Properties and potential optoelectronic applications of lead halide perovskite nanocrystals. *Science (80-.).* **358**, 745–750 (2017).

68. Ono, L. K., Juarez-Perez, E. J. & Qi, Y. Progress on Perovskite Materials and Solar Cells with Mixed Cations and Halide Anions. *ACS Appl. Mater. Interfaces* **9**, 30197–30246 (2017).

69. Petrus, M. L. *et al.* Capturing the Sun: A Review of the Challenges and Perspectives of Perovskite Solar Cells. *Adv. Energy Mater.* **7**, 1–27 (2017).

70. Yang, S., Fu, W., Zhang, Z., Chen, H. & Li, C. Z. Recent advances in perovskite solar cells: Efficiency, stability and lead-free perovskite. *J. Mater. Chem. A* **5**, 11462–11482 (2017).

71. Ščajev, P. *et al.* Two regimes of carrier diffusion in vapor-deposited lead-halide perovskites. *J. Phys. Chem. C* **121**, 21600–21609 (2017).

72. Ščajev, P. *et al.* Diffusion Enhancement in Highly Excited $MAPbI_3$ Perovskite Layers with Additives. *J. Phys. Chem. Lett.* **9**, 3167–3172 (2018).

73. Bannikov, V. V., Shein, I. R. & Ivanovskii, A. L. Electronic structure, chemical bonding and elastic properties of the first thorium-containing nitride perovskite TaThN3. *Phys. Status Solidi - Rapid Res. Lett.* **1**, 89–91 (2007).

74. Sarmiento-Pérez, R., Cerqueira, T. F. T., Körbel, S., Botti, S. & Marques, M. A. L. Prediction of Stable Nitride Perovskites. *Chem. Mater.* **27**, 5957–5963 (2015).

75. Jain, A., Shin, Y. & Persson, K. A. Computational predictions of energy materials using density functional theory. *Nat. Rev. Mater.* **1**, 1–13 (2016).

76. Pickard, C. J. & Needs, R. J. Ab initio random structure searching. *J. Phys. Condens. Matter* **23**, (2011).

77. Curtarolo, S., Morgan, D., Persson, K., Rodgers, J. & Ceder, G. Predicting crystal structures with data mining of quantum calculations. *Phys. Rev. Lett.* **91**, 1–4 (2003).

78. Hautier, G., Fischer, C., Ehrlacher, V., Jain, A. & Ceder, G. Data mined ionic substitutions for the discovery of new compounds. *Inorg. Chem.* **50**, 656–663 (2011).

79. Fischer, C. C., Tibbetts, K. J., Morgan, D. & Ceder, G. Predicting crystal structure by merging data mining with quantum mechanics. *Nat. Mater.* **5**, 641–646 (2006).

80. Jain, A. *et al.* A high-throughput infrastructure for density functional

theory calculations. *Comput. Mater. Sci.* **50**, 2295–2310 (2011).

81. Curtarolo, S. *et al.* The high-throughput highway to computational materials design. *Nat. Mater.* **12**, 191–201 (2013).

82. Saal, J. E., Kirklin, S., Aykol, M., Meredig, B. & Wolverton, C. Materials design and discovery with high-throughput density functional theory: The open quantum materials database (OQMD). *Jom* **65**, 1501–1509 (2013).

83. Oba, F. & Kumagai, Y. Design and exploration of semiconductors from first principles: A review of recent advances. *Appl. Phys. Express* **11**, 1–30 (2018).

84. Meredig, B. *et al.* Combinatorial screening for new materials in unconstrained composition space with machine learning. *Phys. Rev. B - Condens. Matter Mater. Phys.* **89**, 1–7 (2014).

85. Sun, W. *et al.* A Map of the Inorganic Ternary Metal Nitrides. *Prep.* (2018).

86. Sun, W. *et al.* Thermodynamic Routes to Novel Metastable Nitrogen-Rich Nitrides. *Chem. Mater.* **29**, 6936–6946 (2017).

87. Bauers, S. R. *et al.* Ternary Nitride Semiconductors in the Rocksalt Crystal Structure. *arXiv:1810.05668 [cond-mat.mtrl-sci]* (2018).

88. Caskey, C. M., Richards, R. M., Ginley, D. S. & Zakutayev, A. Thin film synthesis and properties of copper nitride, a metastable semiconductor. *Mater. Horizons* **1**, 424–430 (2014).

89. Caskey, C. M. *et al.* Semiconducting properties of spinel tin nitride and other IV3N4polymorphs. *J. Mater. Chem. C* **3**, 1389–1396 (2015).

90. Fioretti, A. N. *et al.* Combinatorial insights into doping control and transport properties of zinc tin nitride. *J. Mater. Chem. C* **3**, 11017–11028 (2015).

91. Zakutayev, A. *et al.* Experimental synthesis and properties of metastable CuNbN2and theoretical extension to other ternary copper nitrides. *Chem. Mater.* **26**, 4970–4977 (2014).

92. Hinuma, Y. *et al.* Discovery of earth-abundant nitride semiconductors by computational screening and high-pressure synthesis. *Nat. Commun.* **7**, 1–10 (2016).

93. Zhang, X., Yu, L., Zakutayev, A. & Zunger, A. Sorting stable versus unstable hypothetical compounds: The case of multi-functional ABX Half-Heusler filled tetrahedral structures. *Adv. Funct. Mater.* **22**, 1425–1435 (2012).

94. Matsuzaki, K., Okazaki, T., Lee, Y. S., Hosono, H. & Susaki, T.

Controlled bipolar doping in Cu3N (100) thin films. *Appl. Phys. Lett.* **105**, 1–5 (2014).

95. Varley, J. B. *et al.* High-Throughput Design of Non-oxide p-Type Transparent Conducting Materials: Data Mining, Search Strategy, and Identification of Boron Phosphide. *Chem. Mater.* **29**, 2568–2573 (2017).

96. Hautier, G., Miglio, A., Waroquiers, D., Rignanese, G. M. & Gonze, X. How does chemistry influence electron effective mass in oxides? A high-throughput computational analysis. *Chem. Mater.* **26**, 5447–5458 (2014).

97. Sun, W. *et al.* The thermodynamic scale of inorganic crystalline metastability. *Sci. Adv.* **2**, (2016).

98. Wang, S., Wang, Z., Setyawan, W., Mingo, N. & Curtarolo, S. Assessing the Thermoelectric Properties of Sintered Compounds via High-Throughput Ab-Initio Calculations. *Phys. Rev. X* **1**, 1–8 (2011).

99. Quayle, P. C., He, K., Shan, J. & Kash, K. Synthesis, lattice structure, and band gap of ZnSnN2. *MRS Commun.* **3**, 135–138 (2013).

100. Chwang, R., Smith, B. J. & Crowell, C. R. Contact size effects on the van der Pauw method for resistivity and Hall coefficient measurement. *Solid State Electron.* **17**, 1217–1227 (1974).

101. Bell, A. *et al.* Exciton freeze-out and thermally activated relaxation at local potential fluctuations in thick Al xGa 1-xN layers. *J. Appl. Phys.* **95**, 4670–4674 (2004).

102. Jurkevičius, J. Photoluminescence Efficiency in Wide-band-gap III-Nitride Semiconductors and their Heterostructures. (Vilnius University, 2016).

103. Eliseev, P. G., Perlin, P., Lee, J. & Osiński, M. 'Blue' temperature-induced shift and band-tail emission in InGaN-based light sources. *Appl. Phys. Lett.* **71**, 569–571 (1997).

104. Li, Q., Xu, S. J., Xie, M. H. & Tong, S. Y. A model for steady-state luminescence of localized-state ensemble. *Europhys. Lett.* **71**, 994–1000 (2005).

105. Wang, Z. *et al.* Consistency on Two Kinds of Localized Centers Examined from Temperature-Dependent and Time-Resolved Photoluminescence in InGaN/GaN Multiple Quantum Wells. *ACS Photonics* **4**, 2078–2084 (2017).

106. Eichler, H. J., Gunter, P. & Pohl, D. W. *Laser-Induced Dynamic Gratings*. (Springer-Verlag, 1986).

107. Ban, K. *et al.* Internal quantum efficiency of whole-composition-range AlGaN multiquantum wells. *Appl. Phys. Express* **4**, 16–19 (2011).

108. Yoshida, H., Kuwabara, M., Yamashita, Y., Uchiyama, K. & Kan, H. Radiative and nonradiative recombination in an ultraviolet GaN/AlGaN multiple-quantum-well laser diode. *Appl. Phys. Lett.* **96**, 2008–2011 (2010).

109. Bulashevich, K. A., Mymrin, V. F., Karpov, S. Y., Zhmakin, I. A. & Zhmakin, A. I. Simulation of visible and ultra-violet group-III nitride light emitting diodes. *J. Comput. Phys.* **213**, 214–238 (2006).

110. Kuokstis, E., Sun, W. H., Shatalov, M., Yang, J. W. & Khan, M. A. Role of alloy fluctuations in photoluminescence dynamics of AlGaN epilayers. *Appl. Phys. Lett.* **88**, 1–4 (2006).

111. Iwata, Y., Banal, R. G., Ichikawa, S., Funato, M. & Kawakami, Y. Emission mechanisms in al-rich AlGaN/AlN quantum wells assessed by excitation power dependent photoluminescence spectroscopy. *J. Appl. Phys.* **117**, 75701 (2015).

112. Chichibu, S. F., Onuma, T., Hazu, K. & Uedono, A. Time-resolved luminescence studies on AlN and high AlN mole fraction AlGaN alloys. *Phys. Status Solidi Curr. Top. Solid State Phys.* **10**, 501–506 (2013).

113. Murotani, H. *et al.* Temperature dependence of localized exciton transitions in AlGaN ternary alloy epitaxial layers. *J. Appl. Phys.* **104**, 053514 (2008).

114. Murotani, H. *et al.* Recombination dynamics of localized excitons in AlxGa1-xN (0.37<x<0.81) ternary alloys. *Phys. status solidi* **8**, 2133–2135 (2011).

115. Chichibu, S. F., Hazu, K., Onuma, T. & Uedono, A. Collateral evidence for an excellent radiative performance of AlxGa1-xN alloy films of high AlN mole fractions. *Appl. Phys. Lett.* **99**, 97–100 (2011).

116. Dmitriev, A. & Oruzheinikov, A. The rate of radiative recombination in the nitride semiconductors and alloys. *J. Appl. Phys.* **86**, 3241–3246 (1999).

117. Im, J. S. *et al.* Radiative carrier lifetime, momentum matrix element, and hole effective mass in GaN. *Appl. Phys. Lett.* **70**, 631–633 (1997).

118. Malinauskas, T., Jarasiunas, K., Heuken, M., Scholz, F. & Brückner, P. Diffusion and recombination of degenerate carrier plasma in GaN. *Phys. Status Solidi Curr. Top. Solid State Phys.* **6**, 743–746 (2009).

119. Malinauskas, T. *et al.* Contribution of dislocations to carrier recombination and transport in highly excited ELO and HVPE GaN layers. *Phys. Status Solidi Basic Res.* **243**, 1426–1430 (2006).

120. Onuma, T. *et al.* Radiative and nonradiative processes in strain-free AlxGa1-xN films studied by time-resolved photoluminescence and positron annihilation techniques. *J. Appl. Phys.* **95**, 2495–2504 (2004).

121. Fan, S. *et al.* Optical investigation of strong exciton localization in high Al composition AlxGa1-xN alloys. *Opt. Express* **21**, 24497 (2013).

122. Lee, S. M. & Bajaj, K. K. A quantum statistical theory of linewidths of radiative transitions due to compositional disordering in semiconductor alloys. *J. Appl. Phys.* **73**, 1788–1796 (1993).

123. Mickevičius, J. *et al.* Internal quantum efficiency in AlGaN with strong carrier localization. *Appl. Phys. Lett.* **101**, 211902 (2012).

124. Bourdon, G., Robert, I., Sagnes, I. & Abram, I. Spontaneous emission in highly excited semiconductors: Saturation of the radiative recombination rate. *J. Appl. Phys.* **92**, 6595–6600 (2002).

125. David, A. & Grundmann, M. J. Droop in InGaN light-emitting diodes: A differential carrier lifetime analysis. *Appl. Phys. Lett.* **96**, 2–5 (2010).

126. Ryu, H. Y., Shin, D. S. & Shim, J. I. Analysis of efficiency droop in nitride light-emitting diodes by the reduced effective volume of InGaN active material. *Appl. Phys. Lett.* **100**, 1–5 (2012).

127. Bulashevich, K. A. & Karpov, S. Y. Is Auger recombination responsible for the efficiency rollover in III-nitride light-emitting diodes? *Phys. Status Solidi Curr. Top. Solid State Phys.* **5**, 2066–2069 (2008).

128. Saxena, T. *et al.* Low threshold for optical damage in AlGaN epilayers and heterostructures. *J. Appl. Phys.* **114**, 203103 (2013).

129. Kimerling, L. C. Recombination enhanced defect reactions. *Solid State Electron.* **21**, 1391–1401 (1978).

130. Lang, D. V. Recombination-Enhanced Reactions in Semiconductors. *Annu. Rev. Mater. Sci.* **12**, 377–398 (1982).

131. Sumi, H. Phonon-kick mechanism for defect reactions enhanced by electronic excitation. *J. Phys. C Solid State Phys.* **17**, 6071–6086 (1984).

132. Harada, Y. *et al.* Current-pulse-width control of degra- dation in II-VI and III-N compound blue-UV-white LEDs. *Phys. Status Solidi*

Curr. Top. Solid State Phys. **9**, 1844–1847 (2012).

133. Storasta, L., Carlsson, F. H. C., Bergman, J. P. & Janźn, E. Observation of recombination enhanced defect annealing in 4H-SiC. *Appl. Phys. Lett.* **86**, 1–3 (2005).

134. Reshchikov, M. A. *et al.* Unstable luminescence in GaN and ZnO. *Phys. B Condens. Matter* **376**–**377**, 715–718 (2006).

135. Newton, M. E., Campbell, B. A., Twitchen, D. J., Baker, J. M. & Anthony, T. R. Recombination-enhanced diffusion of self-interstitial atoms and vacancy-interstitial recombination in diamond. *Diam. Relat. Mater.* **11**, 618–622 (2002).

136. Jortner, J. Dynamics of the Primary Events in Bacterial Photosynthesis. *J. Am. Chem. Soc.* **102**, 6676–6686 (1980).

137. Seitz, F. & Koehler, J. S. Displacement of Atoms during Irradiation. in *Solid State Physics: Advances in Research and Applications* (eds. Seitz, F. & Turnbull, D.) 351–378 (Academic Press Inc., 1956).

138. Gold, R. D. & Weisberg, L. R. Permanent degradation of GaAs tunnel diodes. *Solid State Electron.* **7**, 811–821 (1964).

139. Weeks, J. D., Tully, J. C. & Kimerling, L. C. Theory of recombination-enhanced defect reactions in semiconductors. *Phys. Rev. B* **12**, 3286–3292 (1975).

140. Sumi, H. Dynamic defect reactions induced by multiphonon nonradiative recombination ofinjected carriers at deep levels in semiconductors. *Phys. Rev. B* **29**, 4616–4630 (1984).

141. Yassievich, I. N. Recombination-induced defect heating and related phenomena. *Semicond. Sci. Technol.* **9**, 1433–1453 (1994).

142. Shun-Lien Chuang *et al.* Kinetic model for degradation of light-emitting diodes. *IEEE J. Quantum Electron.* **33**, 970–979 (1997).

143. Shinozuka, Y. Mechanisms of capture- and recombination-enhanced defect reactions in semiconductors. *Phys. B* **308**, 506–509 (2001).

144. Shinozuka, Y., Wakita, M. & Suzuki, K. Phonon-kick mechanism for defect reactions in semiconductors. *Jpn. J. Appl. Phys.* **51**, (2012).

145. Maeda, K. *et al.* Electronically induced dislocation glide motion in hexagonal GaN single crystals. *Phys. B Condens. Matter* **273**, 134–139 (1999).

146. Medvedev, O. & Vyvenko, O. Intersection Nodes of Basal Screw Dislocations as Luminous Quantum Dots in GaN. *Phys. Status Solidi - Rapid Res. Lett.* **11**, 1–4 (2017).

147. Tomiya, S., Hino, T., Goto, S., Takeya, M. & Ikeda, M. Dislocation

related issues in the degradation of GaN-based laser diodes. *IEEE J. Sel. Top. Quantum Electron.* **10**, 1277–1286 (2004).

148. Yakimov, E. B., Vergeles, P. S., Polyakov, A. Y., Lee, I. H. & Pearton, S. J. Movement of basal plane dislocations in GaN during electron beam irradiation. *Appl. Phys. Lett.* **106**, (2015).

149. Lim, H. *et al.* Influence of laser lift-off on optical and structural properties of InGaN/GaN vertical blue light emitting diodes. *AIP Adv.* **2**, 022122 (2012).

150. Lam, N. D. *et al.* Enhanced Luminescence of InGaN / GaN Vertical Light Emitting Diodes with an InGaN Protection Layer. in *Proceedings of the International Conference Nanomaterials: Applications and Properties* **2**, 1–4 (2013).

151. Nakamura, S., Hoshino, K., Ikadai, Y., Suda, M. & Okumura, T. Anomalous enhancement of in-diffusion of plasma-induced defects in GaN upon ultraviolet-light irradiation. *Jpn. J. Appl. Phys.* **52**, (2013).

152. Hayashi, K., Sasaki, H. & Oishi, T. Analysis of on-state gate current of AlGaN/GaN high-electron-mobility transistor under electrical and thermal stresses. *Jpn. J. Appl. Phys.* **52**, (2013).

153. Cao, X. A., Sandvik, P. M., LeBoeuf, S. F. & Arthur, S. D. Defect generation in InGaN/GaN light-emitting diodes under forward and reverse electrical stresses. *Microelectron. Reliab.* **43**, 1987–1991 (2003).

154. Tsujio, T., Oda, M. & Shinozuka, Y. First-principles calculation of electron-phonon coupling at a Ga vacancy in GaN. *Jpn. J. Appl. Phys.* **56**, (2017).

155. Cao, X. A., Syed, A. A. & Piao, H. Investigation of the electronic properties of nitrogen vacancies in AlGaN. *J. Appl. Phys.* **105**, 63707 (2009).

156. Jiménez, J. Laser diode reliability: Crystal defects and degradation modes. *Comptes Rendus Phys.* **4**, 663–673 (2003).

157. Nikishin, S. A. *et al.* Short-period superlattices of AlN⁄Al 0.08Ga0.92N grown on AlN substrates. *Appl. Phys. Lett.* **85**, 4355 (2004).

158. Yu, H., Ulker, E. & Ozbay, E. MOCVD growth and electrical studies of p-type AlGaN with Al fraction 0.35. *J. Cryst. Growth* **289**, 419–422 (2006).

159. Parish, G., Keller, S., Denbaars, S. P. & Mishra, U. K. SIMS investigations into the effect of growth conditions on residual impurity and silicon incorporation in GaN and $Al_xGa_{1-x}N$. *J.*

Electron. Mater. **29**, 15–20 (2000).

160. Gao, M. *et al.* Compositional modulation and optical emission in AlGaN epitaxial films. *J. Appl. Phys.* **100**, (2006).

161. Bradley, S. T., Goss, S. H., Brillson, L. J., Hwang, J. & Schaff, W. J. Deep level defects and doping in high Al mole fraction AlGaN. *J. Vac. Sci. Technol. B Microelectron. Nanom. Struct.* **21**, 2558 (2003).

162. Syed, A. A. & Cao, X. A. Thermal and plasma damage in AlGaN Schottky diodes. *J. Phys. D. Appl. Phys.* **42**, 4 (2009).

163. Hashizume, T. & Hasegawa, H. Effects of nitrogen deficiency on electronic properties of AlGaN surfaces subjected to thermal and plasma processes. in *Applied Surface Science* **234**, 387–394 (2004).

164. Hodges, C. *et al.* Optical investigation of degradation mechanisms in AlGaN/GaN high electron mobility transistors: Generation of non-radiative recombination centers. *Appl. Phys. Lett.* **100**, 112106 (2012).

165. Ťapajna, M., Simms, R. J. T., Pei, Y., Mishra, U. K. & Kuball, M. Integrated optical and electrical analysis: Identifying location and properties of traps in AlGaN/GaN HEMTs during electrical stress. *IEEE Electron Device Lett.* **31**, 662–664 (2010).

166. Sawyer, S., Rumyantsev, S. L. & Shur, M. S. Degradation of AlGaN-based ultraviolet light emitting diodes. *Solid. State. Electron.* **52**, 968–972 (2008).

167. Pinos, A. *et al.* Aging of AlGaN quantum well light emitting diode studied by scanning near-field optical spectroscopy. *Appl. Phys. Lett.* **95**, 181914 (2009).

168. Jones, R. E. *et al.* High electron mobility InN. *Appl. Phys. Lett.* **90**, 162103 (2007).

169. Pinos, A., Marcinkevičius, S. & Shur, M. S. High current-induced degradation of AlGaN ultraviolet light emitting diodes. in *Journal of Applied Physics* **109**, 103108 (2011).

170. Pinos, A. *et al.* Optical studies of degradation of AlGaN quantum well based deep ultraviolet light emitting diodes. *J. Appl. Phys.* **108**, 93113 (2010).

171. Gao, F. *et al.* Role of oxygen in the OFF-state degradation of AlGaN/GaN high electron mobility transistors. *Appl. Phys. Lett.* **99**, 223506 (2011).

172. Tapajna, M. *et al.* Influence of threading dislocation density on early degradation in AlGaN/GaN high electron mobility transistors. *Appl. Phys. Lett.* **99**, 223501 (2011).

173. Higashiwaki, M., Chowdhury, S., Swenson, B. L. & Mishra, U. K. Effects of oxidation on surface chemical states and barrier height of AlGaN/GaN heterostructures. *Appl. Phys. Lett.* **97**, 222104 (2010).

174. Qin, X., Dong, H., Kim, J. & Wallace, R. M. A crystalline oxide passivation for Al2O3/AlGaN/GaN. *Appl. Phys. Lett.* **105**, 141604 (2014).

175. Boroditsky, M. *et al.* Surface recombination measurements on III-V candidate materials for nanostructure light-emitting diodes. *J. Appl. Phys.* **87**, 3497–3504 (2000).

176. Aleksiejunas, R. *et al.* Determination of free carrier bipolar diffusion coefficient and surface recombination velocity of undoped GaN epilayers. *Appl. Phys. Lett.* **83**, 1157–1159 (2003).

177. Ščajev, P., Jarašiūnas, K., Okur, S., Özgür, U. & Morkoç, H. Carrier dynamics in bulk GaN. *J. Appl. Phys.* **111**, 023702 (2012).

178. Bulashevich, K. A. & Karpov, S. Y. Impact of surface recombination on efficiency of III-nitride light-emitting diodes. *Phys. status solidi - Rapid Res. Lett.* **10**, 480–484 (2016).

179. Kitagawa, H. *et al.* Green Photoluminescence from GaInN Photonic Crystals. *Appl. Phys. Express* **1**, 032004 (2008).

180. Kumakura, K. *et al.* Minority carrier diffusion lengths in MOVPE-grown n- and p-InGaN and performance of AlGaN/InGaN/GaN double heterojunction bipolar transistors. *J. Cryst. Growth* **298**, 787–790 (2007).

181. Aleksiejunas, R. *et al.* Diffusion-driven and excitation-dependent recombination rate in blue InGaN/GaN quantum well structures. *Appl. Phys. Lett.* **104**, (2014).

182. Passlack, M., Hong, M., Mannaerts, J. P., Kwo, J. R. & Tu, L. W. Recombination velocity at oxide-GaAs interfaces fabricated by in situ molecular beam epitaxy. *Appl. Phys. Lett.* **68**, 3605–3607 (1996).

183. Olson, J. M., Ahrenkiel, R. K., Dunlavy, D. J., Keyes, B. & Kibbler, A. E. Ultralow recombination velocity at Ga0.5In0.5P/GaAs heterointerfaces. *Appl. Phys. Lett.* **55**, 1208–1210 (1989).

184. Mohammaad, S. N. *et al.* Proposed explanation of the anomalous doping characteristics of III–V nitrides. *Philos. Mag. B Phys. Condens. Matter; Stat. Mech. Electron. Opt. Magn. Prop.* **76**, 131–143 (1997).

185. Arehart, A. R. *et al.* Deep level optical and thermal spectroscopy of traps in n -GaN grown by ammonia molecular beam epitaxy. *Appl. Phys. Lett.* **93**, 1–4 (2008).

186. Kinoshita, T., Obata, T., Yanagi, H. & Inoue, S. I. High p-type conduction in high-Al content Mg-doped AlGaN. *Appl. Phys. Lett.* **102**, 1–4 (2013).

187. Nakarmi, M. L. *et al.* Correlation between optical and electrical properties of Mg-doped AlN epilayers. *Appl. Phys. Lett.* **89**, 2004–2007 (2006).

188. Briot, O., Alexis, J. P., Tchounkeu, M. & Aulombard, R. L. Optimization of the MOVPE growth of GaN on sapphire. *Mater. Sci. Eng. B* **43**, 147–153 (1997).

189. Allerman, A. A. *et al.* Growth and design of deep-UV (240-290 nm) light emitting diodes using AlGaN alloys. *J. Cryst. Growth* **272**, 227–241 (2004).

190. Koleske, D. D., Wickenden, A. E., Henry, R. L., DeSisto, W. J. & Gorman, R. J. Growth model for GaN with comparison to structural, optical, and electrical properties. *J. Appl. Phys.* **84**, 1998–2010 (1998).

191. Keller, S. *et al.* Metalorganic chemical vapor deposition of high mobility AlGaN/GaN heterostructures. *J. Appl. Phys.* **86**, 5850–5857 (1999).

192. Ohba, Y., Yoshida, H. & Sato, R. Growth of High-Quality AlN, GaN and AlGaN with Atomically Smooth Surfaces on Sapphire Substrates. *Jpn. J. Appl. Phys.* **36**, L1565–L1567 (1997).

193. Mattila, T. & Nieminen, R. Point-defect complexes and broadband luminescence in GaN and AlN. *Phys. Rev. B - Condens. Matter Mater. Phys.* **55**, 9571–9576 (1997).

194. Lee, I. H. *et al.* Deep hole traps in undoped n-GaN films grown by hydride vapor phase epitaxy. *J. Appl. Phys.* **115**, (2014).

195. Elsner, J. & Jones, R. Deep acceptors trapped at threading-edge dislocations in GaN. *Phys. Rev. B - Condens. Matter Mater. Phys.* **58**, 12571–12574 (1998).

196. You, J. H., Lu, J. Q. & Johnson, H. T. Electron scattering due to threading edge dislocations in n-type wurtzite GaN. *J. Appl. Phys.* **99**, (2006).

197. Tuomisto, F. *et al.* Dissociation of VGa-ON complexes in HVPE GaN by high pressure and high temperature annealing. *Phys. Status Solidi Basic Res.* **243**, 1436–1440 (2006).

198. Nepal, N., Nakarmi, M. L., Lin, J. Y. & Jiang, H. X. Photoluminescence studies of impurity transitions in AlGaN alloys. *Appl. Phys. Lett.* **89**, 092107 (2006).

199. Sedhain, A., Lin, J. Y. & Jiang, H. X. Nature of optical transitions involving cation vacancies and complexes in AlN and AlGaN. *Appl. Phys. Lett.* **100**, (2012).

200. Khan, A., Balakrishnan, K. & Katona, T. Ultraviolet light-emitting diodes based on group three nitrides. *Nat. Photonics* **2**, 77–84 (2008).

201. Pinos, A. *et al.* Localization potentials in AlGaN epitaxial films studied by scanning near-field optical spectroscopy. *J. Appl. Phys.* **109**, (2011).

202. Chichibu, S. F. *et al.* Origin of defect-insensitive emission probability in In-containing (Al,In,Ga)N alloy semiconductors. *Nat. Mater.* **5**, 810–816 (2006).

203. Malinauskas, T. *et al.* Optical evaluation of carrier lifetime and diffusion length in synthetic diamonds. *Diam. Relat. Mater.* **17**, 1212–1215 (2008).

204. Lyon, T. J. De *et al.* Low surface recombination velocity and contact resistance using p + / p carbondoped GaAs structures. *Appl. Phys. Lett.* **56**, 2442 (1990).

205. Kuciauskas, D. *et al.* Charge-carrier transport and recombination in heteroepitaxial CdTe. *J. Appl. Phys.* **116**, (2014).

206. Ščajev, P., Usikov, A., Soukhoveev, V., Aleksiejūnas, R. & Jarašiūnas, K. Diffusion-limited nonradiative recombination at extended defects in hydride vapor phase epitaxy GaN layers. *Appl. Phys. Lett.* **98**, (2011).

207. Morkoç, H. Comprehensive characterization of hydride VPE grown GaN layers and templates. *Mater. Sci. Eng. R Reports* **33**, 135–207 (2001).

208. Mathis, S. K. *et al.* Modeling of threading dislocation reduction in growing GaN layers. *J. Cryst. Growth* **231**, 371–390 (2001).

209. Malinauskas, T. *et al.* All-optical characterization of carrier lifetimes and diffusion lengths in MOCVD-, ELO-, and HVPE- grown GaN. *J. Cryst. Growth* **300**, 223–227 (2007).

210. Lee, K. & Auh, K. Dislocation Density of GaN Grown by Hydride Vapor Phase. *MRS Internet J. Nitride Semicond. Res.* **9**, 1–4 (2001).

211. Lin, Y. J., Lin, W. X., Lee, C. T. & Chien, F. T. Changes in optical and electrical properties and surface recombination velocity of n-type GaN due to (NH4)2Sxtreatment. *Solid State Commun.* **137**, 257–259 (2006).

212. Iwata, H., Yokoyama, H., Sugimoto, M., Hamao, N. & Onabe, K. Reduction in interfacial recombination velocity by superlattice buffer

layers in GaAs/ AlGaAs quantum well structures. *Appl. Phys. Lett.* **54**, 2427 (1989).

213. Molenkamp, L. W. & van't Blik, H. F. J. Very low interface recombination velocity in (Al,Ga)As heterostructures grown by organometallic vapor-phase epitaxy. *J. Appl. Phys.* **64**, 4253–4256 (1988).

214. Limpijumnong, S. & Van de Walle, C. G. Diffusivity of native defects in GaN. *Phys. Rev. B - Condens. Matter Mater. Phys.* **69**, 1–11 (2004).

215. Ganchenkova, M. G. & Nieminen, R. M. Nitrogen vacancies as major point defects in gallium nitride. *Phys. Rev. Lett.* **96**, 1–4 (2006).

216. Mohanta, A., Jang, D. J., Wang, M. S. & Tu, L. W. Time-integrated photoluminescence and pump-probe reflection spectroscopy of Si doped InN thin films. *J. Appl. Phys.* **115**, 044906 (2014).

217. Chen, F., Cartwright, A. N., Lu, H. & Schaff, W. J. Temperature dependence of carrier lifetimes in InN. *Phys. Status Solidi A* **202**, 768–772 (2005).

218. Nargelas, S. *et al.* Injection-Activated Defect-Governed Recombination Rate in InN. *Jpn. J. Appl. Phys.* **52**, 08JD02 (2013).

219. Ascázubi, R., Wilke, I., Cho, S., Lu, H. & Schaff, W. J. Ultrafast recombination in Si-doped InN. *Appl. Phys. Lett.* **88**, 1–4 (2006).

220. Cho, Y. *et al.* Auger recombination as the dominant nonradiative recombination channel in InN. *Phys. Rev. B - Condens. Matter Mater. Phys.* **87**, 1–5 (2013).

221. Tsai, T. R., Chang, C. F. & Gwo, S. Ultrafast hot electron relaxation time anomaly in InN epitaxial films. *Appl. Phys. Lett.* **90**, 1–4 (2007).

222. Nargelas, S. *et al.* Dynamics of free carrier absorption in InN layers. *Appl. Phys. Lett.* **95**, 162103 (2009).

223. Chen, F., Cartwright, A. N., Lu, H. & Schaff, W. J. Ultrafast carrier dynamics in InN epilayers. *J. Cryst. Growth* **269**, 10–14 (2004).

224. Ma, N. *et al.* Hole mobility in wurtzite InN. *Appl. Phys. Lett.* **98**, 19–22 (2011).

225. Wang, X., Che, S. B., Ishitani, Y. & Yoshikawa, A. Hole mobility in Mg-doped p -type InN films. *Appl. Phys. Lett.* **92**, 2006–2009 (2008).

226. Xie, M. Y. *et al.* Effect of Mg doping on the structural and free-charge carrier properties of InN films. *J. Appl. Phys.* **115**, 163504 (2014).

227. Wang, K. *et al.* Mg doped InN and confirmation of free holes in InN. *Appl. Phys. Lett.* **98**, (2011).

228. Chen, F., Cartwright, A. N., Lu, H. & Schaff, W. J. Hole transport and carrier lifetime in InN epilayers. *Appl. Phys. Lett.* **87**, 1–3 (2005).

229. Nargelas, S. *et al.* Nonlinear carrier recombination and transport features in highly excited InN layer. *Phys. Status Solidi Curr. Top. Solid State Phys.* **6**, 735–738 (2009).

230. Intartaglia, R. *et al.* Radiative and nonradiative recombination processes in InN films grown by metal organic chemical vapor deposition. *Appl. Phys. Lett.* **86**, 142104 (2005).

231. Veal, T. D. *et al.* Electron accumulation at InN/AIN and InN/GaN interfaces. *Phys. Status Solidi C Conf.* **2**, 2246–2249 (2005).

232. Lu, H., Schaff, W. J., Eastman, L. F. & Stutz, C. E. Surface charge accumulation of InN films grown by molecular-beam epitaxy. *Appl. Phys. Lett.* **82**, 1736–1738 (2003).

233. Mahboob, I. *et al.* Origin of electron accumulation at wurtzite InN surfaces. *Phys. Rev. B - Condens. Matter Mater. Phys.* **69**, 1–4 (2004).

234. Li, S. X. *et al.* Fermi-level stabilization energy in group III nitrides. *Phys. Rev. B - Condens. Matter Mater. Phys.* **71**, 1–4 (2005).

235. Cimalla, V., Lebedev, V., Morales, F. M., Goldhahn, R. & Ambacher, O. Model for the thickness dependence of electron concentration in InN films. *Appl. Phys. Lett.* **89**, 1–4 (2006).

236. Lu, H. *et al.* Growth of Thick InN by Molecular Beam Epitaxy. *MRS Proc.* **743**, 1–6 (2002).

237. Piper, L. F. J., Veal, T. D., McConville, C. F., Lu, H. & Schaff, W. J. Origin of the n-type conductivity of InN: The role of positively charged dislocations. *Appl. Phys. Lett.* **88**, 1–4 (2006).

238. Malinauskas, T. *et al.* Optical monitoring of nonequilibrium carrier lifetime in freestanding GaN by time-resolved four-wave mixing and photoluminescence techniques. *Appl. Phys. Lett.* **88**, 202109 (2006).

239. Hader, J., Moloney, J. V. & Koch, S. W. Beyond the ABC: carrier recombination in semiconductor lasers. in *Physics and Simulation of Optoelectronic Devices XIV* 61151T (International Society for Optics and Photonics, 2006). doi:10.1117/12.641744

240. Linnros, J. & Grivickas, V. Carrier-diffusion measurements in silicon with a Fourier-transient-grating method. *Phys. Rev. B* **50**, 16943–16955 (1994).

241. Sun, S. Z. *et al.* Observation of femtosecond carrier thermalization

time in indium nitride. *J. Appl. Phys.* **103**, 123513 (2008).

242. Reklaitis, A., Krotkus, A. & Grigaliunaite, G. Enhanced drift velocity of photoelectrons in a semiconductor with ultrafast carrier recombination. *Semicond. Sci. Technol.* **14**, 945–947 (1999).

243. Song, D. Y. *et al.* Effect of stress and free-carrier concentration on photoluminescence in InN. *Appl. Phys. Lett.* **92**, 1–4 (2008).

244. Suihkonen, S., Sormunen, J., Rangel-Kuoppa, V. T., Koskenvaara, H. & Sopanen, M. Growth of InN by vertical flow MOVPE. *J. Cryst. Growth* **291**, 8–11 (2006).

245. Yamamoto, A., Sugita, K., Takatsuka, H., Hashimoto, A. & Davydov, V. Y. Correlations between electrical and optical properties for OMVPE InN. *J. Cryst. Growth* **261**, 275–279 (2004).

246. Wu, J. When group-III nitrides go infrared: New properties and perspectives. *J. Appl. Phys.* **106**, 5 (2009).

247. Jenkins, P. Space PV Systems and Flight Demonstrations. in *Photovoltaic Solar Energy* (eds. Reinders, A., Verlinden, P., Sark, W. van & Freundlich, A.) 444–454 (John Wiley & Sons, Ltd, 2017). doi:10.1002/9781118927496.ch40

248. Wang, J., Mulligan, P., Brillson, L. & Cao, L. R. Review of using gallium nitride for ionizing radiation detection. *Appl. Phys. Rev.* **2**, 031102 (2015).

249. Pearton, S. J., Ren, F., Patrick, E., Law, M. E. & Polyakov, A. Y. Review—Ionizing Radiation Damage Effects on GaN Devices. *ECS J. Solid State Sci. Technol.* **5**, Q35–Q60 (2016).

250. Walukiewicz, W. *et al.* Dopants and defects in InN and InGaN alloys. *J. Cryst. Growth* **288**, 278–282 (2006).

251. Johnston, A. H. Radiation effects in optoelectronic devices. *IEEE Trans. Nucl. Sci.* **60**, 2054–2073 (2013).

252. Clays, C. & Simoen, E. *Radiation Effects in Advanced Semiconductor Materials and Devices*. (Springer-Verlag Berlin Heidelberg GmbH, 2002). doi:10.1007/978-3-662-04974-7

253. Messenger, S. R., Summers, G. P., Burke, E. A., Walters, R. J. & Xapsos, M. A. Modeling solar cell degradation in space: A comparison of the NRL displacement damage dose and the JPL equivalent fluence approaches. *Prog. Photovoltaics Res. Appl.* **9**, 103–121 (2001).

254. Xapsos, M. A., Barth, J. L., Stassinopoulos, E. G., Burke, E. A. & Gee, G. B. Space Environment Effects: Model for Emission of Solar Protons (ESP)--Cumulative and Worst-Case Event Fluences. *Sp.*

Environ. Eff. Model Emiss. Sol. protons - Cumul. worst-case event fluences / M.A. Xapsos ... [et al.]. MSFC (1999).

255. Anspaugh, B. E. GaAs Solar Cell Radiation Handbook. *Natl. Aeronaut. and. Sp. Adm. JPL* (1996).

256. Boschini, M. J., Rancoita, P. G. & Tacconi, M. SR-NIEL Calculator: Screened Relativistic (SR) Treatment for Calculating the Displacement Damage and Nuclear Stopping Powers for Electrons, Protons, Light- and Heavy- Ions in Materials. *SR-NIEL Calculator: Screened Relativistic (SR) Treatment for Calculating the Displacement Damage and Nuclear Stopping Powers for Electrons, Protons, Light- and Heavy- Ions in Materials* (2014). Available at: http://www.sr-niel.org.

257. Lauenstein, J. M. & Barth, J. L. Radiation belt modeling for spacecraft design: Model comparisons for common orbits. in *IEEE Radiation Effects Data Workshop* 102–109 (IEEE, 2005). doi:10.1109/REDW.2005.1532674

258. ECSS Secretariat & ESA-ESTEC. *ECSS-E-ST-10-04C: Space engineering, Space environment*. (ESA Requirements and Standards Division, 2008).

259. Miroshnichenko, L. I. & Nymmik, R. A. Extreme fluxes in solar energetic particle events: Methodological and physical limitations. *Radiat. Meas.* **61**, 6–15 (2014).

260. Barth, J. L., Dyer, C. S. & Stassinopoulos, E. G. Space, atmospheric, and terrestrial radiation environments. *IEEE Trans. Nucl. Sci.* **50 III**, 466–482 (2003).

261. Ziegler, J. F. SRIM. *The Stopping and Range of Ions in Matter* (2013). Available at: http://www.srim.org. (Accessed: 2nd July 2018)

262. Ruffenach, S., Moret, M., Briot, O. & Gil, B. Recent advances in the MOVPE growth of indium nitride. *Phys. Status Solidi* **207**, 9–18 (2010).

263. Gallinat, C. S., Koblmuller, G. & Speck, J. S. The role of threading dislocations and unintentionally incorporated impurities on the bulk electron conductivity of In-face InN. *Appl. Phys. Lett.* **95**, 2007–2010 (2009).

264. Van De Walle, C. G., Lyons, J. L. & Janotti, A. Controlling the conductivity of InN. *Phys. Status Solidi Appl. Mater. Sci.* **207**, 1024–1036 (2010).

265. Yamamoto, A., Sugita, K. & Hashimoto, A. Elucidation of factors obstructing quality improvement of MOVPE-grown InN. *J. Cryst. Growth* **311**, 4636–4640 (2009).

266. Khan, N., Sedhain, A., Li, J., Lin, J. Y. & Jiang, H. X. High mobility InN epilayers grown on AlN epilayer templates. *Appl. Phys. Lett.* **92**, 2006–2009 (2008).

267. Liliental-Weber, Z. *et al.* TEM studies of as-grown, irradiated and annealed InN films. *Phys. B Condens. Matter* **401**–**402**, 646–649 (2007).

268. Walters, R. Materials, Cell Structures, and Radiation Effects. in *Photovoltaic Solar Energy* (eds. Reinders, A., Verlinden, P., Sark, W. van & Freundlich, A.) 431–443 (John Wiley & Sons, Ltd, 2017). doi:10.1002/9781118927496.ch39

269. Barry, A. L., Houdayer, A. J., Hinrichsen, P. F., Letourneau, W. G. & Vincent, J. The Energy Dependence of Lifetime Damage Constants in GaAs LEDs for 1 – 500 MeV Protons. *IEEE Trans. Nucl. Sci.* **42**, 2104–2107 (1995).

270. Walters, R. J. *et al.* Correlation of proton radiation damage in InGaAs-GaAs quantum-well light-emitting diodes. in *IEEE Transactions on Nuclear Science* **48**, 1773–1777 (2001).

271. Khanna, S. M. *et al.* Proton energy dependence of the light output in gallium nitride light-emitting diodes. *IEEE Trans. Nucl. Sci.* **51**, 2729–2735 (2004).

272. Warner, J. H. *et al.* High-Energy Proton Irradiation Effects in GaAs Devices. *IEEE Trans. Nucl. Sci.* **51**, 2887–2895 (2004).

273. Rose, B. H. Proton damage effects on light emitting diodes. *J. Appl. Phys.* **53**, 1772 (1982).

274. Wu, J. *et al.* Superior radiation resistance of In1−xGaxN alloys: Full-solar-spectrum photovoltaic material system. *J. Appl. Phys.* **94**, 6477–6482 (2003).

275. Brown, G. F., Ager, J. W., Walukiewicz, W., Schaff, W. J. & Wu, J. Probing and modulating surface electron accumulation in InN by the electrolyte gated Hall effect. *Appl. Phys. Lett.* **93**, 2008–2010 (2008).

276. Miller, N. *et al.* Hole transport and photoluminescence in Mg-doped InN. *J. Appl. Phys.* **107**, (2010).

277. IOFFE. Electrical properties of GaAs. Available at: http://www.ioffe.ru/SVA/NSM/Semicond/GaAs/electric.html. (Accessed: 10th October 2019)

ŽYDRŪNAS PODLIPSKAS | CV

Birthdate 20 April 1989

Email zydrunas.podlipskas@ff.vu.lt

WORK EXPERIENCE

Junior Research Fellow 2017 – Present
Institute of Photonics and Nanotechnology, Vilnius University

Engineer 2014 – 2017
Institute of Photonics and Nanotechnology, Vilnius University

EDUCATION

PhD Studies in Physics 2014 – 2018
Institute of Photonics and Nanotechnology, Vilnius University

Master of Materials and Technology of Optoelectronics 2012 – 2014
Vilnius University

Bachelor of Applied Physics 2008 – 2012
Vilnius University

PROJECTS

01.2.2-CPVA-K-703-02-0002 2018 – Present
Jonizuojančiosios spinduliuotės nesąlytinio ir nuotolinio detektavimo technologijų centras

09.3.3-LMT-K-712-01-0013 2018 – Present
Spartūs scintiliatoriai spinduliuotės detektoriams

01.2.2-LMT-K-718-01-0041, SMART 2018 – Present
Neutronų srauto detektavimo sistema su optiniu signalo nuskaitymu

LMT, S-MIP-17-75 2017 – Present
Nespindulinės rekombinacijos keliai nepoliniuose ir pusiau poliniuose InGaN dariniuose

EK, Horizontas 2020, AIDA2020 2019 – 2019

LMT, S-LLT-18-1 2017 – 2018
Fotosensorius GeSn pagrindu – nuo fundamentinių tyrimų iki taikymų

LMT, LAT-16022 2016 – 2018
Nitridiniai puslaidininkiai radiacijai atspariems infraraudonosios spinduliuotės detektoriams

LMA, CERN-VU-2016-1 2017 – 2017
Scintiliatoriai ateities kalorimetrams

Papers

Paper A PODLIPSKAS, Ž., Aleksiejūnas, R., Kadys, A., Mickevičius, J., Jurkevičius, J., Tamulaitis, G., Shur, M. S., Shatalov, M., Yang, J. & Gaska, R. Dependence of radiative and nonradiative recombination on carrier density and Al content in thick AlGaN epilayers. *Journal of Physics D: Applied Physics* **49**, 145110 (2016).

Paper B PODLIPSKAS, Ž., Aleksiejūnas, R., Nargelas, S., Jurkevičius, J., Mickevičius, J., Kadys, A., Tamulaitis, G., Shur, M. S., Shatalov, M., Yang, J. & Gaska, R. Photomodification of carrier lifetime and diffusivity in AlGaN epitaxial layers. *Current Applied Physics* **16**, 633–637 (2016).

Paper D Aleksiejūnas, R., PODLIPSKAS, Ž., Nargelas, S., Kadys, A., Kolenda, M., Nomeika, K., Mickevičius, J. & Tamulaitis, G. Direct Auger recombination and density-dependent hole diffusion in InN. *Scientific Reports* **8**, 4621 (2018).

Paper E PODLIPSKAS, Ž., Jurkevičius, J., Kadys, A., Kolenda, M., Kovalevskij, V., Dobrovolskas, D., Aleksiejūnas, R. & Tamulaitis, G. Extreme radiation resistance in InN. *Journal of Alloys and Compounds* **789**, 48–55 (2019).

Paper A

Dependence of radiative and nonradiative recombination on carrier density and Al content in thick AlGaN epilayers

Podlipskas, Ž., Aleksiejūnas, R., Kadys, A., Mickevičius, J., Jurkevičius, J., Tamulaitis, G., Shur, M. S., Shatalov, M., Yang, J. & Gaska, R.

Journal of Physics D: Applied Physics **49**, 145110 (2016)

DOI:10.1088/0022-3727/49/14/145110

Paper B

Photomodification of carrier lifetime and diffusivity in AlGaN epitaxial layers

Podlipskas, Ž., Aleksiejūnas, R., Nargelas, S., Jurkevičius, J., Mickevičius, J., Kadys, A., Tamulaitis, G., Shur, M. S., Shatalov, M., Yang, J. & Gaska, R.

Current Applied Physics **16**, 633–637 (2016)

DOI:10.1016/j.cap.2016.03.010

Paper D

Direct Auger recombination and density-dependent hole diffusion in InN

Aleksiejūnas, R., Podlipskas, Ž., Nargelas, S., Kadys, A., Kolenda, M., Nomeika, K., Mickevičius, J. & Tamulaitis, G.

Scientific Reports **8**, 4621 (2018)

DOI:10.1038/s41598-018-22832-6

Paper E

Extreme radiation resistance in InN

Podlipskas, Ž., Jurkevičius, J., Kadys, A., Kolenda, M., Kovalevskij, V., Dobrovolskas, D., Aleksiejūnas, R. & Tamulaitis, G.

Journal of Alloys and Compounds **789**, 48–55 (2019)

DOI:10.1016/j.jallcom.2019.03.108

Vilniaus universiteto leidykla
Saulėtekio al. 9, LT-10222 Vilnius
El. p. info@leidykla.vu.lt
www.leidykla.vu.lt
Tiražas 20 egz.